

DESIGN AND IMPLEMENTATION  
OF A  
HYBRID MULTIPATH SIMULATION SYSTEM  
FOR THE STUDY OF  
DIFFUSE MULTIPATH

by



GREGORY BRENT WILSON

A Thesis

Submitted to the Faculty of Engineering  
in Partial Fulfillment of the Requirements for  
the Degree  
Master of Engineering

McMaster University

February 1982

A HYBRID MULTIPATH SIMULATION SYSTEM

MASTER OF ENGINEERING  
(Electrical Engineering)

McMASTER UNIVERSITY  
Hamilton, Ontario

TITLE: Design and Implementation of a Hybrid Multipath  
Simulation system for the Study of Diffuse Multipath

AUTHOR: Gregory Brent Wilson

SUPERVISOR: Dr. S. Haykin

NUMBER OF PAGES: (xiv), 169.

## ABSTRACT

Radiation returning from a target at low elevation to a radar can have a wide variety of characteristics. In general, we see return not only from the target itself, but from its image as well; this is the essence of multipath. The nature of this multipath depends on a number of factors, the most important of which is the roughness of the reflecting surface. The study of this return is essential in order that we may overcome the problems associated with target detection in multipath environments.

In this thesis, methods of simulating diffuse multipath are discussed, and a hybrid system has been constructed which illustrates the effect of a phased array receiver on the observed radar return.

## ACKNOWLEDGEMENTS

I am grateful to my supervisor, Dr. Simon Haykin, for the guidance, encouragement and support he has given me throughout the course of my research.

The progression of my work was greatly aided by the advice and constructive criticism of the many graduate students and staff members associated with the Communication Research Laboratory. Special recognition should be given to Vytas Kezys and Nick Slater for the use of their graphics routines.

I thank Jon Betz for his assistance in the development of much of the system hardware. I would also like to thank Dave Sutherland and Peter Young for their contributions in developing the transmitter position control system.

In closing, I would like to extend a very special thank-you to my girlfriend, Brenda Fox, for being understanding and supportive for the duration of my studies.

To my parents

## TABLE OF CONTENTS

Abstract  
Acknowledgements  
List of Figures  
List of Tables

### CHAPTER 1: INTRODUCTION

### CHAPTER 2: THE MULTIPATH PROBLEM

- 2.1 Multipath Interference
- 2.2 Specular Multipath
- 2.3 Diffuse Scattering
- 2.4 Diffuse Roughness Masking

### CHAPTER 3: SIMULATION TECHNIQUES

- 3.1 The Simulation of Multipath
- 3.2 A Holographic Approach to the Synthesis of Multipath
- 3.3 The Phased Array Multipath Simulator
- 3.4 The Hybrid Multipath Simulator
- 3.5 Merits of Hybrid Simulation

### CHAPTER 4: HYBRID SYSTEM FEATURES

- 4.1 Overview
- 4.2 Hardware
- 4.3 Software

## CHAPTER 5: RESULTS

- 5.1.1 Theoretical
- 5.1.2 RMS-Surface Slope
- 5.1.3 RMS Surface Height Deviation
- 5.1.4 Elevation
- 5.1.5 Summary of Theoretical Results
- 5.2.1 Experimental
- 5.2.2 Case I
- 5.2.3 Case II
- 5.2.4 Case III
- 5.2.5 Summary of Experimental Results

## CHAPTER 6: CONCLUDING REMARKS

- 6.1 Conclusions
- 6.2 Recommendations

## REFERENCES

## APPENDIX A: SYSTEM HARDWARE

- A.1.1 Microwave Hardware
- A.1.2 VSWR Test Performed on New Elliptical Waveguide
- A.2.1 Data Acquisition System (DAS)
- A.2.2 Timing for DAS
- A.3.1 Receiver Position Control System
- A.3.2 Switching Circuits
- A.3.3 Speed Control Circuit
- A.4 Transmitter Positioning Device



APPENDIX B: SYSTEM SOFTWARE

B.1.1 Program DVS72

B.2.1 Program AJUST

B.3.1 Program DFGEN

B.4.1 Program SHAPE

B.5.1 Program DF3DP

P

LIST OF FIGURES.

- Figure 2.1 Illustration of a typical multipath occurrence in mobile communications.
- Figure 2.2 A microwave position triangulation system.
- Figure 2.3 Multipath geometry for a flat earth.
- Figure 2.4 Reflection coefficient of a perfectly plane earth with  $\epsilon/\epsilon_0 = 10$ ,  $\sigma = 10^{-3}$  mho/m.  $\Delta$
- Figure 2.5 Reflection coefficient of a very smooth sea,  $\epsilon/\epsilon_0 = 80$ ,  $\sigma = 4$  mho/m.  $\Delta$
- Figure 2.6 Phase  $\phi$  of the reflection coefficient of a perfectly plane earth,  $\epsilon/\epsilon_0 = 10$ ,  $\sigma = 10^{-3}$  mho/m.  $\Delta$
- Figure 2.7 Phase  $\phi$  of the reflection coefficient of a very smooth sea,  $\epsilon/\epsilon_0 = 80$ ,  $\sigma = 4$  mho/m.  $\Delta$
- Figure 2.8 The first fresnel zone from which specular reflections may occur.
- Figure 2.9 Various forms of the glissening surface from which diffuse reflections may occur.
- Figure 2.10 Specular and diffuse scattering coefficients versus roughness.\*
- Figure 2.11 Glistening surface geometry of diffuse multipath.
- Figure 3.1 Holographic recording apparatus.
- Figure 3.2 Holographic reproduction of the object antenna of Figure 3.1.
- Figure 3.3 Phased array multipath simulation transmitter.
- Figure 3.4 Overview of complete phased array multipath simulator.

---

\* Figure 2.10 has been taken from figure 4, page 689, reference [9].

$\Delta$  Figures 2.4, 2.5, 2.6 and 2.7 were reproduced from figures 11.1, 11.2, 11.3 and 11.4, pages 220 and 221 of reference [8].

Figure 4.1 Block diagram illustrating the hybrid multipath simulator's major hardware components.

Figures 5.1.2.A-E The diffuse reflection coefficient versus look angle for varying RMS surface slope for a target elevation of  $\theta_t$  and a surface height deviation of  $\sigma_h$ :

Figure 5.1.2.A  $\theta_t = .5$  degrees,  $\sigma_h = .6$  metres.

Figure 5.1.2.B  $\theta_t = .5$  degrees,  $\sigma_h = .15$  metres.

Figure 5.1.2.C  $\theta_t = .5$  degrees,  $\sigma_h = .0375$  metres.

Figure 5.1.2.D  $\theta_t = 1.0$  degrees,  $\sigma_h = .15$  metres.

Figure 5.1.2.E  $\theta_t = .25$  degrees,  $\sigma_h = .15$  metres.

Figures 5.1.3.A-E The diffuse reflection coefficient versus look angle for varying RMS surface height deviation, with an RMS surface slope of  $\beta_0$  and a target elevation of  $\theta_t$ :

Figure 5.1.3.A  $\beta_0 = .1$  radians,  $\theta_t = .5$  degrees.

Figure 5.1.3.B  $\beta_0 = .01$  radians,  $\theta_t = .5$  degrees.

Figure 5.1.3.C  $\beta_0 = .001$  radians,  $\theta_t = .5$  degrees.

Figure 5.1.3.D  $\beta_0 = .01$  radians,  $\theta_t = 1.0$  degrees.

Figure 5.1.3.E  $\beta_0 = .01$  radians,  $\theta_t = .25$  degrees.

Figures 5.1.4.A-E The diffuse reflection coefficient versus look angle for varying target elevation with a RMS surface slope of  $\beta_0$  and RMS surface height deviation of  $\sigma_h$ :

Figure 5.1.4.A  $\beta_0 = .01$  radians,  $\sigma_h = .6$  metres.

Figure 5.1.4.B  $\beta_0 = .01$  radians,  $\sigma_h = .15$  metres.

Figure 5.1.4.C  $\beta_0 = .01$  radians,  $\sigma_h = .0375$  metres.

Figure 5.1.4.D  $\beta_0 = .1$  radians,  $\sigma_h = .15$  metres.

Figure 5.1.4.E  $\beta_0 = .001$  radians,  $\sigma_h = .15$  metres.

		RMS surface slope	RMS surface height deviation	target elevation
Figures 5.2.2.A-I	Case I	$\beta_0 = .1$ radians	$\sigma_h = .15$ metres	$\theta_t = .25$ degrees
Figure 5.2.2.A	Extent of glistening surface.			
Figure 5.2.2.B	Magnitude of the diffusion reflection coefficient (theoretical).			
Figure 5.2.2.C	Phase of the diffuse reflection coefficient (theoretical).			
Figure 5.2.2.D	5. degree blow-up of the theoretical diffuse reflection coefficient's magnitude.			
Figure 5.2.2.E	5. degree blow-up of the theoretical phase of the diffuse reflection coefficient.			
Figure 5.2.2.F	Magnitude of the reflection coefficient with experimental element pattern applied.			
Figure 5.2.2.G	Phase of the reflection coefficient with experimental element phase applied.			
Figure 5.2.2.H	Magnitude of the reflection coefficient for the combined array pattern.			
Figure 5.2.2.I	Phase of the reflection coefficient for the combined array pattern.			
Figures 5.2.3.A-I	Case II	$\beta_0 = .01$ radians	$\sigma_h = .15$ metres	$\theta_t = .25$ degrees
Figure 5.2.3.A	Extent of glistening surface.			
Figure 5.2.3.B	Magnitude of the diffusion reflection coefficient (theoretical).			
Figure 5.2.3.C	Phase of the diffuse reflection coefficient (theoretical).			
Figure 5.2.3.D	5. degree blow-up of the theoretical diffuse reflection coefficient's magnitude.			
Figure 5.2.3.E	5. degree blow-up of the theoretical phase of the diffuse reflection coefficient.			

- Figure 5.2.3.F Magnitude of the reflection coefficient with experimental element pattern applied.
- Figure 5.2.3.G Phase of the reflection coefficient with experimental element phase applied.
- Figure 5.2.3.H Magnitude of the reflection coefficient for the combined array pattern.
- Figure 5.2.3.I Phase of the reflection coefficient for the combined array pattern.
- Figures 5.2.4.A-I Case III  $\beta_0 = .01$   $\sigma_h = .15$   $\theta_t = 2.5$   
radians metres degrees
- Figure 5.2.4.A Extent of glistening surface.
- Figure 5.2.4.B Magnitude of the diffusion reflection coefficient (theoretical).
- Figure 5.2.4.C Phase of the diffuse reflection coefficient (theoretical).
- Figure 5.2.4.D 5 degree blow-up of the theoretical diffuse reflection coefficient's magnitude.
- Figure 5.2.4.E 5 degree blow-up of the theoretical phase of the diffuse reflection coefficient.
- Figure 5.2.4.F Magnitude of the reflection coefficient with experimental element pattern applied.
- Figure 5.2.4.G Phase of the reflection coefficient with experimental element phase applied.
- Figure 5.2.4.H Magnitude of the reflection coefficient for the combined array pattern.
- Figure 5.2.4.I Phase of the reflection coefficient for the combined array pattern.
- Figure A.1 Microwave hardware for hybrid multipath simulation system.
- Figure A.2 Apparatus for forward power measurement.
- Figure A.3 Apparatus for reflected power measurement.

- Figure A.4 Magic or Hybrid Tee.
- Figure A.5 Data Acquisition System circuit diagram.
- Figure A.6 Data Acquisition System timing diagram.
- Figure A.7 Block diagram of Receiver Position Control system.
- Figure A.8 Complete circuit diagram for Receiver Position Control system.
- Figure A.9 Circuit diagram for relay switching.
- Figure A.10 Circuit diagram for speed control.
- Figure A.11 Sketch of Transmitter Positioning Mechanism.
- Figure A.12 Drive housing for Positioning Mechanism.
- Figure A.13 Carriage of Positioning Mechanism.

LIST OF TABLES

A.3.4.1 Parts list for drive housing of Positioning Mechanism.

A.3.4.2. Parts list for carriage of Positioning Mechanism.

CHAPTER 1  
INTRODUCTION

Radar (radio detecting and ranging) received the bulk of its development during World War II. The decimeter wavelength radars of that time being largely unimpaired by such things as fog, cloud and the optical horizon, stimulated radar's usage in military surveillance, weapon control and navigation [2,3]. The use of radar at present time, however, goes far beyond that of the military with wavelengths extending into the millimeter range, though most are centimeter radars[6]. Most air travel is controlled with either on board or ground based radars, while the navigation of ships, monitoring of traffic speed, and the exploration of the universe all involve various forms of radar.

All radar systems involve the detection of objects, be they natural or man-made. This detection is accomplished by the observation of electromagnetic signals either reflected from the object by the radar; or transmitted directly to the radar as in the case of a beacon. Not only does radar permit the observation of an object which may be optically obscured, but they also relieve perceptual problems often associated with optics by allowing these objects to be viewed in a planar format (as in the case of the PPI "plan position indicator") regardless of the illumination angle [2]. Another plus for radar is that not only can objects be viewed in the three dimensional space of azimuth, elevation and range, but a target's velocity can also be



determined by the radar's doppler coordinate.

At this time, it may be of value to look at the course radar has taken since World War II, what its limitations were then and their present day state. The major concern of early radar engineers was to increase the signal-to-noise ratio in both the pulsed and continuous wave (CW) radars. Throughout the 1940's, emphasis was placed on the development of systems transmitting large amounts of power [2]. This level of radiation was required in order to provide the relatively insensitive receiver components with sufficient signal return to permit target detection. With the simple waveforms being transmitted at that time, resolution was being sacrificed for longer detection times. At this point, pulse compression techniques such as "chirp" were being developed to satisfy the resolution and detection problem. New technology in the form of diode mixers and the like, resulted in systems of much higher sensitivity accommodating much greater range measurements.

These high-sensitivity systems now extending into the centimeter wavelengths were plagued with problems. Many abnormalities not visible to the earlier radars were now crowding the screens of the new systems. Clutter in the form of rain, clouds, birds, land and sea reflections were impairing the operation of these radars. Nevertheless by the early 1960's the problems associated with target detection limited by receiver noise had been for the most part overcome. This improvement, largely due to the existence of better signal processing techniques, opened the door to many studies involving the statistical characteristics of other forms of interference. By the late 1960's, much had been determined

about the statistical nature of clutter. In the 1970's, advanced signal processing techniques produced favourable results; however, errors still occurred in severely cluttered environments.

-Considerable interest has been directed in recent years to the errors encountered through system response to multipath environments. In the early chapters of this thesis the characteristics of both specular and diffuse multipath are reviewed in some detail. In Chapter 3, three ways of generating realistic multipath in the laboratory are discussed. These methods are: microwave holography, phased arrays, and the last (hybrid) method involving synthetic aperture techniques. In Chapter 4, an outline of the design and implementation of the latter technique is given. A comparison of the experimental results with those found in practice are discussed in the Chapter 5 of this thesis.

## CHAPTER 2

### THE MULTIPATH PROBLEM

#### 2.1 Multipath Interference

Multipath is a problem not unique to the radar situation, in fact, it occurs in most areas of communications. A microwave radio signal transmitted between a fixed base station and a moving vehicle in a typical urban environment exhibits extreme variations in both amplitude and apparent frequency [4]. This occurrence of multipath interference is caused by the numerous signals reflected from buildings and other obstacles in the vicinity of the mobile unit. The above mentioned case is illustrated in Figure 2.1.

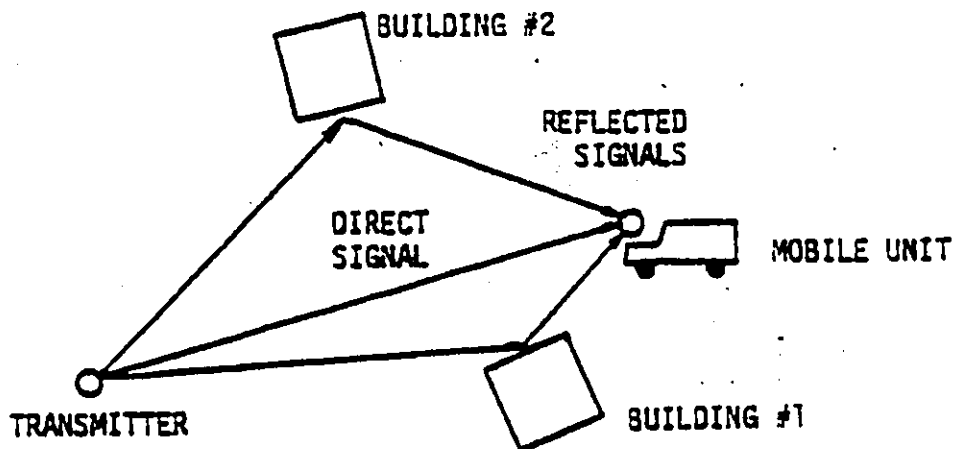


Figure 2.1 Illustration of a typical multipath occurrence in mobile communications.

Multipath also accounts for errors generated in high performance missile tracking systems. Figure 2.2 illustrates such a system. In this case, ranging between the missile and a ground location is accomplished by measuring the phase difference between a reference CW transmission and a replica of the reference which has traveled to the missile and back to the ground location [5]. Ground reflections in the vicinity of the ground receivers cause errors in the phase measured in this system.

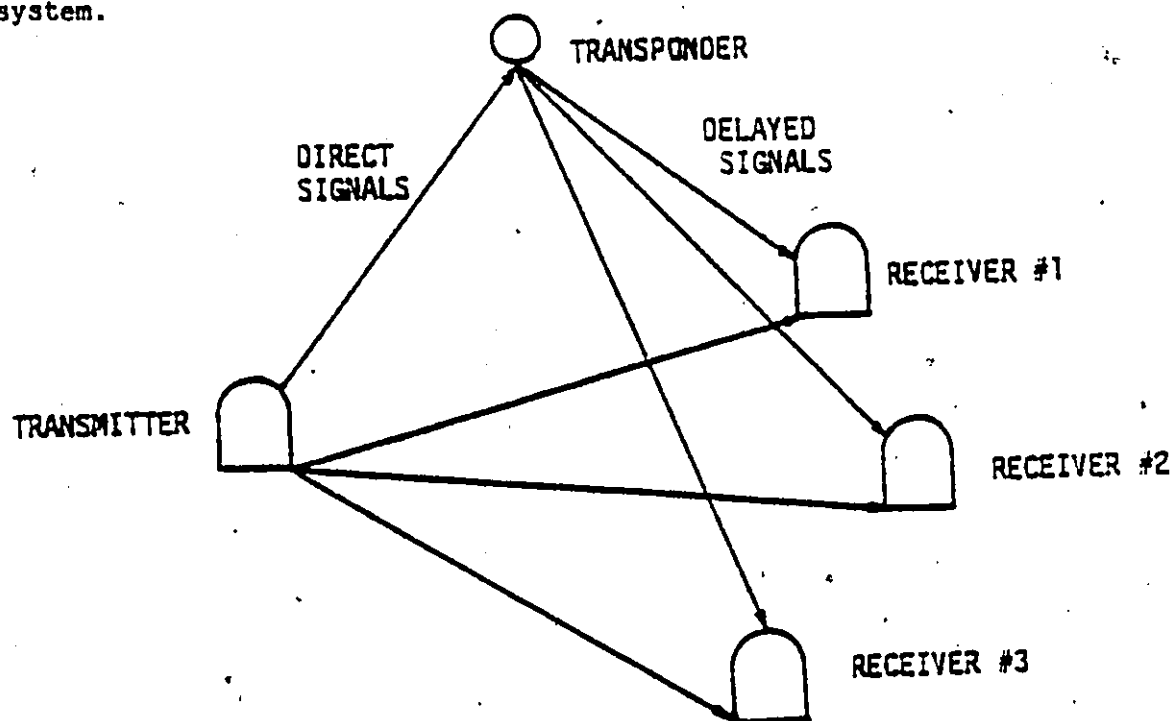


Figure 2.2 A microwave position triangulation system.

The occurrence of multipath in a low-elevation tracking radar environment will be developed in this thesis. Emphasis has been placed on the recent work of D.K. Barton [9]. The types of multipath signals encountered can vary widely in nature. The term specular is given to multipath which is coherent (varies deterministically with respect to

the local oscillator). Specular multipath is found where low elevation targets are being tracked above smooth surfaces. One incidence of a specular multipath problem would be the tracking of an airplane making its landing approach above the pavement of a runway. Microwaves radiating isotropically from the airplane will be reflected specularly from the pavement since its surface would appear smooth to this radiation. The receiving element, seeing signals directly from the plane and the reflected signals as well, may indicate the present of two targets, or one dumbbell target depending on the plane's elevation. The tracking of a target above a rough surface such as the sea, would on the other hand result in a multipath component which is diffuse in nature. Diffuse multipath is incoherent with respect to the local oscillator, appearing as narrow band noise, and it may be distributed over a large area between the target and the residing radar [7].

The characteristics of multipath depend on many factors such as; wavelength, polarization, grazing angle and the chemical properties of the reflecting surface. These reflections from the earth's surface will be specular or diffuse in nature. Pure specular reflections will result only from perfectly smooth surfaces such as pavement, concrete and especially calm water. The earth's natural surfaces in general produce reflections that contain both specular and diffuse components. The specular reflections give the same radiation pattern as that of a "perfectly" smooth surface, while a spherical pattern is observed in the diffuse case [3].

2.2 Specular Multipath

Figure 2.3 indicates the multipath geometry for a flat earth upon which the following analysis of specular multipath is based. Assuming the target to be an isotropic radiator, we have two signals impinging on the receiving aperture. The first, being the target direct signal arriving at an angle  $\theta_d$  (with respect to the receiver's boresight), adds to the surface-reflected signal at angle  $-\theta_r$ ; this combination results in a net electric signal, given by:

$$E = A_d + A_r e^{-j\alpha} \tag{2.1}$$

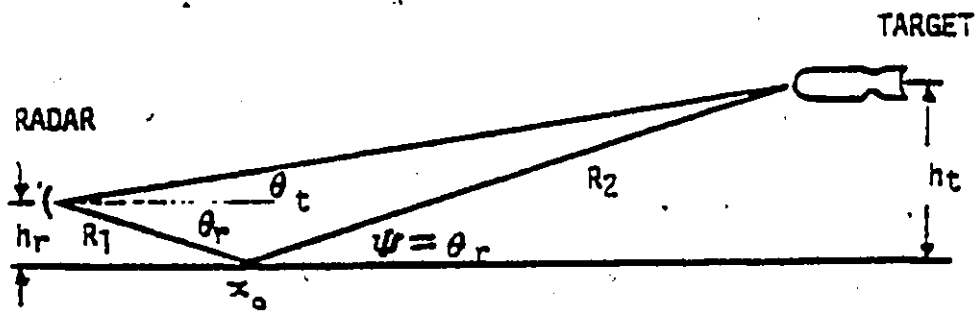


Figure 2.3 Multipath geometry for a flat earth.

The term  $A_d$  represents the signal strength of the direct component and  $A_r$  the reflected signal's strength, such that the surface reflection coefficient is given by  $\rho_0$  of equation (2.2):

$$\rho_0 = A_r / A_d \tag{2.2}$$

The reflection coefficient  $\rho_0$  is a function of the grazing angle  $\psi$ , wavelength  $\lambda$ , and polarization. Figures 2.4 and 2.5 taken from, [8], illustrate this relationship for land and sea.

The  $\alpha$  term of equation (2.1) represents the total phase shift due

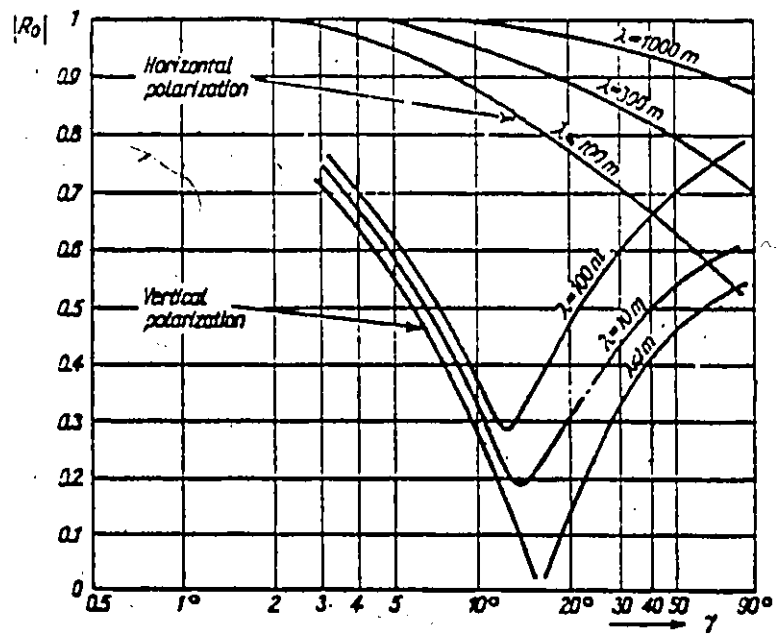


Figure 2.4 Reflection coefficient of a perfectly plane earth with  $\epsilon/\epsilon_0 = 10$ ,  $\sigma = 10^{-3}$  mho/m.

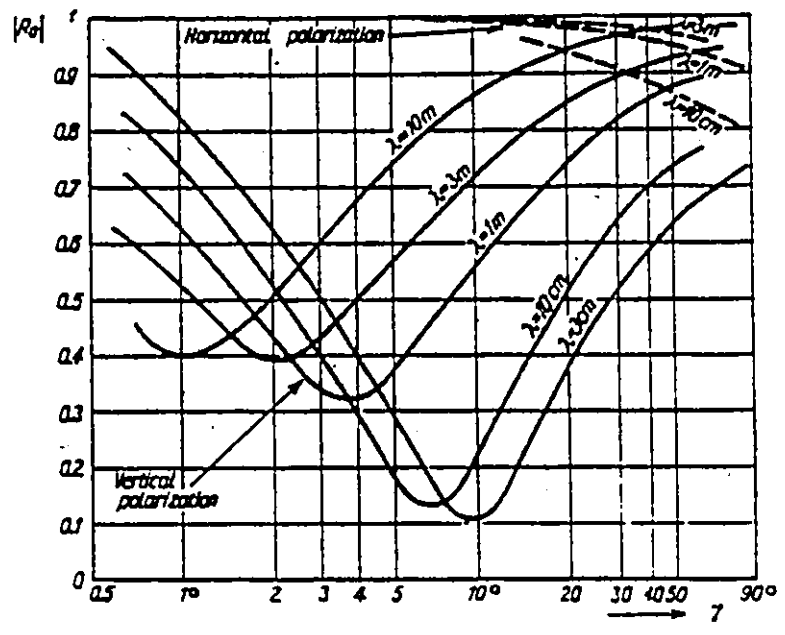


Figure 2.5 Reflection coefficient of a very smooth sea.  $\epsilon/\epsilon_0 = 80$ ,  $\sigma = 4$  mho/m.

to path length difference between the direct and reflected rays (first term of equation (2.3)). The phase shift introduced by the surface itself (second term of equation (2.3)) is illustrated in figures 2.6 and 2.7 as a function of  $\psi$ ,  $\lambda$  and polarization.

The total phase shift in the reflected path is given by

$$\alpha = \frac{2\pi}{\lambda} \delta_0 + \phi \quad (2.3)$$

where the path length difference  $\delta_0$  is calculated below with reference to figure 2.3:

$$\begin{aligned} \delta_0 &= (R_1 + R_2) - R \\ &= [(h_T + h_R)^2 + G^2]^{1/2} - [(h_T - h_R)^2 + G^2]^{1/2} \\ &= G \left[ \left( \frac{h_T + h_R}{G} \right)^2 + 1 \right]^{1/2} - \left[ \left( \frac{h_T - h_R}{G} \right)^2 + 1 \right]^{1/2} \end{aligned}$$

However, we have the series expansion

$$(1 + x^2)^{1/2} = 1 + \frac{1}{2} x^2 - \frac{1}{8} x^4 + \dots$$

Also noting that

$$x^4 = \left( \frac{h_T \pm h_R}{G} \right)^4$$

will be very small for the low elevation case (since  $G \gg (h_T \pm h_R)$ ), this and all remaining terms may be discarded without significant error.

Therefore, we have:

$$\begin{aligned} \delta_0 &= G \left\{ \left[ \frac{1}{2} \left( \frac{h_T + h_R}{G} \right)^2 + 1 \right] - \left[ \frac{1}{2} \left( \frac{h_T - h_R}{G} \right)^2 + 1 \right] \right\} \\ &= \frac{2 h_T h_R}{G} \quad (2.4) \end{aligned}$$



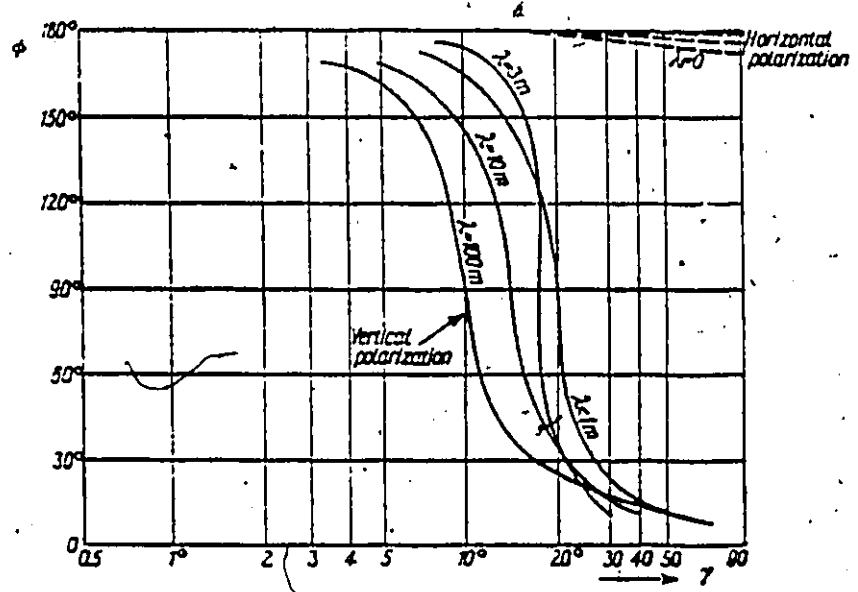


Figure 2.6 Phase  $\Phi$  of the reflection coefficient of a perfectly plane earth.  $\epsilon/\epsilon_0 = 10, \sigma = 10^{-6}$  mho/m.

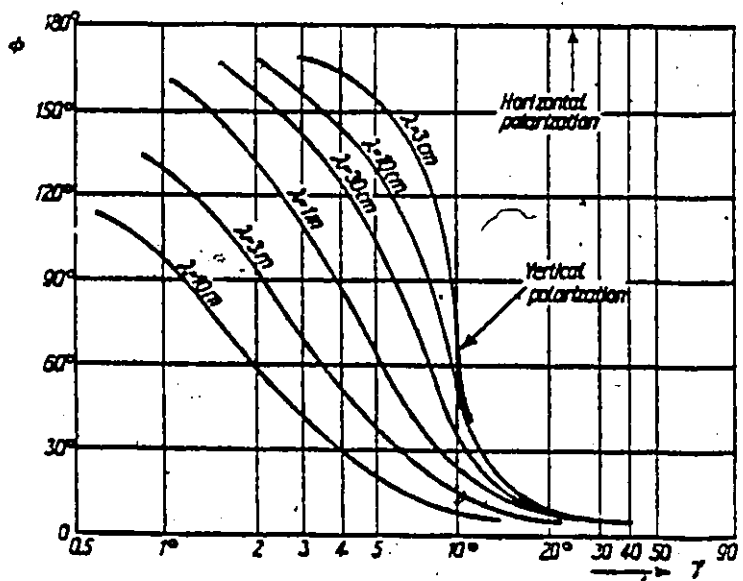


Figure 2.7 Phase  $\Phi$  of the reflection coefficient of a very smooth sea.  $\epsilon/\epsilon_0 = 80, \sigma = 4$  mho/m.

Another factor to be considered is that of the antenna gain. The antenna gain varies with look angle, and as such, it determines the extent to which a particular receiver will be affected by multipath reflections. Representing the antenna gain pattern by  $f(\theta)$ , we can modify equation (2.1) to account for the antenna look angle, as follows:

$$E = A_d f(\theta_d) + A_r f(\theta_r) e^{-j\alpha} \quad (2.5)$$

Specular reflection occurs within the first fresnel zone if the surface height difference  $\Delta h$  meets the Rayleigh criterion

$$\Delta h < \frac{1}{8} \frac{\lambda}{\sin \psi} \quad (2.5)$$

The first fresnel zone is that area of the surface for which  $(\delta - \delta_0) < \lambda/2$ ; where  $\delta_0$  is the path length difference for reflection at the theoretical specular reflection point  $x_0 = h_r \cot \psi$  (see figure 2.8) and  $\delta$  is the path length difference resulting from reflection at any other point on the surface.

According to reference [8], the strength of the specular component may be better represented by including the root mean square (rms) specular scattering coefficient  $\rho_s$ , such that the surface reflection coefficient is  $\rho = \rho_0 \rho_s$  where

$$\rho_s^2 = \exp \left[ - \left( \frac{4\pi\sigma_h \sin\psi}{\lambda} \right)^2 \right] \quad (2.7)$$

Here the rms surface height variation is given by  $\sigma_h$  which is assumed to have a Gaussian or normal distribution [9].

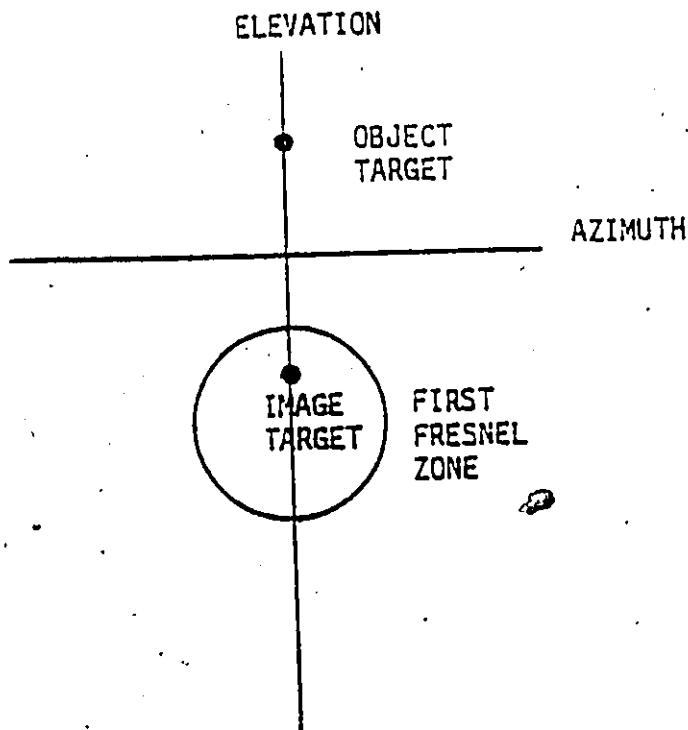


Figure 2.3: The first fresnel zone from which specular reflection may occur.

### 2.3 Diffuse Scattering

The "glistening surface" (Figure 2.9) is the area from which most of the scattered power may be observed. By scattered power we mean that power which has not been absorbed or specularly reflected by the surface. This surface may be idealized as a homogeneous, normal distribution of small facets with rms slope  $\sigma_a = 2\sigma_h/d_c$ , where  $\sigma_h$  and  $d_c$  are the rms surface height deviation and correlation distance respectively.

The glistening surface consists of that area for which radiation incident at angle  $\psi$  reflects to the radar by way of a facet having slope  $\leq \sigma_a$ .

As in the specular reflected case the reflection coefficient is

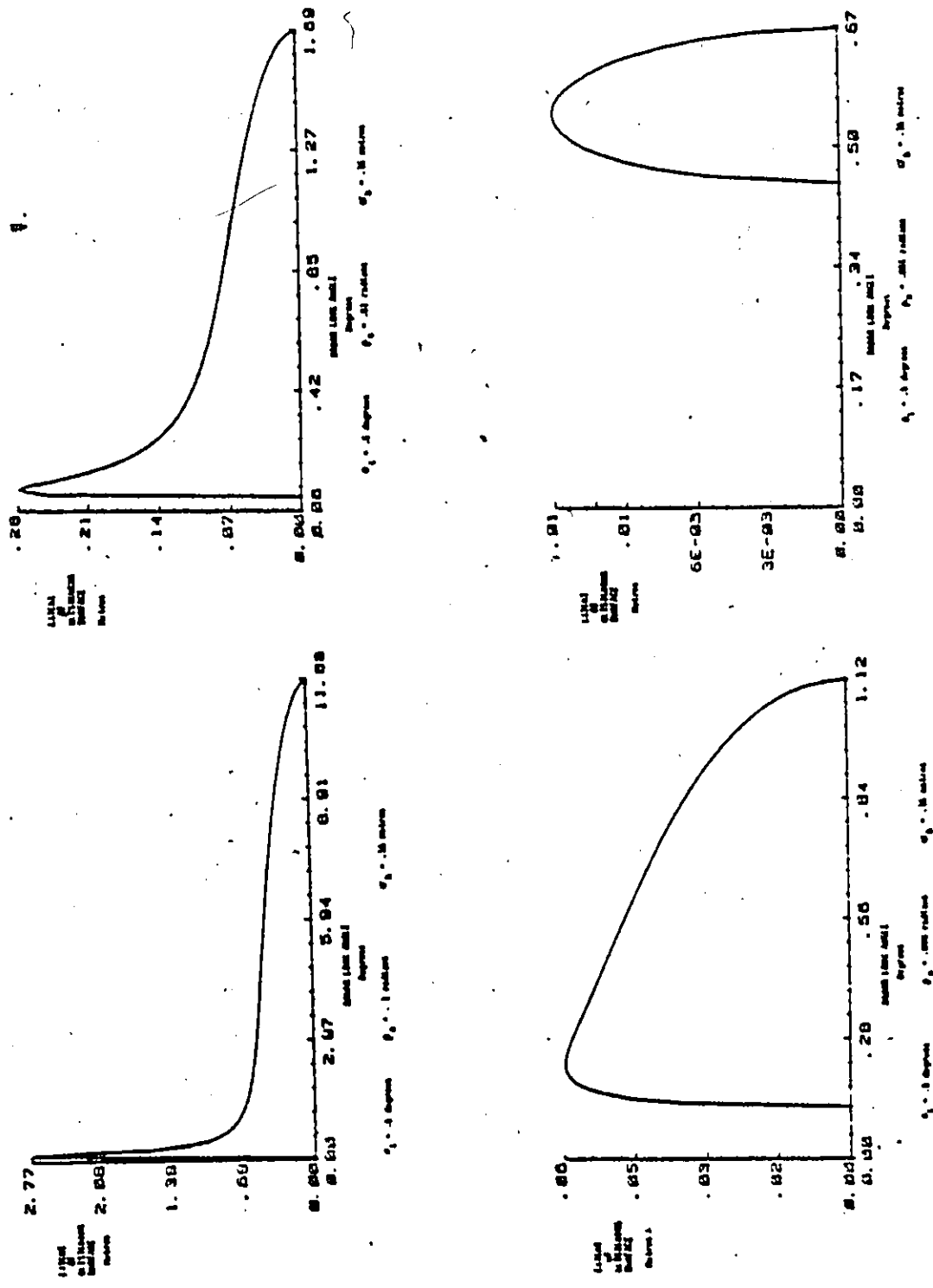


Figure 2.9 Various forms of the glistening surface from which diffuse reflections may occur.

modified by means of the diffuse scattering coefficient  $\rho_d$  such that  $\rho = \rho_0 \rho_d$  where  $\rho_d$  is commonly taken to be a function of  $(\sigma_h/\lambda \sin \psi)$ . A comparison of the diffuse and specular scattering coefficients is given in Figure 2.10.

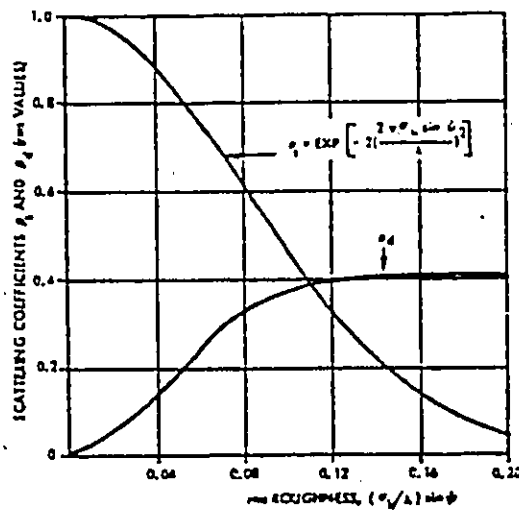


Figure 2.10 Specular and diffuse scattering coefficients versus roughness

Assuming the target to be an isotropic beacon, the power received along a direct path is given by the beacon equation:

$$P_r = \frac{P_t G_t}{4\pi R^2} A_r \quad (2.8)$$

where  $P_t$  is the transmitted power,  $G_t$  is the transmitter gain,  $A_r$  is the receiver aperture, and  $R$  is the target range. Since the receiver aperture,  $A_r$ , can be written in terms of receiver gain and wavelength as  $G_r \lambda^2/4\pi$ , and the transmitter gain is unity for an isotropic radiator, we can rewrite equation (2.8) as:

$$P_r = \frac{P_t G_r \lambda^2}{(4\pi)^2 R^2} \quad (2.9)$$

Let us now consider the small surface area  $dS$  to be a radiator with transmitted power  $dP_{t_s}$

$$dP_{t_s} = \frac{P_t \lambda^2 dG_S}{(4\pi)^2 R_1^2} \quad (2.10)$$

and gain

$$dG_S = \sigma^0 dS$$

where  $\sigma^0$  is the radar cross-section of the surface. This surface will thus contribute  $dP_c$  of clutter power to the radar at a distance  $R_2$  where:

$$dP_c = \frac{G_r P_t \lambda^2 \sigma^0 dS}{(4\pi)^3 R_1^2 R_2^2} \quad (2.11)$$

For further analysis, it is convenient to express this clutter power in terms of the diffuse scattering coefficient  $\rho_d$  [9].

$$d\rho_d^2 \equiv \frac{dP_c}{P_r} = \left(\frac{R}{R_1 R_2}\right)^2 \frac{\sigma^0}{4\pi} dS \quad (2.12)$$

Note that the cancellation of receiver gain  $G_r$  implies that the receiver is a uniform gain, omni-directional antenna. Assume the surface to be a uniform distribution of facets having rms slope  $\sigma_\alpha$  (this is the case for  $\rho_s = 0$ ), the glistening surface can be characterized by  $\sigma^0 = \cot^2 \sigma_\alpha$  for  $\beta \leq \sigma_\alpha$  and zero for  $\beta > \sigma_\alpha$ , where  $\beta = (\psi_2 - \psi_1)/2$ . The glistening surface may be represented in Cartesian coordinates by the following

Equation

$$y = \pm \frac{x_1 x_2}{x_1 + x_2} \left( \frac{h_r}{x_1} + \frac{h_t}{x_2} \right) \left( \sigma_\alpha^2 - \frac{1}{4} \left( \frac{h_r}{x_1} - \frac{h_t}{x_2} \right)^2 \right)^{1/2} \quad (2.13)$$

Figure 2.11 illustrates the glistening surface coordinates where  $x_1 + x_2 = G$  and  $R_1 = x_1$ ,  $R_2 = x_2$  and the glistening surface is bounded in  $x$  by  $x_a = h_r/2\sigma_\alpha$  and  $x_b = R - x_a$ . The total diffuse power can be derived by integrating equation (2.12) over the glistening surface. However, the integration may be in  $x$  alone by noting that the integrand will be relatively constant over  $y$  for a given  $x$ . Noting that since the surface is symmetrical in  $y$ , we have  $ds = 2ydx$ . Setting  $R_1 = x_1$ ,  $R_2 = x_2$  and  $\sigma_o = 1/\sigma_\alpha^2$  (since  $\cot^2 \sigma_\alpha = 1/\sigma_\alpha^2$ ) in equation (2.12), we have:

$$P_d^2 = \frac{R^2}{2\pi\sigma_\alpha^2} \int_{x_a}^{x_b} \frac{ydx}{(R-x)^2 x^2} \quad (2.14)$$

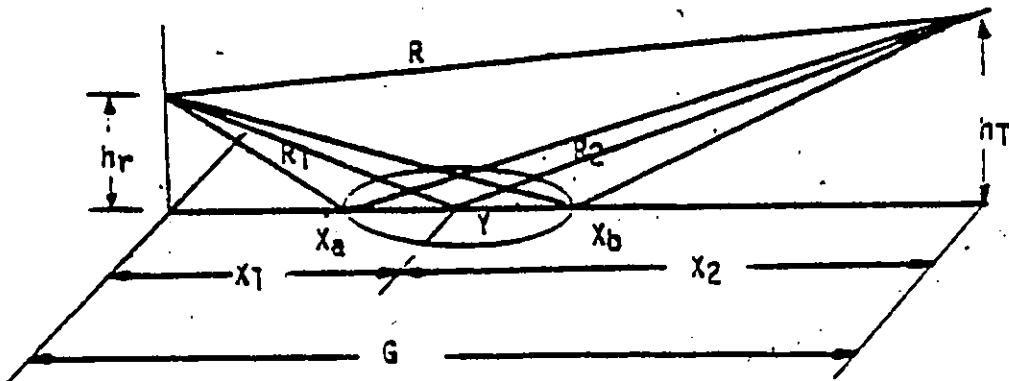


Figure 2.11 Glistening surface geometry of diffuse multipath.

#### 2.4 Diffuse Roughness Masking

It is, in general, necessary to consider the contributions of both specular and diffuse multipath alike, since in practice few surfaces will result in these two extreme cases. It is for this reason that Barton [9] has introduced the roughness factor  $F_d^2$  to scale the diffuse component.

$$F_d^2 = 1 - \rho_s^2 \quad (2.15)$$

As can be seen in equation (2.15),  $F_d^2$  represents that fraction of reflected power not attributed to the specular component. From equation (2.7), we see that  $\rho_s^2$  is, however, a function of  $\psi$ , the grazing angle for specular reflection. In the diffuse case, the incident angle and the reflecting angle  $\psi_2$  are not necessarily equal; for this reason,  $\rho_s^2$  must be calculated to accommodate both. Taking the geometric mean of the two paths, we have

$$F_d^2 = F_{d1} F_{d2} = \sqrt{(1 - \rho_{s1}^2)(1 - \rho_{s2}^2)} \quad (2.16)$$

where the subscripts 1 and 2 correspond to the contribution of the incident and reflected paths.

Equation (2.14) may now be updated to include the roughness factor.

$$\rho_d^2 = \frac{R^2}{2\pi\sigma_\alpha^2} \int_x^{x_b} \frac{F_d^2 y dx}{(R-x)^2 x^2} \quad (2.17)$$

It is perhaps more instructive to view the power  $\rho_d^2$  as a function of the receiver look angle  $\theta$ . This may be accomplished by making the substitution below.



$$x = h_r \tan \theta$$

$$dx = -h_r \csc^2 \theta d\theta$$

$$\theta_a = \tan^{-1} (h_r/x_a) \quad \theta_b = \tan^{-1} (h_r/x_b)$$

The term  $\rho_d^2$  can now be written as

$$\begin{aligned} \rho_d^2 &= \frac{-R^2}{2\pi\beta^2} \int_{\theta_a}^{\theta_b} \frac{F_d y h_r \csc^2 \theta}{\left(R - \frac{h_r}{\tan \theta}\right)^2 \frac{h_r^2}{\tan^2 \theta}} d\theta \\ &= \frac{-R^2}{2\pi h_r \beta_o^2} \int_{\theta_a}^{\theta_b} \frac{F_d y d\theta}{(R - h_r \cot \theta)^2 \cos^2 \theta} \end{aligned}$$

Since  $x_b > x_a$ ;  $\theta_a > \theta_b$ ; therefore, reversing the limits, we have

$$\rho_d^2 = \frac{R^2}{2\pi h_r \beta_o^2} \int_{\theta_b}^{\theta_a} \frac{F_d y d\theta}{(R - h_r \cot \theta)^2 \cos^2 \theta} \quad (2.18)$$

Equation (2.18) can be written in the form of eq. (2.19) below.

$$\frac{d\rho_d^2}{d\theta} = \frac{R^2}{2\pi h_r \beta_o^2} \left[ \frac{F_d y}{(R - h_r \cot \theta)^2 \cos^2 \theta} \right] \quad (2.19)$$

Note that equation (2.19) is the slope of  $\rho_d^2$ , and that  $\rho_d^2 = 0$  for  $\theta_a < \theta < \theta_b$ . It is now possible to construct a curve representing the reflection coefficient  $\rho_d = (\rho_d^2)^{1/2}$ . This is done by averaging the slope of  $\rho_d^2$  over  $N$  small intervals of size  $\Delta\theta$ . The next value of  $\rho_d(i+1) = \rho_d(i) + (\text{mean } (d\rho_d^2/d\theta) \times \Delta\theta)^{1/2}$ , where  $\rho_d(0) = 0$  and  $\rho_d(N) = \rho_{d\text{total}}$ . In this way we may arrive at a value for the total diffuse power.

## CHAPTER 3

### SIMULATION TECHNIQUES

#### 3.1 The Simulation of Multipath

In this chapter, we shall discuss three possible methods of simulating multipath. Section 3.2 describes a holographic method in which the amplitude and phase information required to simulate a multipath environment is recorded on a holographic plate. A microwave source may be transmitted through or reflected from this plate, producing the desired multipath wavefront. A phased array approach is discussed in Section 3.3. In this case, discrete elements are used to approximate the numerous reflections associated with diffuse multipath. This section is then followed by one on a hybrid simulation system in which the numerous radiators are obtained experimentally from a single source, then combined by means of software to produce any number of diffuse environments. It should be noted that a pure software simulation has been excluded, because of the desire to test the response of an actual array (and its own specific imperfections) to the impending multipath.

#### 3.2 Holographic Approach to the Synthesis of Multipath

The extension of holography to the microwave frequencies of the electromagnetic spectrum seems to offer new possibilities for the solution of a number of problems such as antenna synthesis [10]. The

concept of holography has been around for quite some time. A number of years prior to 1947, Dennis Gabor photographically recorded the interference pattern, generated by the interaction of scattered quasi-monochromatic light from an object and a coherent reference wave [11]. Reconstruction of the original wavefront was then achieved by defraction of coherent light through the developed holographic transparency. "Hologram" was the description label Gabor put on these transparencies, taken from the greek word "holos", meaning whole. This was a fitting name, since a hologram retains all the information contained in the original signal.

The extension of holography to the microwave frequencies, being a conceptually trivial matter, has the practical limitation that there is to date no microwave analog to photography. That is not to say that it is impossible to generate microwave holograms; it is just that it is more difficult than in the optical case. The remainder of this section will, for the above mentioned reasons, be dedicated to summarizing the theory behind the possible techniques used in acquiring microwave hologram.

As in optical holography, it is desired to record only the modulus of the interference pattern of interest, since the phase information is encoded in the modulus. Assume we have a plane in  $x$  and  $y$  upon which a hologram is to be constructed. The reference wave  $E_R$  (in the far field of this plane) is given in equation (3.1):

$$E_R(x,y) = A_R \cos(\omega t + \phi_R(x,y)) \quad (3.1)$$

The term  $A_R$  is the reference signal's amplitude, while  $\phi_R(x,y)$  is its

phase which varies spatially, as given by equation (3.2):

$$\phi_R(x,y) = \frac{2\pi}{\lambda} [x \sin\theta_A + y \sin\theta_E] \quad (3.2)$$

where  $\theta_A$  and  $\theta_E$  are the azimuth and elevation angles (with respect to boresight) respectively. A wave scattered from an object (in our case a land or water surface) can be expressed as

$$E_O(x,y) = A_O(x,y) \cos(\omega t + \phi_O(x,y)) \quad (3.3)$$

Note that now both amplitude and phase are functions of position. Seen as a whole, both  $A_O(x,y)$  and  $\phi_O(x,y)$  will be extremely complex. If, however, we consider only the contribution of one point on the object, (azimuth =  $\theta_{A1}$ , elevation =  $\theta_{E1}$ ), we have

$$E_{O1}(x,y) = A_{O1} \cos(\omega t + \phi_{O1}(x,y)) \quad (3.4)$$

Now,  $A_{O1}$  will be a constant whose value depends only on the reflection coefficient of the surface at that point. The function  $\phi_{O1}(x,y)$  will once again be a simple function as in equation (3.5):

$$\phi_{O1}(x,y) = \frac{2\pi}{\lambda} [x \sin\theta_{A1} + y \sin\theta_{E1}] \quad (3.5)$$

For this analysis, we shall consider only the contribution of this one point source, noting that the total object will be represented by the sum of all contributing points.

It is the interference pattern of  $E_R(x,y)$  and  $E_{O1}(x,y)$  that is recorded to form a hologram. In the optical case, this is done with a photographic film which merely records the power of the interference. This process is equivalent to squaring and low-pass filtering [11] the interference electric field  $E_I$  of equation (3.6):

$$E_I(x,y) = E_R(x,y) + E_{O1}(x,y) \quad (3.6)$$

The intensity pattern is calculated as follows

$$\begin{aligned}
 E_I(x,y)^2 &= [E_I(x,y) + E_{O1}(x,y)]^2 \\
 &= [A_R \cos(\omega t + \phi_R(x,y)) + A_{O1} \cos(\omega t + \phi_{O1}(x,y))]^2 \\
 &= [A_R^2 \cos^2(\omega t + \phi_R(x,y)) \\
 &\quad + 2A_R A_{O1} \cos(\omega t + \phi_R(x,y)) \cos(\omega t + \phi_{O1}(x,y)) \\
 &\quad + A_{O1}^2 \cos^2(\omega t + \phi_{O1}(x,y))]
 \end{aligned}$$

But

$$\cos^2 \alpha = \frac{1}{2} (1 + \cos 2\alpha)$$

and

$$\cos \alpha \cos \beta = \frac{1}{2} \cos(\alpha - \beta) + \frac{1}{2} \cos(\alpha + \beta)$$

Therefore,

$$\begin{aligned}
 E_I(x,y)^2 &= \frac{A_R^2}{2} (1 + \cos(2\omega t + 2\phi_R(x,y))) \\
 &\quad + A_R A_{O1} (\cos(\phi_R(x,y) - \phi_{O1}(x,y))) + \frac{A_{O1}^2}{2} (1 + \cos(2\omega t + 2\phi_{O1}(x,y)))
 \end{aligned}$$

A low-pass filter removes all but the constant terms, giving the intensity

$$I(x,y) = \frac{A_R^2}{2} + A_R A_{O1} \cos(\phi_R(x,y) - \phi_{O1}(x,y)) + \frac{A_{O1}^2}{2} \quad (3.7)$$

It can now be seen that the amplitude and phase of the object signal are preserved in the second term of equation (3.7). It is an important observation that the other two terms are constant for all points  $x$  and  $y$  on the hologram, since only the phase of the second term is a function of  $x$  and  $y$ .

The effect of the first and third terms of equation (3.7) is only

to add a constant brightness to the hologram. This brightness is a quantity contributing to a term known as the fringe visibility [11], given by:

$$v \equiv (I_{\max} - I_{\min}) / (I_{\max} + I_{\min})$$

where from equation (3.7)

$$I_{\max} = \frac{A_R^2}{2} + A_R A_{oi} + \frac{A_{oi}^2}{2}$$

$$I_{\min} = \frac{A_R^2}{2} - A_R A_{oi} + \frac{A_{oi}^2}{2}$$

Therefore,

$$v = \frac{2 A_R A_{oi}}{(A_R^2 + A_{oi}^2)} \quad (3.8)$$

The amplitude transmittance of a hologram is proportional to  $I(x,y)$ , and therefore the reconstructed wave  $E_N$  is given by equation (3.9), the product of the intensity pattern and the reference wave:

$$E_N(x,y) = I(x,y) E_R(x,y) \quad (3.9)$$

$$= A_R \cos(\omega t + \phi_R(x,y)) \left[ \frac{A_R^2}{2} + A_R A_{oi} \cos(\phi_R(x,y) - \phi_{oi}(x,y)) + \frac{A_{oi}^2}{2} \right]$$

$$= \frac{A_R^3}{2} \cos(\omega t + \phi_R(x,y)) + [A_R^2 A_{oi} \cos(\phi_R(x,y)$$

$$- \phi_{oi}(x,y)) \times \cos(\omega t + \phi_R(x,y))] + \frac{A_R A_{oi}^2}{2} \cos(\omega t + \phi_R(x,y))$$

$$\begin{aligned}
&= \frac{A_R}{2} [A_R^2 + A_{oi}^2] \cos(\omega t + \phi_R(x,y)) + \frac{A_R^2 A_{oi}}{2} \cos(\omega t + \phi_{oi}(x,y)) \\
&\quad + \frac{A_R^2 A_{oi}}{2} \cos(\omega t + 2\phi_R(x,y) - \phi_{oi}(x,y)) \tag{3.10}
\end{aligned}$$

The above hologram will have three beams. The first represented by term one of equation (3.10) will be a scaled version of the reference beam and occurring at the same azimuth and elevation. The other two terms are the sidebands situated symmetrically in phase about the reference beam. The ratio of sideband to reference amplitude is  $v/2$ , which will have a maximum value of 0.5 when the reconstructive and object wave amplitude  $A_R$  and  $A_{oi}$  are equal. It is these side-band terms which contain all the information of the original object wave. The third term of equation (3.10), the conjugate wave, has complementary phase information and as such, it is undesirable. Only the second term is of the correct form and is the only signal we wish to see. It is possible to separate the second beam by making  $\phi_R(x,y)$  large when forming the hologram.

In the following, two methods of producing microwave holograms are briefly described.

An experiment apparatus for the recording of microwave holograms is illustrated in Fig. 3.1. The receiver of Fig. 3.1 is moved about a two dimensional plane which is to become the plan of the hologram. The interference intensity pattern resulting from the reference and object antenna are recorded for a suitably large number of points to accommodate accurate interpolation when constructing the resultant

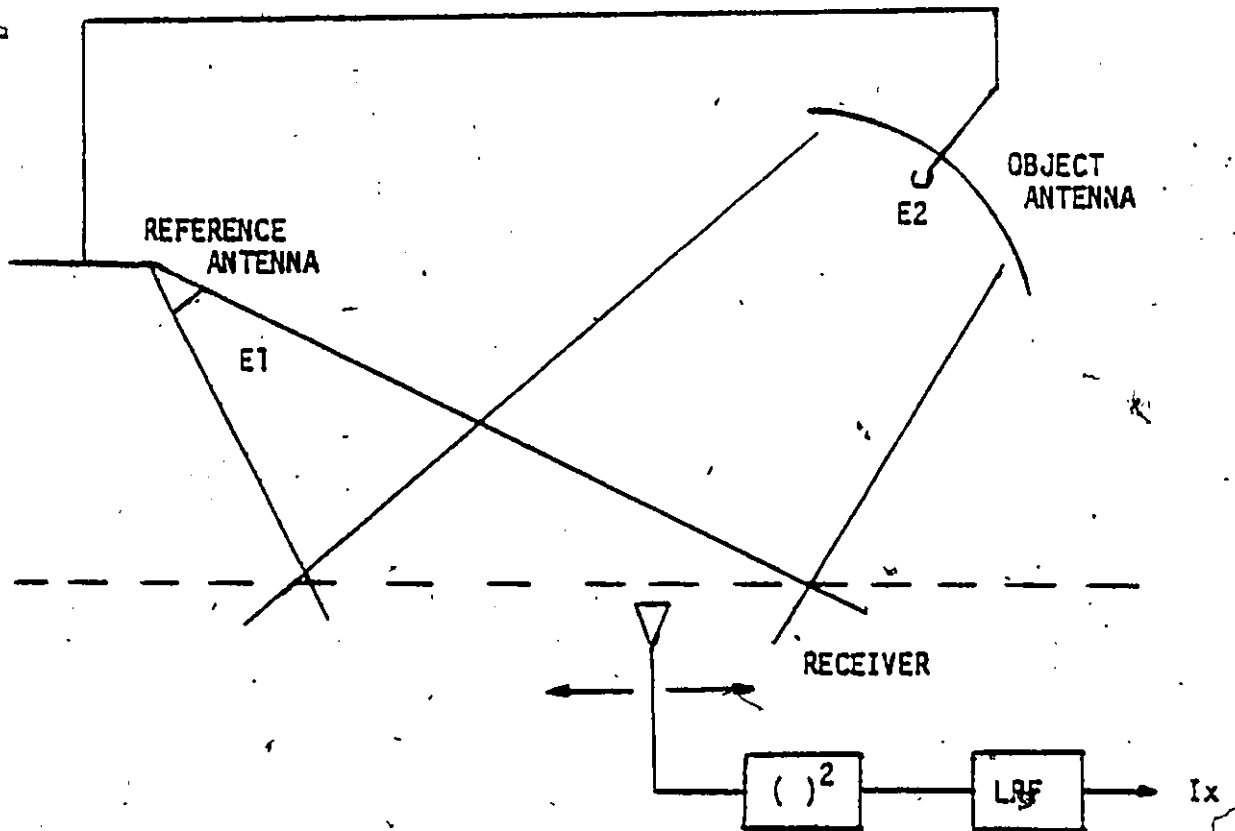


Figure 3.1 Holographic recording apparatus.



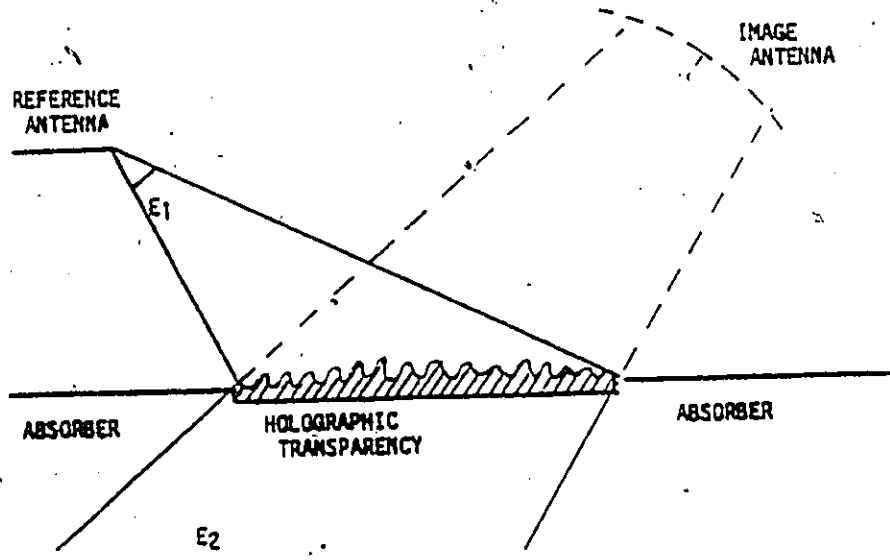



Figure 3.2 Holographic reproduction of the object antenna of Figure 3.1.



hologram can be constructed with a plate of variable attenuation or phase, having a profile equal to that of the recorded interference pattern. Figure 3.2 shows the resulting reconstruction of the object antenna. A recent paper by N.H. Farhat [12] describes another method of producing amplitude and phase modulating microwave transparencies. A short summary of the technique is as follows; the wavefront to be spatially modulated radiates on a thin semiconductor plate. The plate initially having uniform thickness and resistivity, is altered by means of excess carrier generation by photoexcitation or electron beam carrier injection. The electromagnetic properties of the plate change as a result and exhibit a change in reflection and transmission coefficients [12]. Phase modulation can be obtained through a process known as relief grating, where the apparent phase modulation is due to difference in path lengths derived by reflection of the reference beam off grating of various depths.

The elegance of holography in reproduction of a realistic multipath environment becomes most obvious when we consider the fact that holograms being mere amplitude records are easily added to one another producing a superposition of the holographic images. The multipath signal as developed in Chapter 2 may be viewed as the sum of numerous radiators from various angles and having different amplitudes. A hologram can be developed, through the composition of holograms representative of these numerous radiators. This transparency may then be used to radiate a full multipath signal in real time with the use of a single transmitter (the reference signal).

### 3.3 The Phased Array Multipath Simulator

Another possibility for the simulation of multipath in real time is the phased array transmitter. This method is without a doubt the direct approach. Assuming multipath to be the net result of numerous radiators of the form given in equation 3.4, it is theoretically possible to physically simulate their individual contributions. It is merely required to provide the necessary hardware to accommodate variations in the phase and amplitude of each radiator. Figure 3.3 illustrates the hardware requirements of one such radiator.

In a complete system, the radiators would be arranged in such a fashion that the angular assignments of the array element corresponded to the angular extents of the glistening surface as illustrated in Fig. 3.4.

### 3.4 The Hybrid Multipath Simulator

In this context, the word hybrid is used to describe a system which has a hardware basis, but uses the versatility of software to achieve a flexible system. Once again we assume the multipath signal to be composed of many radiating elements of various amplitudes and phases. It is then not only possible to consider discrete radiators additively creating the multipath environment, but to monitor these contributions individually. After all the elements have been considered their contributors are added through software. What we are actually producing is a synthetic aperture transmitter where the discrete radiators, found in

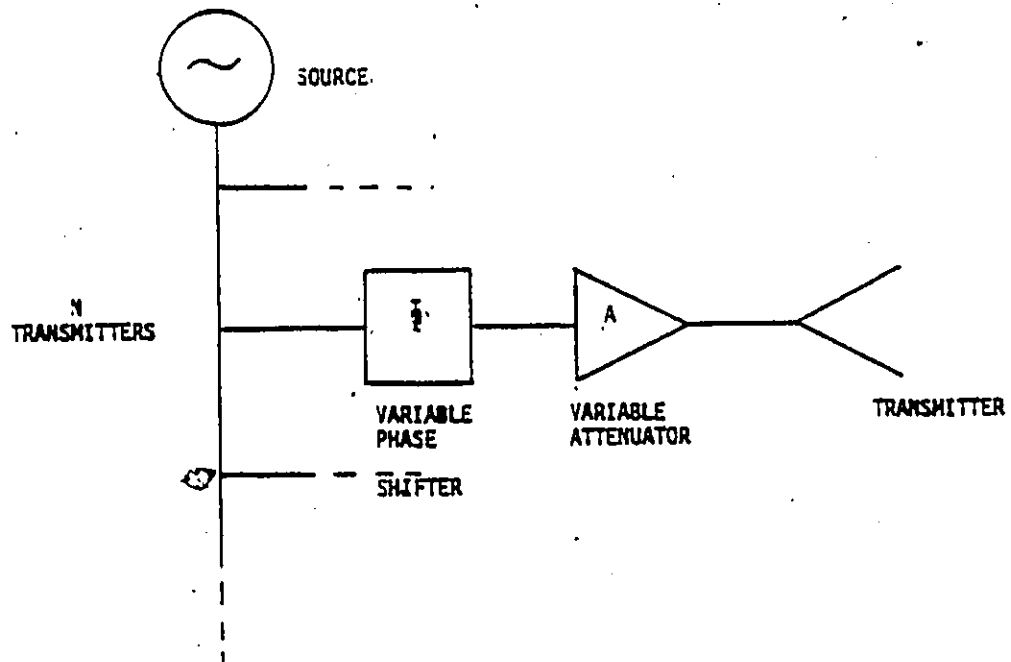


Figure 3.3 Phased array multipath simulation transmitter.

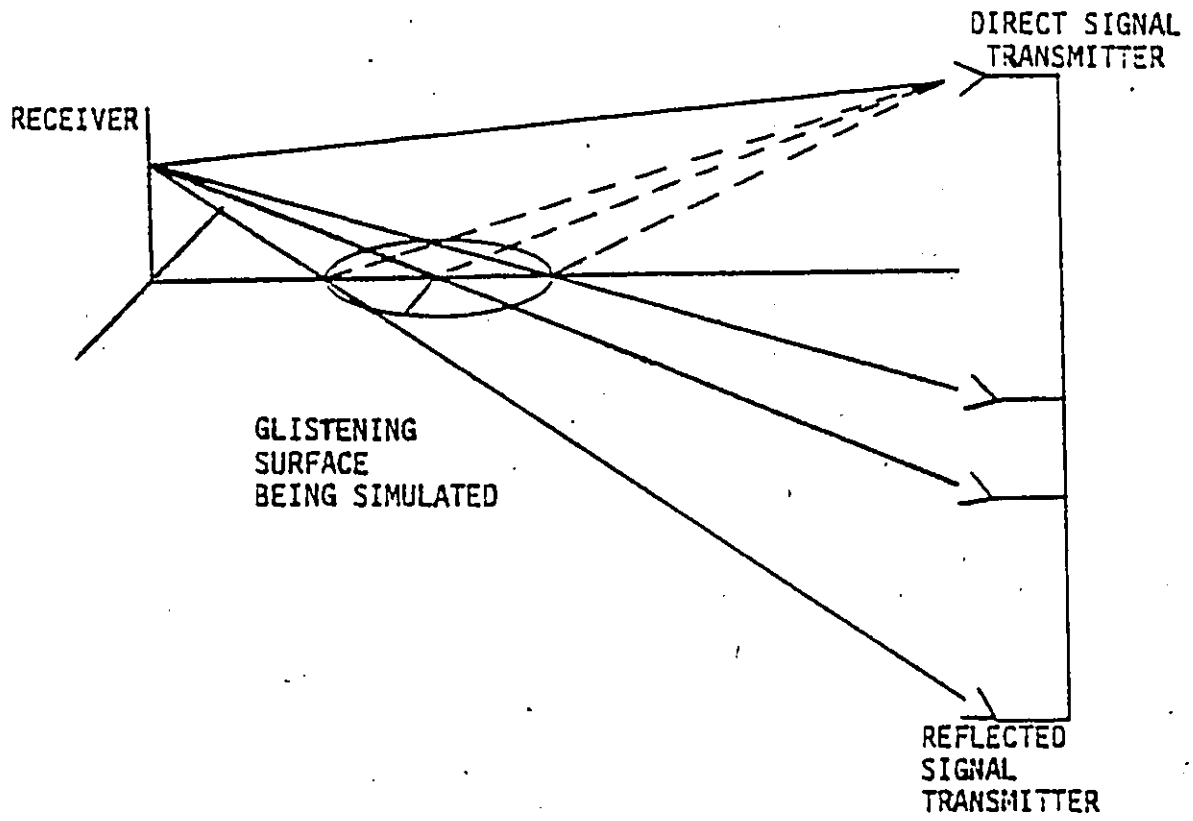


Figure 3.4 Overview of complete phased array multipath simulator.

the phased array of the last section, have now been spaced in time.

The hybrid system was chosen as the simulation method used; the merits of this system resulting in this decision are discussed in the following section.

### 3.5 Merits of Hybrid Simulation

Although the hybrid method has the limitation that it cannot simulate multipath in real time, it has a number of advantages which make it a desirable method. Probably the most obvious limitation of both the phased array and holographic method are their required physical size. For instance, a typical multipath may have an angular distribution of ten degrees; then the phased array and holographic plate would both have a physical extent of seven feet (based on an anechoic chamber length of forty feet). Not only would this extent be outside the quiet zone of the chamber but the required hardware for both methods would be incredibly expensive. For these reasons it can be seen that the hybrid approach is the obvious choice.

## CHAPTER 4

### HYBRID SYSTEM FEATURES

#### 4.1 Overview

It has been shown earlier in this thesis that diffuse multipath may be modelled as the net sum of numerous radiating elements distributed over a wide range of angles. It was desired to test the response of an actual receiver to a diffuse wavefront. Realization of a diffuse multipath transmitter in hardware being extremely expensive and virtually impossible to implement led to the hybrid simulator. The hybrid simulator described in this chapter combines the ability to use a real receiver and still be able to simulate almost any number of transmitters accurately and cheaply.

#### 4.2 Hardware

A block diagram of the hybrid system is shown in Fig. 4.1. The microwave hardware is as follows. The klystron source is split to provide transmitter and receiver power. The phase of the transmitted signal is varied relative to the in-phase local oscillator of the receiver via  $d_2$ . This signal is then amplified to a sufficient level before being transmitted from a 25 dB horn 40 feet from the receiving array. The receiving array consists of eight 10. dB horns. The quadrature oscillator supplying these horns has phase shifter  $d_1$  to provide the appropriate phase shifting with respect to the in-phase oscillator.

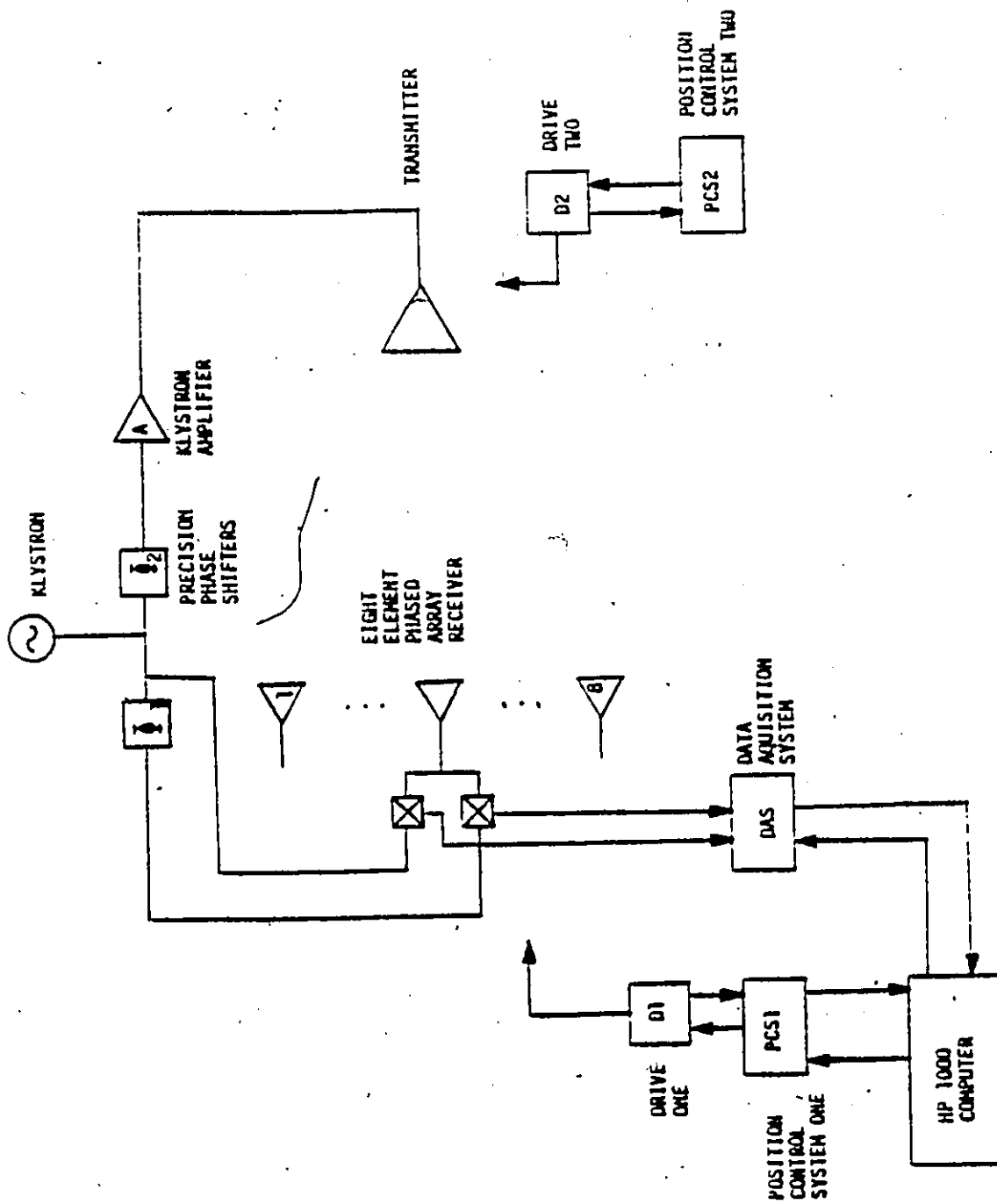


Figure 4.1 Block diagram illustrating the hybrid multipath simulator's major hardware components.



The depression angle with respect to the receiver boresight is obtained by elevation of the transmitter and/or tilting the receiver. The desired angle is either entered manually into position control system two (PCS2) for transmitter position control or under computer control into PCS1 for receiver control. A detailed description of the above mentioned system components and others can be found in Appendix A.

#### 4.3 Software

The software for this system is divided between four programs. The first program "DVS72" (Appendix B) is used to acquire data from the phased array receiver. This program interfaces the hardware and software of the hybrid system. This interface involves data collection, receiver position control, and necessary user prompts to provide essential hardware adjustments.

The second program "ADJUST", described in Appendix B, is used to make the required data adjustments. These adjustments account for nonuniform channel gains, phases and offsets. The next program "DFGEN" generates the appropriate surface reflection characteristics, used to shape the acquired data. The last program "SHAPE" applies the reflection coefficients of "DFGEN" to the data of "DVS72". It also provides the characteristic phase distribution of diffuse multipath and displays the final data format.

A detailed description and listing of the above mentioned programs can be found in Appendix B.

## CHAPTER 5

### RESULTS

#### 5.1.1 Theoretical

In Chapter 2 the nature of diffuse multipath was presented in a mathematical sense, developed from a physical model of a surface. It was found that the resulting equation (2.19) described the diffuse power reflected into the receiver from a surface area contained within the small look angle sweep of  $d\theta$ . This equation being a composite of many factors such as; the extent of the glistening surface in the y-axis, the roughness factor and the target geometry, made it difficult to visualize exactly how the diffuse multipath changes for a given set of parameters.

It is for this reason that the diffuse multipath versus look angle has been displayed by use of program "DF3DP" in a three dimensional format. This allows for one of the various contributing parameters to be varied along one axis with the remaining parameters being fixed. This gives us not only a picture of how the multipath characteristics vary for a given parameter, but also the sensitivity of these characteristics to varying one parameter, as compared to another.

In the following sections the diffuse reflection coefficient is displayed in 3-D for varying RMS surface slope, RMS surface height deviation and target elevation angle. In all plots the target range is 10 km, the wavelength 3 cm, and the radar is situated at a height of 5 m.

### 5.1.2 RMS Surface Slope

The five figures of this section (Figs. 5.1.2A-E) will be considered in two groups of three (Figs. 5.1.2 A, B, C) and (Figs. 5.1.2 D, B, E). Since the figures of this sections display a large amount of mutual information it is perhaps best to describe these feature first since they infact reveal the affects of varying  $\beta_0$  the RMS surface slope. There are two predominate features that are worthy of noting, they are the narrow peak and the wide fringe found in the right and left backgrounds respectively. The narrow peak occuring at small slopes, is to be expected since the extent of the glistening surface depends only on the target geometry and the slope of the reflecting surface. A patch of surface displaced far from the specular point requires a steeper sloped surface facet to reflect power in the direction of the receiver than does a point near the specular point. Since these surface facets are assumed to be normally disturbed, you would expect (ignoring all other facters) diffuse power to be reflected normally about the specular point. It should also be noted that the glisten surface width  $y$  is greater about the specular point, see Fig. 2.9.

As  $\beta_0$  increases the extent of the glistening surface increases from only .016 degrees at  $\beta_0 = .001$  radians to 45.0 deg at  $\beta_0 = .1$  radians. Since the behaviour of the reflection coefficient is relatively continuous for large look angles, the plots have only been made up to 1.0 degree. The fringe in the left back ground arises because as  $\beta_0$  increases the extent of the glistening surface increasing (i.e. from very small angles to very large angles). The actual amount of surface

area from which power can arrive is large ( $dx = -h_r \csc^2 \theta d\theta$ ) for small angles, it is also apparent that the extent of the glistening surface in the y axis increases tremendously for decreasing look angle. The combination of these two affects results in the observed fringe.

In order to investigate the effect of surface height deviation Figs. 5.1.2 A, 5.1.2 B and 5.1.2 C were plotted with respectively decreasing  $\sigma_h$ . The elevation angle was held constant at .5 degrees. It can be seen that the relative magnitude of the reflection coefficient increases for increasing  $\sigma_h$  this is due to the increasing roughness factor  $F_d$  equation 2.16. A more interesting feature, however, is the apparent exaggeration of features as  $\sigma_h$  decreases. It is interesting to note that percent difference between peaks and valleys is much greater when  $\sigma_h$  is small. This affect will be made clear in the RMS slope section (section 5.1.3).

If we now focus attention on figures 5.1.2 D, 5.1.2 B and 5.1.2 E, we can see the effect that various target elevation angles have on the nature of this distribution. Holding the RMS surface height deviation  $\sigma_h$  at .15 meters or  $5\lambda$  the plots of reflection coefficient versus look angle versus  $\beta_0$  were generated (Fig. D, B, E) for target elevation angles of 1.0, .5 and .25, respectively. Some features are quite obvious, those being the fact that the peak follows the specular point and the fringe increase in amplitude with respect to the peak. Some less obvious points are that the glistening surface extends over a greater angular range and that the diffuse reflect coefficient is larger when the elevation angle is larger. These points will be more easily seen in the section on elevation angle (section 5.1.4).

THE DIFFUSE REFLECTION COEFFICIENT VS. LOOK ANGLE FOR VARYING RMS SURFACE SLOPE

RMS SURFACE HEIGHT = .000000 metres TARGET ELEVATION = .500000 degrees

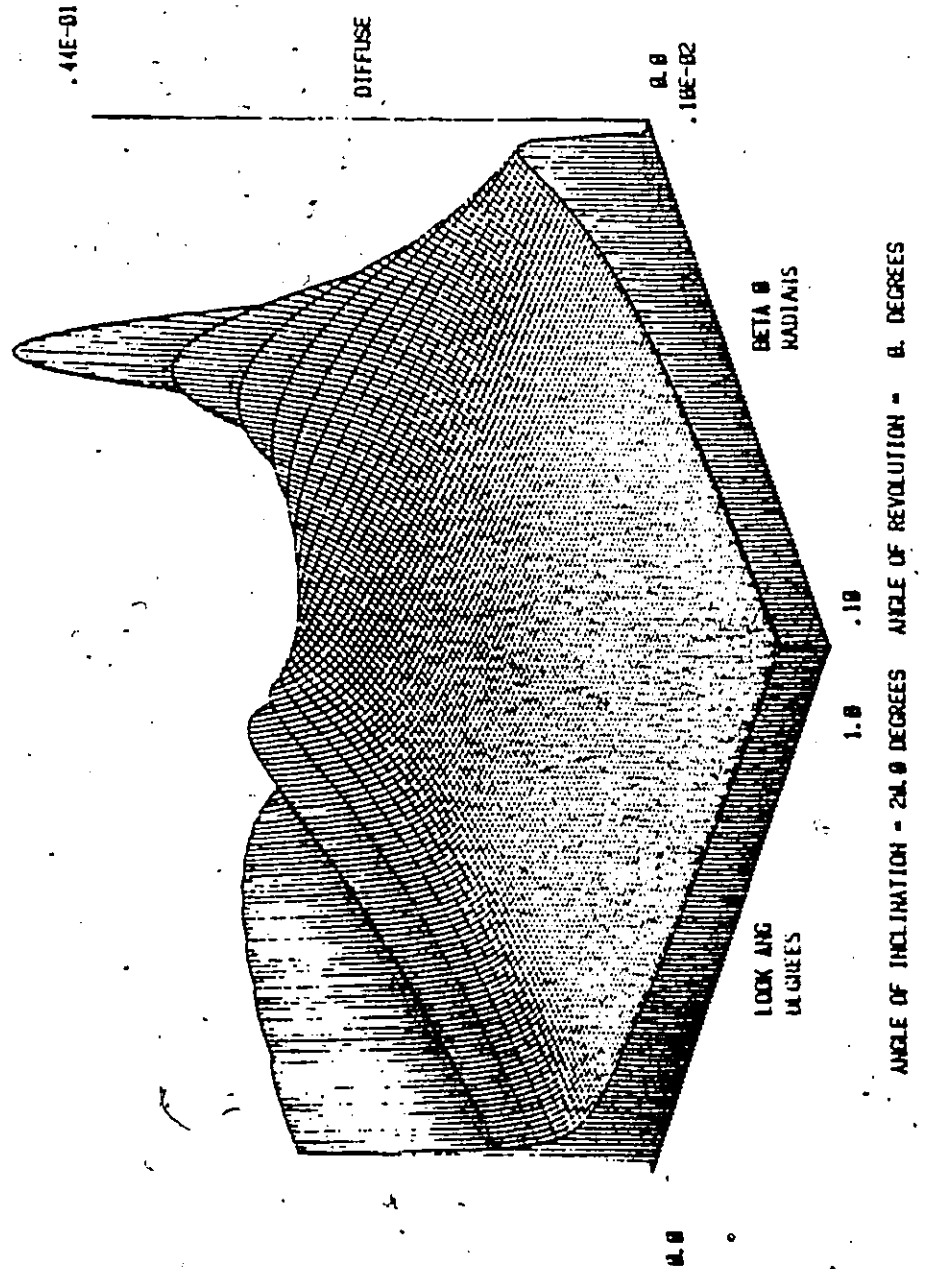
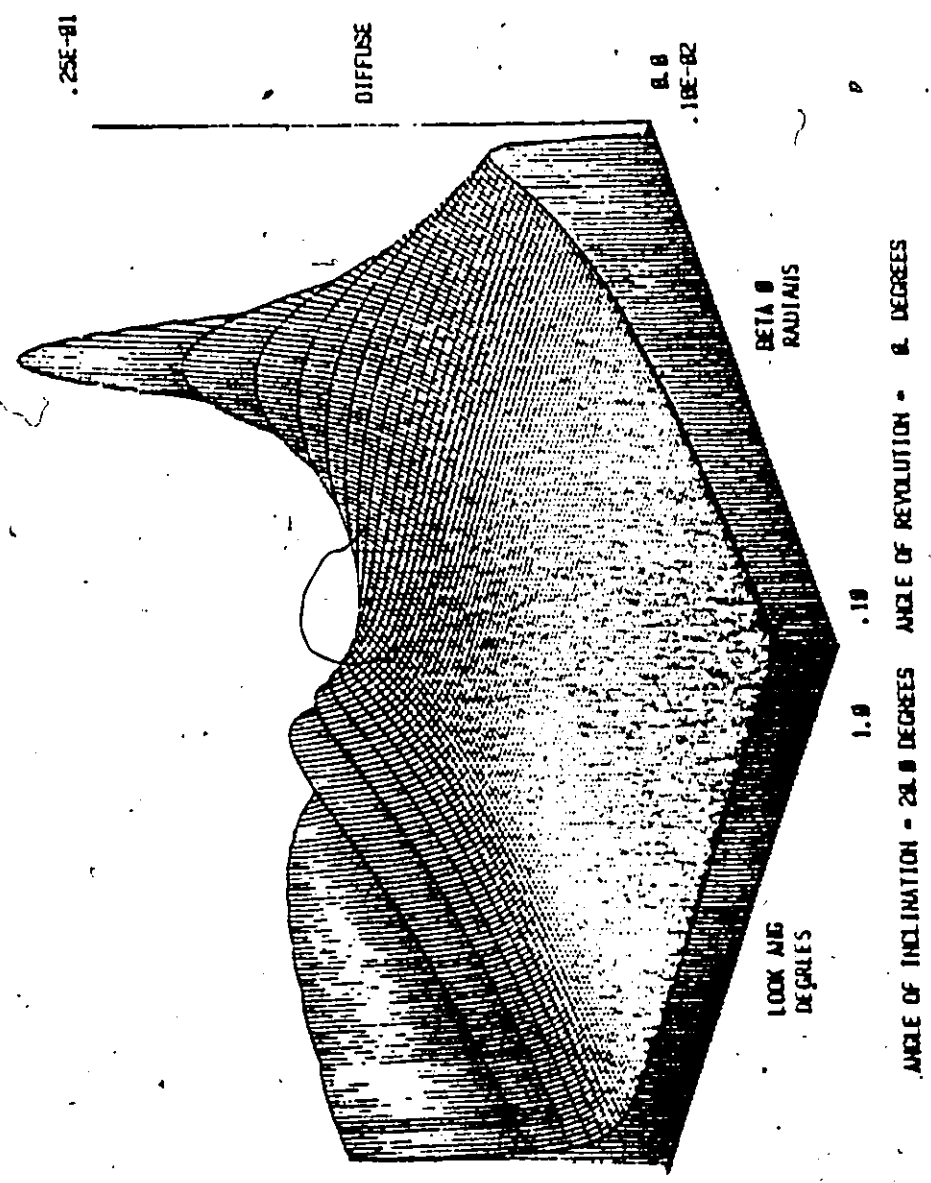


Figure 5.1.2.A The diffuse reflection coefficient versus look angle for varying RMS surface slope for a target elevation of  $\theta_t = .5$  degrees, and a surface height deviation of  $\sigma_h = .6$  metres.

THE DIFFUSE REFLECTION COEFFICIENT VS. LOOK ANGLE FOR VARYING RMS SURFACE SLOPE

RMS SURFACE HEIGHT = .150000 metres      TARGET ELEVATION = .500000 degrees



ANGLE OF INCLINATION = 20.0 DEGREES      ANGLE OF REVOLUTION = 0.0 DEGREES

Figure 5.1.2.3 The diffuse reflection coefficient versus look angle for varying RMS surface slope for a target elevation of  $\theta_t = .5$  degrees, and a surface height deviation of  $\sigma_h = .15$  metres.

THE DIFFUSE REFLECTION COEFFICIENT VS. LOOK ANGLE FOR VARYING RMS SURFACE SLOPE

RMS SURFACE HEIGHT = .037500 metres TARGET ELEVATION = .500000 degrees

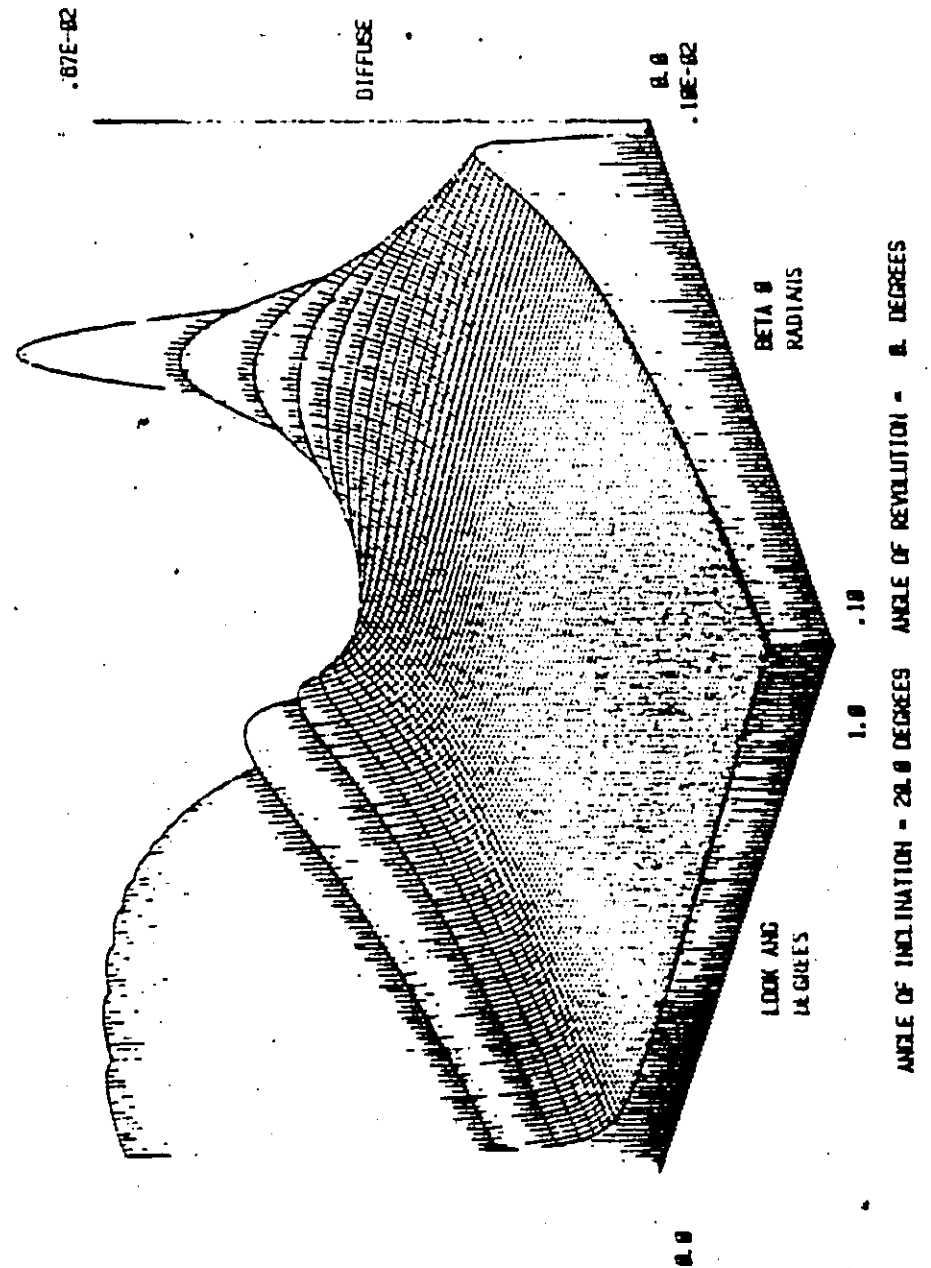


Figure 5.1.2.C The diffuse reflection coefficient versus look angle for varying RMS surface slope for a target elevation of  $\theta_t = .5$  degrees, and a surface height deviation of  $\alpha_H = .0375$  metres.

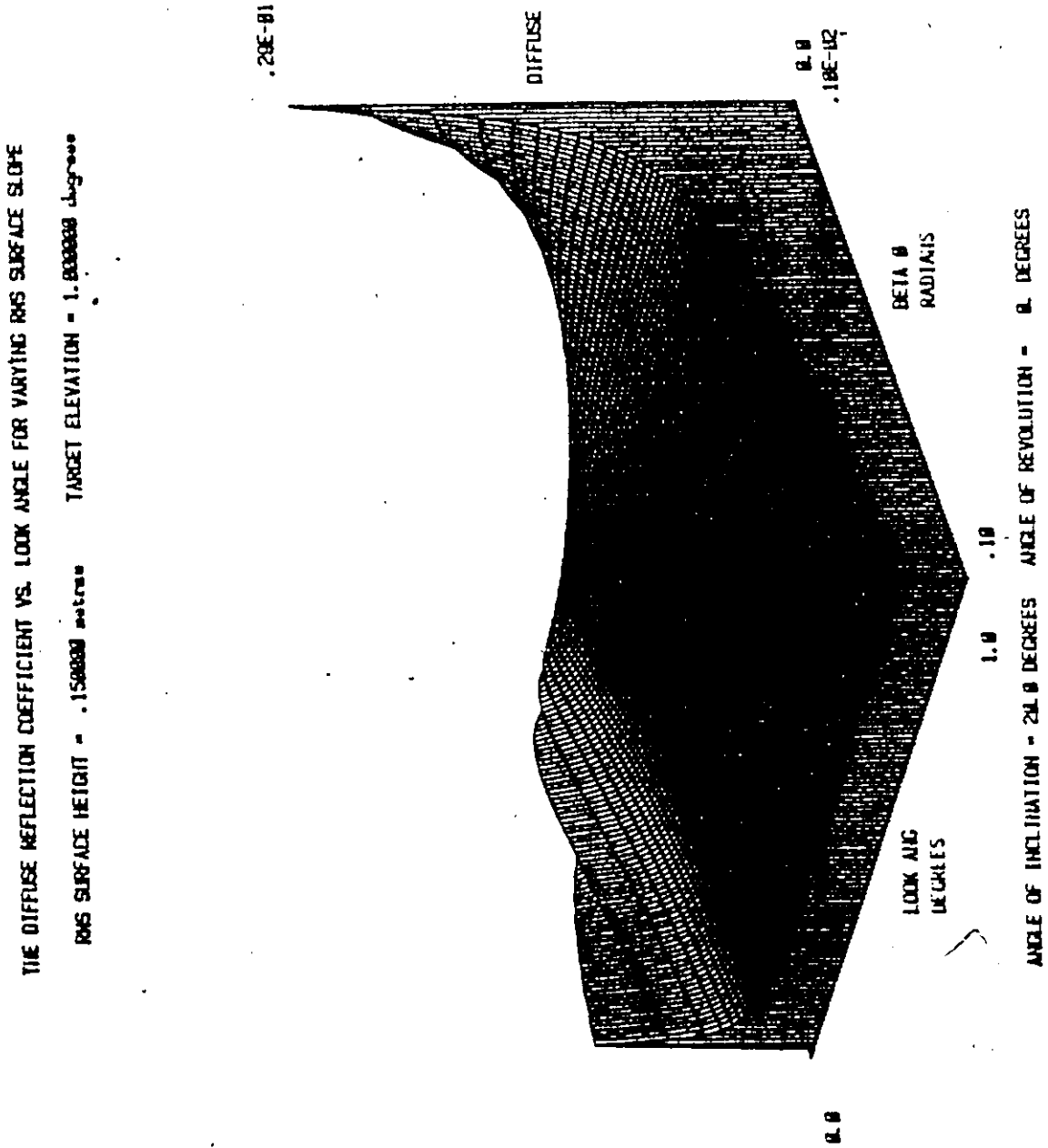


Figure 5.1.2.0 The diffuse reflection coefficient versus look angle for varying RMS surface slope for a target elevation of  $\theta_t = 1.0$  de rees, and a surface height deviation of  $\sigma_h = .15$  metres.



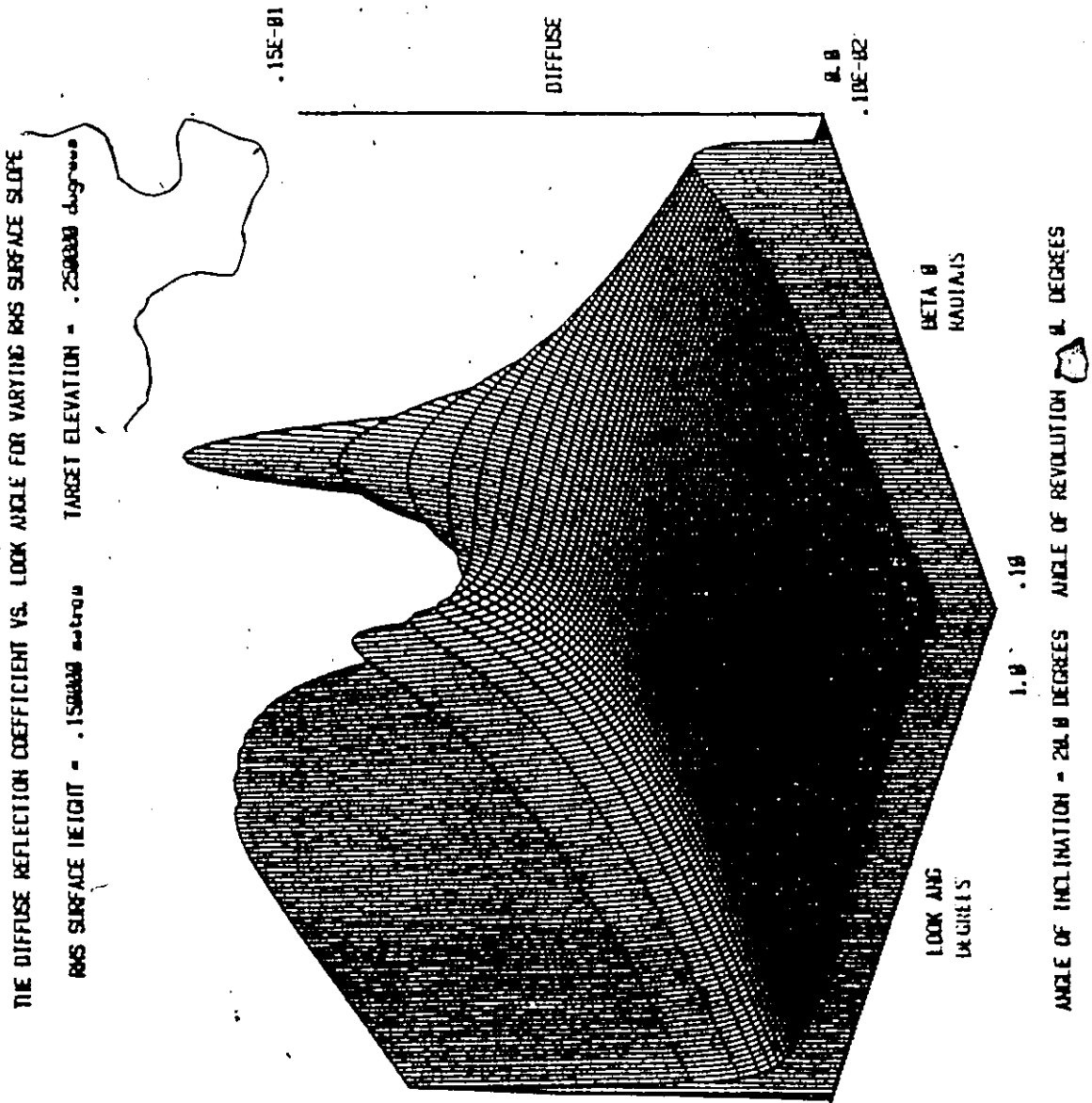


Figure 5.1.2.E The diffuse reflection coefficient versus look angle for varying RMS surface slope for a target elevation of  $\theta_t = .25$  degrees, and a surface height deviation of  $\sigma_h = .15$  metres.

### 5.1.3 RMS Surface Height Deviation

The five figures (5.1.3 A - E) of this section will, as in section 5.1.2, be arranged in two groups of three. The first of these groups (Fig. 5.1.3 A - C) display the change in the diffuse reflection coefficient versus look angle with surface height deviation  $\sigma_h$ , and is shown for three different values of RMS surface slope  $\beta_o$ . These figures were chosen specifically to enhance the dominant figures of section 5.1.2. Figure 5.1.3 A shows the change in the peak of section 5.1.2 ( $\beta_o = .001$ ) for varying  $\sigma_h$  while figures 5.1.3 C ( $\beta_o = .1$ ) shows the fringe. Figure 5.1.3 B illustrates a transition stage at  $\beta_o = .01$  radians. Notice that the maximum peak of figure 5.1.3 C is  $\rho_d = .044$  at  $\sigma_h = .6$  metres  $\beta_o = .001$  radians is the same peak found in figure 5.1.2 A at  $\beta_o = .001$  and for  $\sigma_h = .6$  naturally giving the same value of  $\rho_d$ . It is interesting to note the dramatic change in the amplitude of this peak as  $\sigma_h$  changes. It should be pointed out that the slope of  $\rho_d$  versus  $\sigma_h$  approaches zero for large  $\sigma_h$ .

By close inspection of figure 5.1.3 A we can see that the effects of varying  $\sigma_h$  are more dominant at the very small look angles. Notice that the slope of the cross section at a look angle of 1.0 degrees is far less than that at .03 degrees. The combined effects of increased amplitude for decreasing look angle and increase  $\sigma_h$  are perhaps most obvious in figure 5.1.3 B, note the significant difference in the shape of  $\rho_d$  versus look angle for  $\sigma_h = .038$  and  $\sigma_h = .6$  metres. The above mentioned feature can be explained with reference to equation 2.15 and 2.7. Notice the  $\rho_s^2$  term of equation 2.15 found in equation 2.7

consists of two factors;  $\sigma_h$  and the SINE of the look angle. This means that the roughness factor will increase for increasing  $\sigma_h$  or decreasing look angle. We can also see from figure 5.1.3 C that there is no change in the extent of the glistening surface as a result of varying  $\sigma_h$ .

By consideration of figure 5.1.3 D, B, and E we can see the effects that different target elevations have on the coefficient's distribution. Notice the increasing of  $\rho_d$  for decreasing elevation. Also notice the lack of fringing in figure 5.1.3 D (elevation angle of 1.0 degree) as compared to 5.1.3 E (elevation angle of .25 degrees) and the transition stage found in figure 5.1.3 B for target elevation angle of .5 degrees.

THE DIFFUSE REFLECTION COEFFICIENT VS. LOOK ANGLE FOR VARYING RMS SURFACE HEIGHT

RMS SURFACE SLOPE = .163033 radians TARGET ELEVATION = .500000 degrees

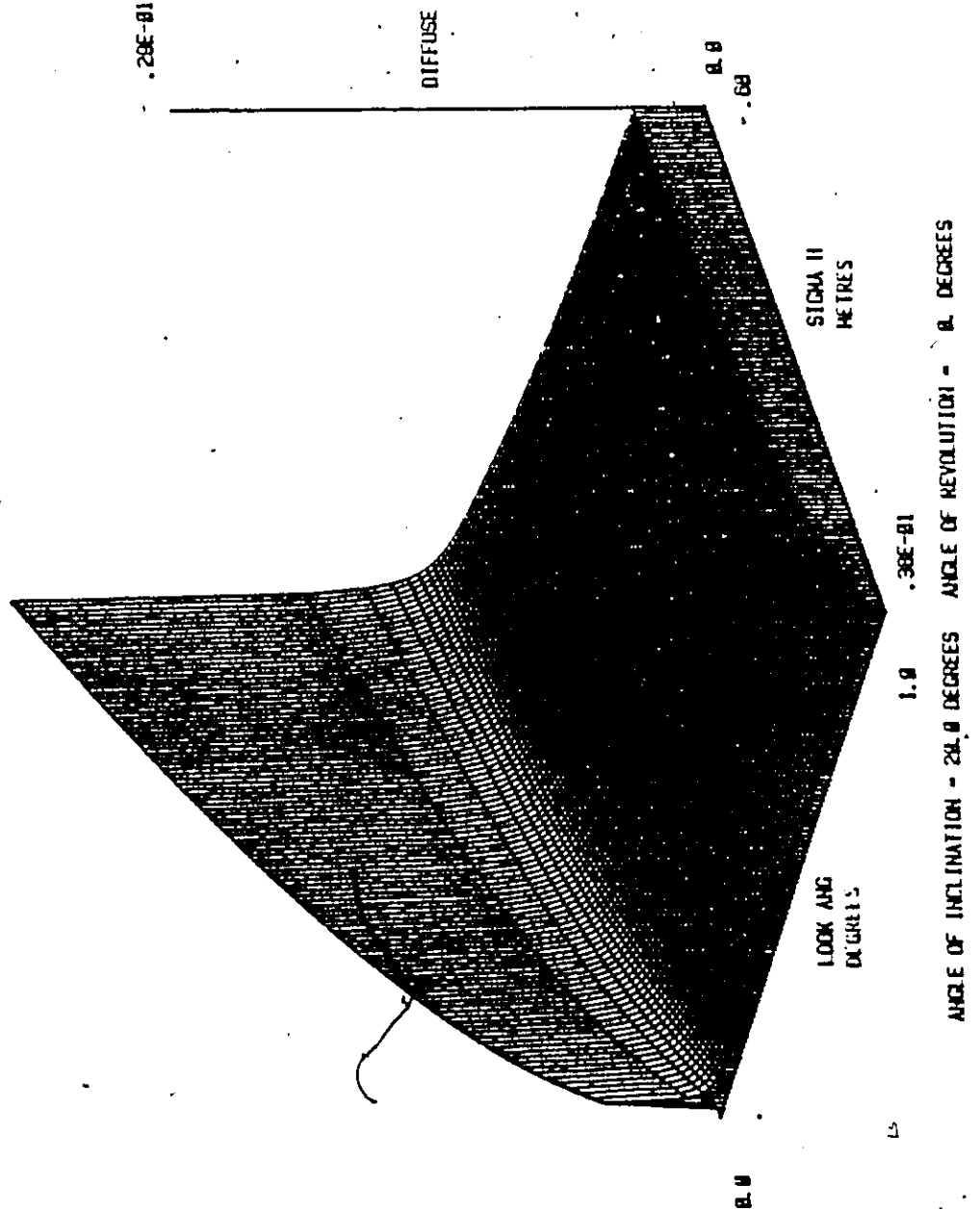


Figure 5.1.3.A

The diffuse reflection coefficient versus look angle for varying RMS surface height deviation, with a RMS surface slope of  $\theta_0 = .1$  radians, and a target elevation of  $\theta_t = .5$  degrees.

THE DIFFUSE REFLECTION COEFFICIENT VS. LOOK ANGLE FOR VARYING RMS SURFACE HEIGHT

RMS SURFACE SLOPE = .010000 radians TARGET ELEVATION = .500000 degrees

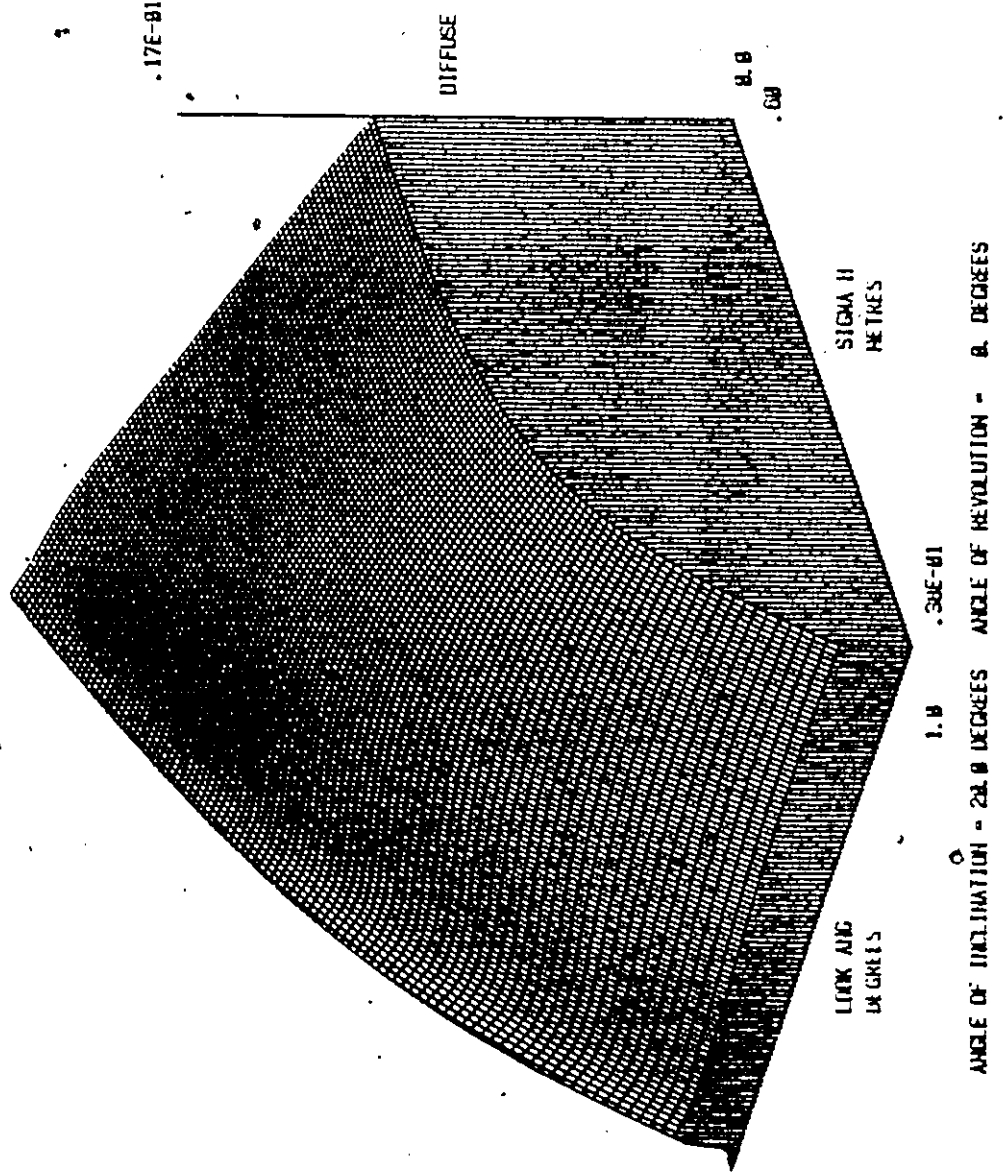


Figure 5.1.3.3 The diffuse reflection coefficient versus look angle for varying RMS surface height deviation, with a RMS surface slope of  $\beta_0 = .01$  radians, and a target elevation of  $\theta_t = .5$  degrees.

THE DIFFUSE REFLECTION COEFFICIENT VS. LOOK ANGLE FOR VARYING RMS SURFACE HEIGHT

RMS SURFACE SLOPE = .001000 radians TARGET ELEVATION = .500000 degrees

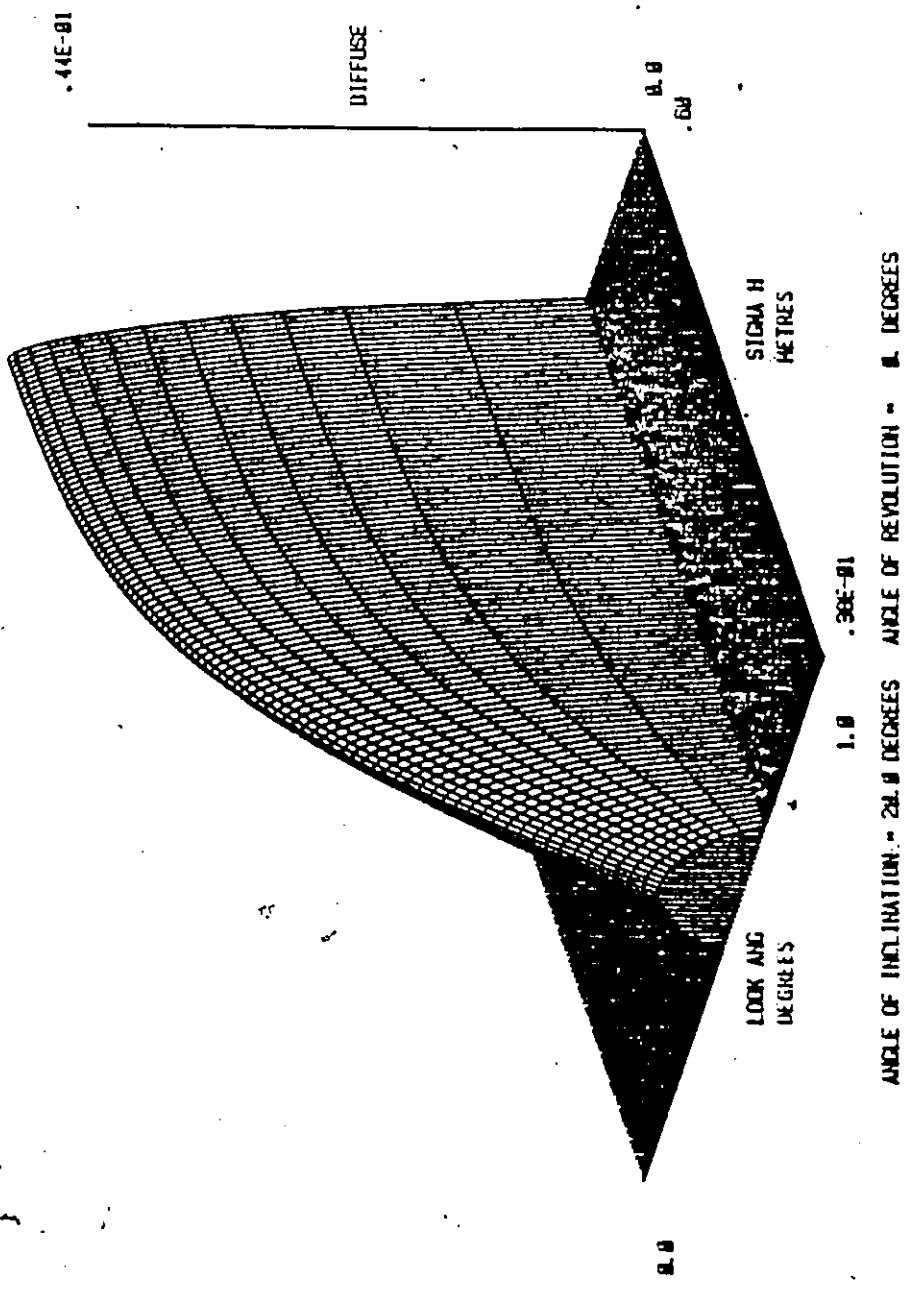


Figure 5.1.3.C The diffuse reflection coefficient versus look angle for varying RMS surface height deviation, with a RMS surface slope of  $\theta_0 = .001$  radians, and a target elevation of  $\theta_t = .5$  degrees.

THE DIFFUSE REFLECTION COEFFICIENT VS. LOOK ANGLE FOR VARYING RMS SURFACE HEIGHT

RMS SURFACE SLOPE = .010000 radians TARGET ELEVATION = 1.000000 degrees

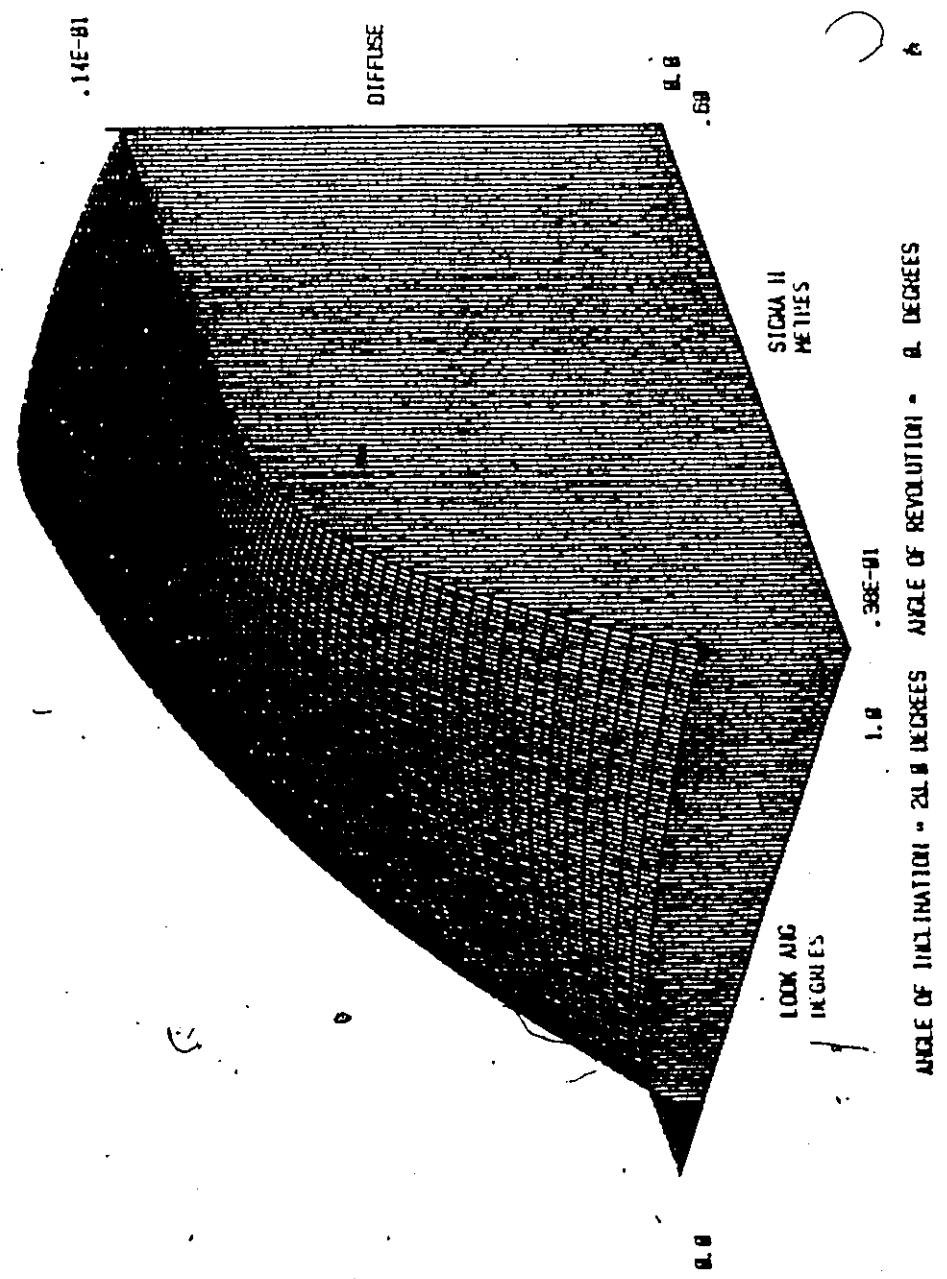


Figure 5.1.3.0 The diffuse reflection coefficient versus look angle for varying RMS surface height deviation with a RMS surface slope of  $\theta_0 = .01$  radians, and a target elevation of  $\theta_t = 1.0$  degrees.

THE DIFFUSE REFLECTION COEFFICIENT VS. LOOK ANGLE FOR VARYING RMS SURFACE HEIGHT

RMS SURFACE SLOPE = .010000 radians TARGET ELEVATION = .250000 degrees

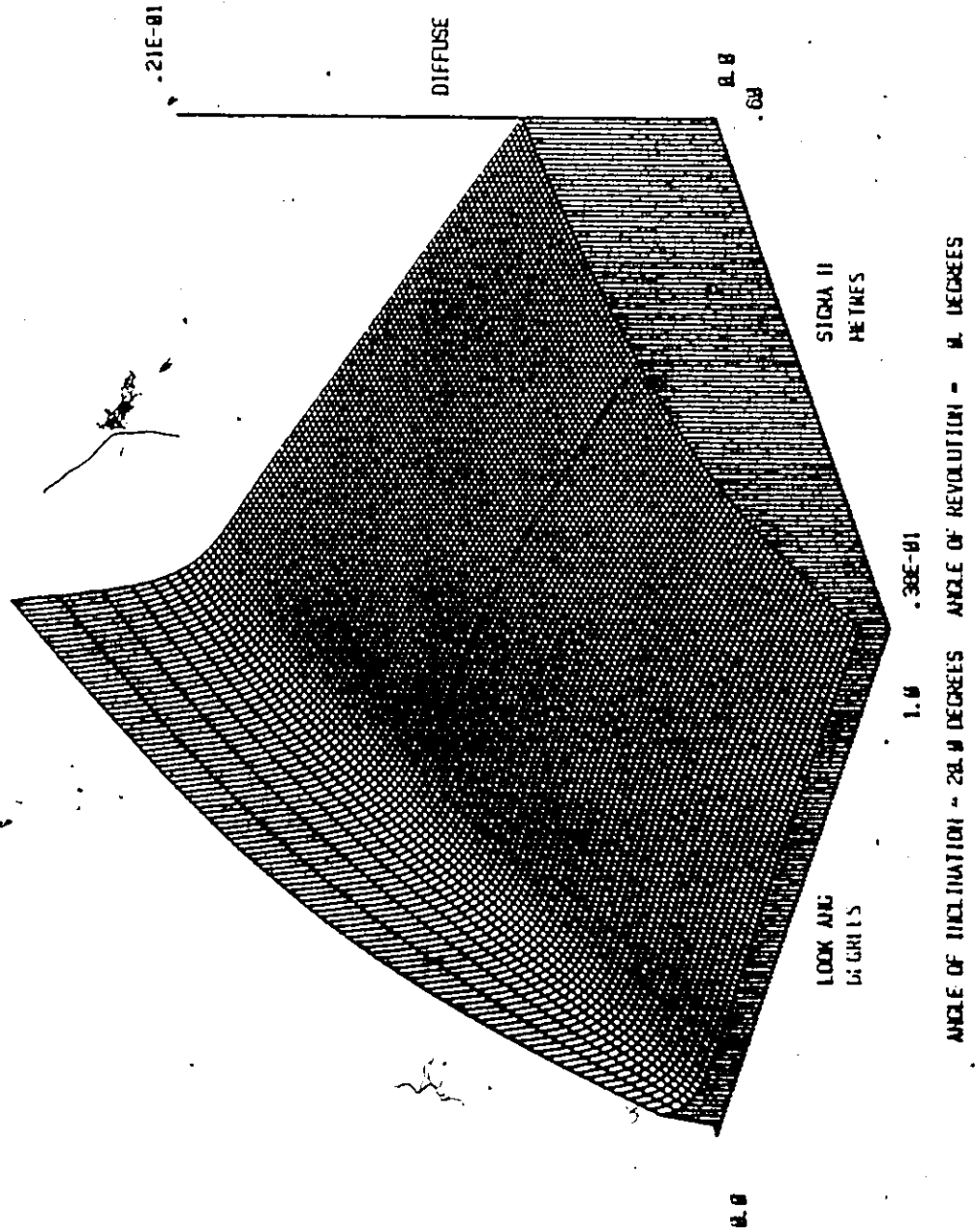


Figure 5.1.3.E The diffuse reflection coefficient versus look angle for varying RMS surface height deviation with a RMS surface slope of  $\theta_0 = .01$  radians, and a target elevation of  $\theta_c = .25$  degrees.



#### 5.1.4 Target Elevation

The figure of this section (Fig. 5.1.4 A - E) are also arranged in two groups of three plots with a total five. The first group figures 5.1.4 A, B, C have been chosen such that the  $\beta_0$  of .01 will give the transition between peaks and fringes for an elevation angle of .5 degrees.

It is now quite obvious that the amount of fringing (or the amount power reflected from small angles) is dependent on the elevation angle of the target. We can also see the effect that  $\sigma_h$  has on this distribution. When  $\sigma_h$  is larger (figure 5.1.4 A) the magnitude of the diffuse reflection coefficient is larger particularly at small look angles. On the other hand when  $\sigma_h$  is small (figure 5.1.4 C) the overall reflection coefficient is smaller and the emphasis is on the peaks rather than the fringes. We saw in Figure 5.1.3 B the effect  $\sigma_h$  had on  $\rho_d$  versus look angle and now it is possible to see how the elevation versus look angle plots have been deformed for the three value of  $\sigma_h$  (.0375, .15, .6)

As in section 5.1.3 figures 5.1.4 D, B, E were chosen to enhance the three dominant features associated with varying  $\beta_0$ . The surface height deviation  $\sigma_h$  has been maintained at a constant value of .15 meters for the three  $\beta_0$  values of .1, .01, .001 radians figure 5.1.4 D-E respectively. These plots represent the fringes, transition, and peak stages discussed in sections 5.1.2 and 5.1.3 for a target elevation angle of .5 degrees. We can see, as pointed out earlier, that the distribution of figure 5.1.4 B toggles between the fringe and peak

stages, reaching the transition stage at elevation angle of .5 degrees.

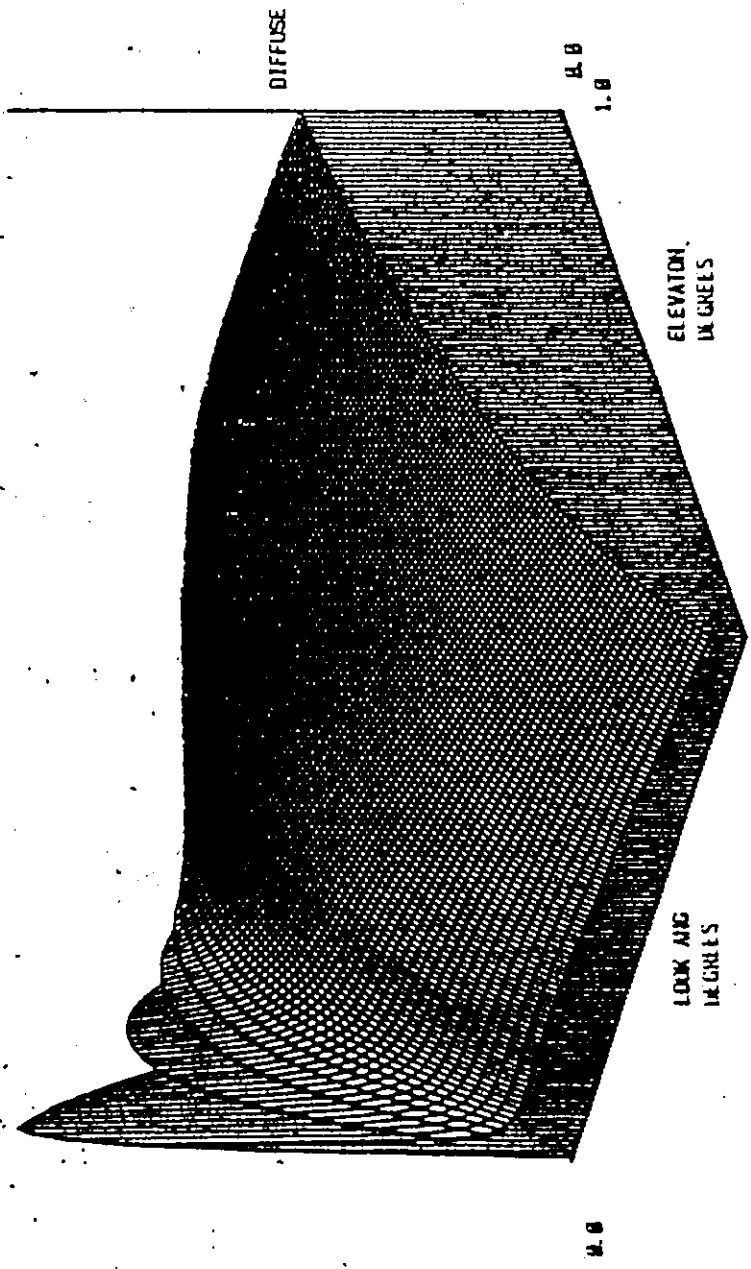
It is very clear in figure 5.1.4 E that the peak follows the target elevation angle. It can be seen however that for very small elevation angles even this distribution begins to show signs of fringing.

In figure 5.1.4 D we can see that the fringe distribution associated with a large  $\beta_0$  become very large. In fact the fringe attains such a large value of  $\rho_d$  between points (large slope) for small look and elevation angles that it is difficult to evaluate with a look angle resolution of only .01 degrees.

THE DIFFUSE REFLECTION COEFFICIENT VS. LOOK ANGLE FOR VARYING TARGET ELEVATION

RMS SURFACE SLOPE = .010000 radians RMS SURFACE HEIGHT = .000000 meters

.30E-01



ANGLE OF INCLINATION = 20.0 DEGREES ANGLE OF REVOLUTION = 0. DEGREES

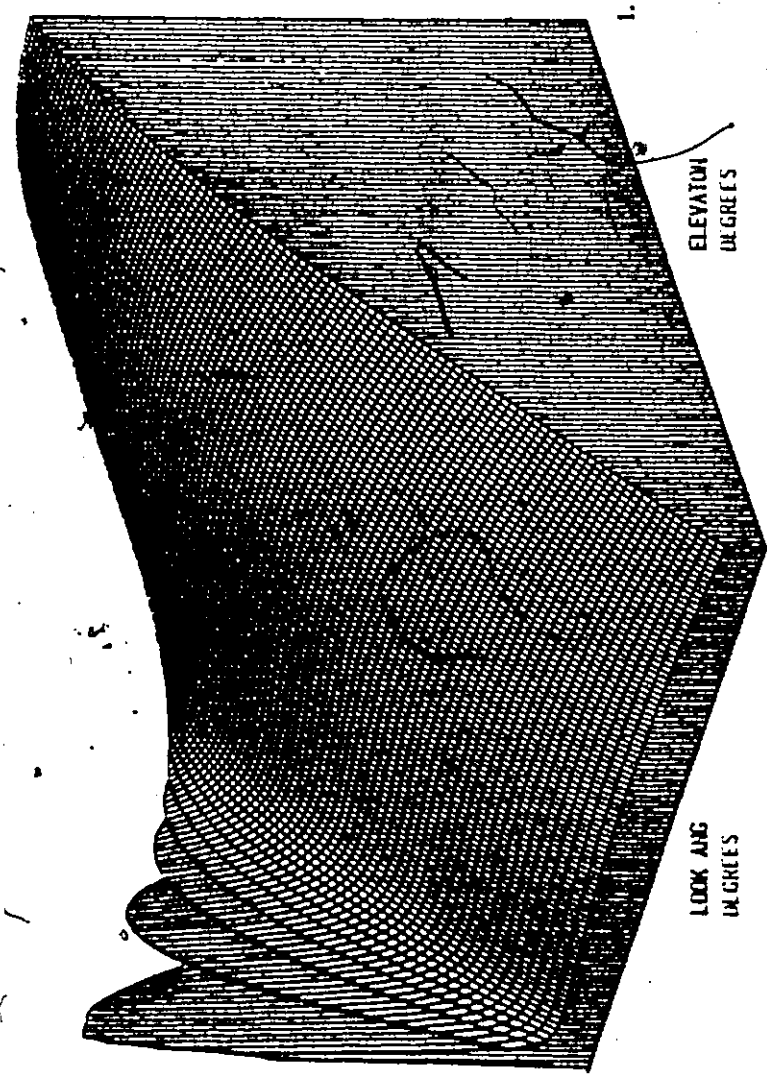
Figure 5.1.4.A The diffuse reflection coefficient versus look angle for varying target elevation with a RMS surface slope of  $\sigma_s = .01$  radians, and RMS surface height deviation of  $\sigma_h = .5$  metres.

THE DIFFUSE REFLECTION COEFFICIENT VS. LOOK ANGLE FOR VARYING TARGET ELEVATION

RMS SURFACE SLOPE =  $0.01$  radians RMS SURFACE HEIGHT =  $.15$  metres

.12E-01

DIFFUSE



ELEVATION IN DEGREES

LOOK ANGLE IN DEGREES

1.0

ANGLE OF INCLINATION =  $20.0$  DEGREES ANGLE OF REVOLUTION =  $0$  DEGREES

Figure 5.1.4.8 The diffuse reflection coefficient versus look angle for varying target elevation with a RMS surface slope of  $0.01$  radians, and RMS surface height deviation of  $.15$  metres.

THE DIFFUSE REFLECTION COEFFICIENT VS. LOOK ANGLE FOR VARYING TARGET ELEVATION.  
 RMS SURFACE SLOPE = .018000 radians RMS SURFACE HEIGHT = .037500 meters

.39E-02

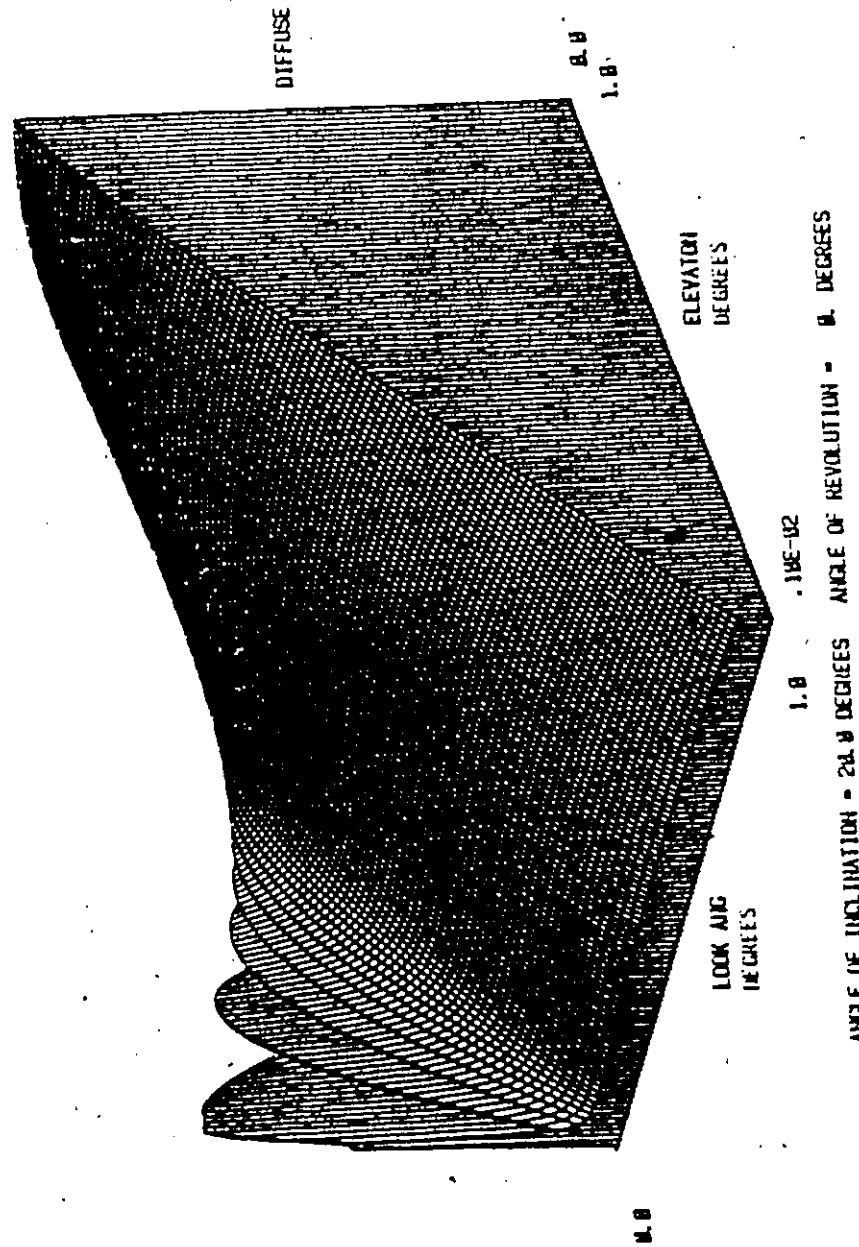


Figure 5.1.4.C The diffuse reflection coefficient versus look angle for varying target elevation with a RMS surface slope of  $\theta_s = .01$  radians, and RMS surface height deviation of  $\sigma_h = .0375$  metres.

THE DIFFUSE REFLECTION COEFFICIENT VS. LOOK ANGLE FOR VARYING TARGET ELEVATION

RMS SURFACE SLOPE =  $1.100000$  radians RMS SURFACE HEIGHT =  $.150000$  meters

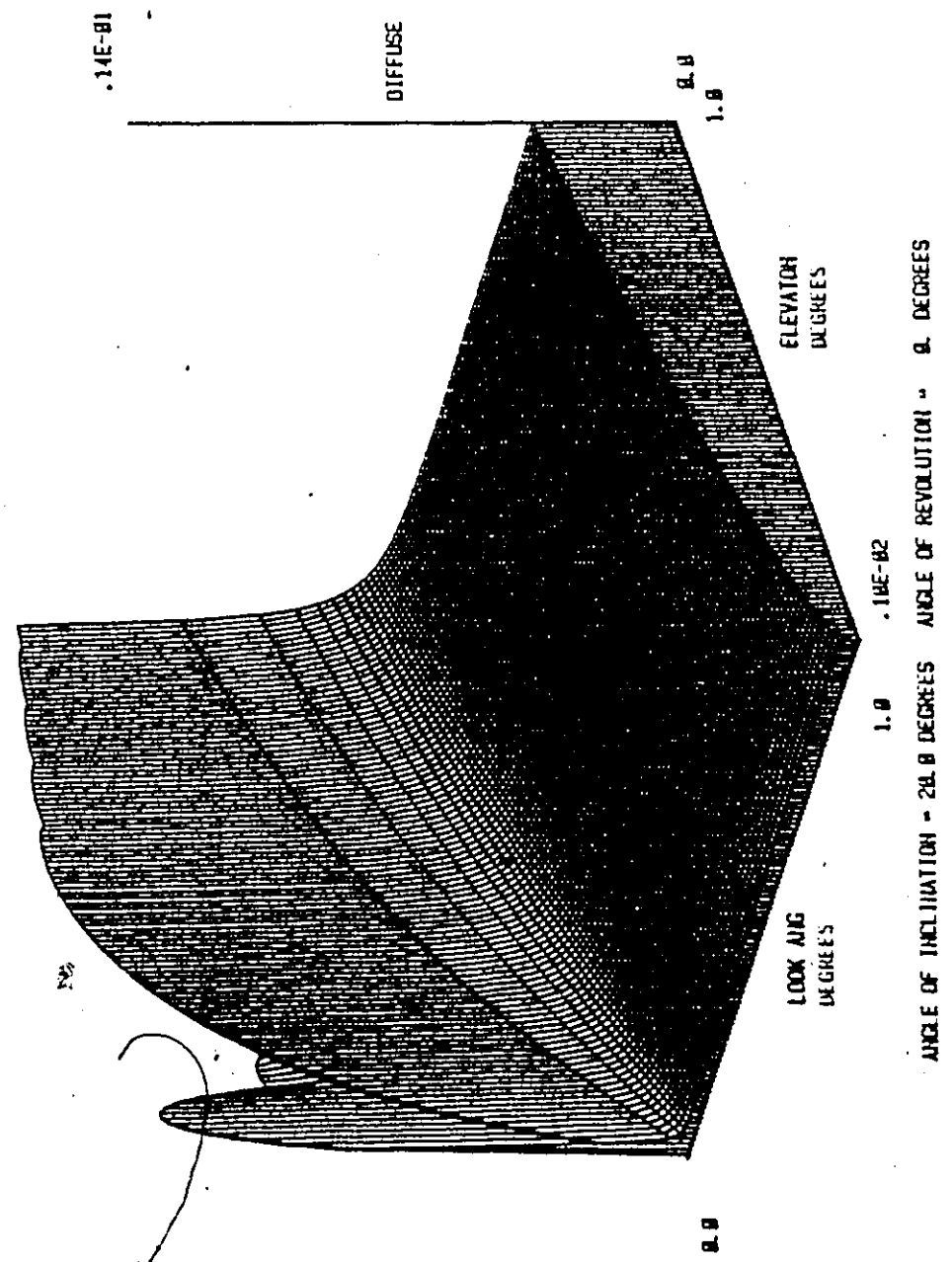


Figure 5.3.4.D The diffuse reflection coefficient versus look angle for varying target elevation with a RMS surface slope of  $\sigma_s = .1$  radians, and RMS surface height deviation of  $\sigma_h = .15$  metres.

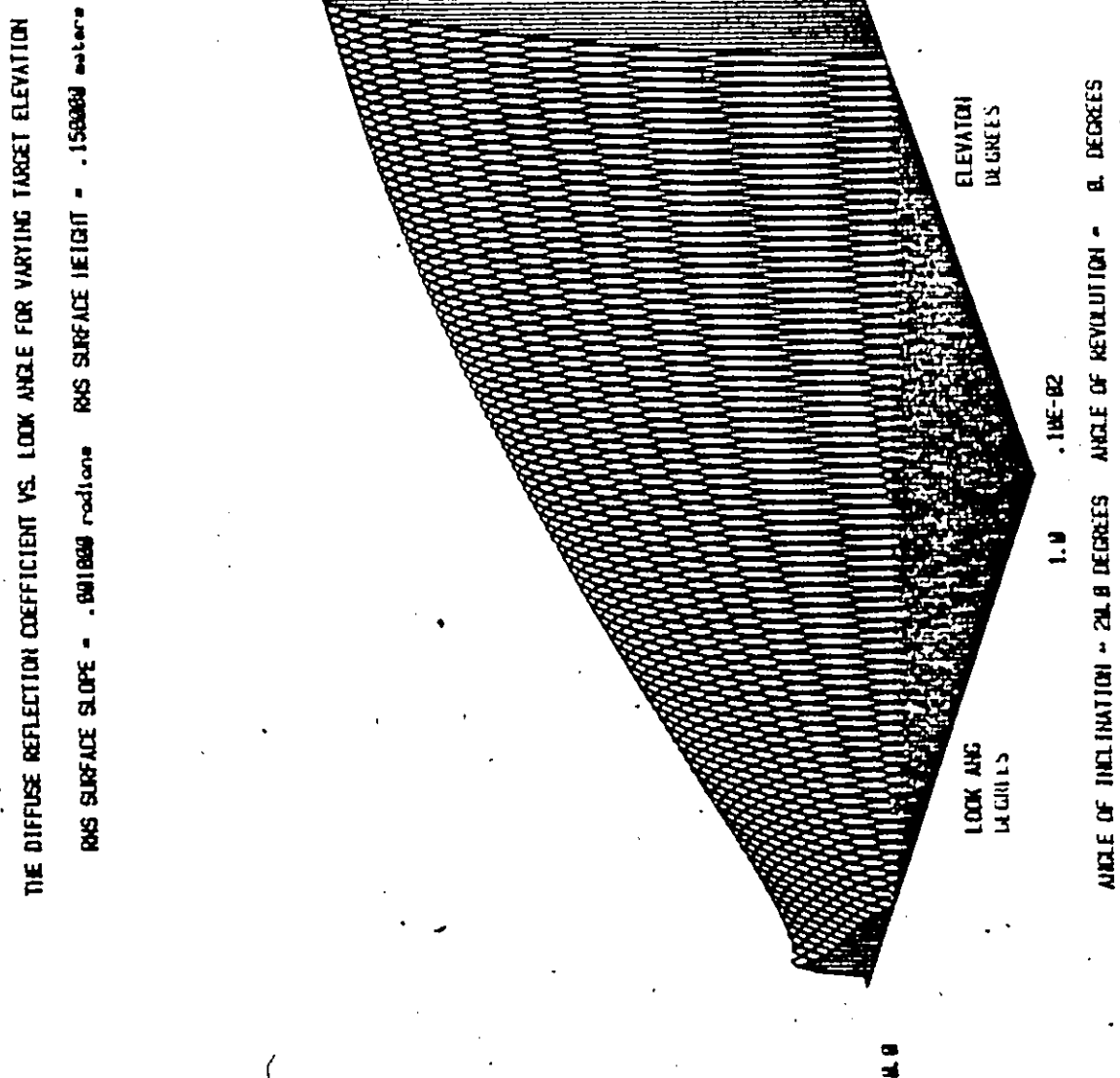


Figure 5.1.4.E The diffuse reflection coefficient versus look angle for varying target elevation with a RMS surface slope of  $\sigma_s = .001$  radians, and RMS surface height deviation of  $\sigma_h = .15$  metres.

### 5.1.5 Summary of Theoretical results

Perhaps the single most important factor contributing to the characteristics of the diffuse multipath reflection coefficient observed is that of the RMS surface slope  $\beta_0$ . There are drastic variations in the shape of  $\rho_d$  versus look angle over the range of  $\beta_0 = .001$  to  $.1$  radians. It can be seen that except for very small angle the reflection coefficient within an angular step of  $.01$  degrees decreases in amplitude for increasing  $\beta_0$ . This, however, is not to say that the amount of diffuse power is reduced, just that the amount of power originating from a particular section of the surface has decreased. The total diffuse power in fact has increased considerably with increasing  $\beta_0$  since this power can be distributed over extremely large angles ( $45$  degrees for a target elevation of  $.5$  degrees and a  $\beta_0$  of  $.1$  radians) when  $\beta_0$  is large.

It has been observed that the RMS surface height deviation  $\sigma_h$  has no affect on the extent of the glistening surface, but that its effects are observed in both the look angle and  $\sigma_h$  coordinates. Remembering that  $\sigma_h$  is a product term with the SINE of the look angle in an equation defining the roughness factor, we can see that this variation will occur. From section 5.1.3 it may be observed that the effects of changing  $\sigma_h$  are most dominant in the range  $.038$  to  $.3$  ( $1.25 \lambda$  to  $10 \lambda$ ) after which time the effects seem to plateau.

Increasing the target elevation has a two fold effect on the diffuse reflection coefficient since not only does the magnitude of the coefficient increase, but the angular spread of the glistening surface



increases as well. This effect of spread in the glistening surface is however nowhere near as dominant as in the case of changing  $\beta_0$  (at least one order of magnitude less).

### 5.2.1 Experimental

In the development and subsequent analysis of diffuse multipath it was assumed that the receiver was omnidirectional with unit gain. In such a case the receiver would see that which was displayed in the figures of sections 5.1.2, 5.1.3 and 5.1.4. It was however, desired to observe the effects a real antenna would have on these distributions (i.e. what features would be observed by a given antenna). With the use of program "DVS72" (Appendix B) data was obtained from the eight element phased array (described in Appendix A) in steps of .1 degrees over the range 0.0 - 5.0 degrees. This data was then stored in a file (# DATA) on the CRL's HP 1000 computer. Program "AJUST" then retrieved the data and made the necessary amplitude and phase adjustments (see Appendix B) to make the successive angular samples combinable. This adjusted data was then dumped into file "#AJUST".

The data describing the diffuse multipath distribution had been generated by the use of program "DFGEN" and was stored in file "DFGEN". Program "SHAPE" read data from both "AJUST" and "#DFGEN" combining them as described in appendix B to give the resulting or effective diffuse reflection coefficients.

### 5.2.2 Case 1

Case I is displayed first since it best describes the effects of antenna patterns on the observed characteristics of diffuse multipath. The characteristics found in the following two cases are far easier explained with reference to Case I, and have been so arranged for that reason.

In this example our target is situated at an elevation angle of .25 degrees with a range of 10 km. The receiving array is found 5 metres above a moderately rough surface ( $\beta_0 = .1$  radians  $\sigma_h = .15$  metres). Figure 5.2.2 A illustrates the glistening surfaces from which power is reflected towards the receiver. The extent of the glistening surface in the y axis is shown in metres over the look angle extent of 10.1 degrees. The actual glistening surface extends to 11.9 degrees but has been truncated for display purposes. It should be noted that the glistening surface is symmetric about  $y = 0$  with only half the surface shown. Note that the extent in y increases very rapidly for very small angles while its distribution for larger angles decreases monotonically. Figure 5.2.2 B shows the distribution of reflection coefficient over this glistening surface.

It is very important to note the increased overall and decreased relative amplitude of the horizon spike and the monotonic section for the plots of this section compared to their corresponding crosssections of sections 5.1.1 - 5.1.5. This observation is easily explained; the plots of this section represent diffuse reflection coefficients corresponding to patches of surface contained within an angular step of

.1 degrees while the plots of the previous section were generate at angular steps of .01 degrees. Since the steps size is greater in this section we observed an averaging of features.

Figure 5.2.2 C is the corresponding phase of the reflection coefficient of figure 5.2.2 B; as might be expected, there is little if any information extractable from the phase plots.

Figures 5.2.2 D and 5.2.2 E are blow ups of figures 5.2.2 B and 5.2.2 C. This was done so that these theoretical plots might be compared directly with their experimental partners: figure 5.2.2 F and 5.2.2 G over the 5.0 degree range experimental data. In figure 5.2.2 F we have shown the model distribution of figure 5.2.2 D with the element pattern of one form of our eight element array applied. The two distributions (D and F) are quite similar, this is, of course, to be expected since the gain of one element should be very near unity over the 5.0 degree range of our data. It may, however, be noted that this curve lacks the smooth trend of the theoretical curve of figure 5.2.2 D. It might also be noted that the phase plots illustrated are the change in phase observed at element eight for varied depression angle.

In figures 5.2.2 H and 5.2.2 I, we see the result of combining the eight array elements. In this and all other cases examined the main beam of this pattern has been centred on the target (in this case at  $-.25$  degrees), and the array elements have been weighted equally. We can see that we obtain an effective null at 3 degrees or 3.25 degrees from the centre of the main beam. Notice that there is a fair amount of gain increasing the effective  $\rho_d$  in the main lobe. It is apparent that

5.0 degrees is quite sufficient to observe the effects of antenna gain on the distribution of diffuse power, since the amount of power in the sidelobe is small comparably speaking.

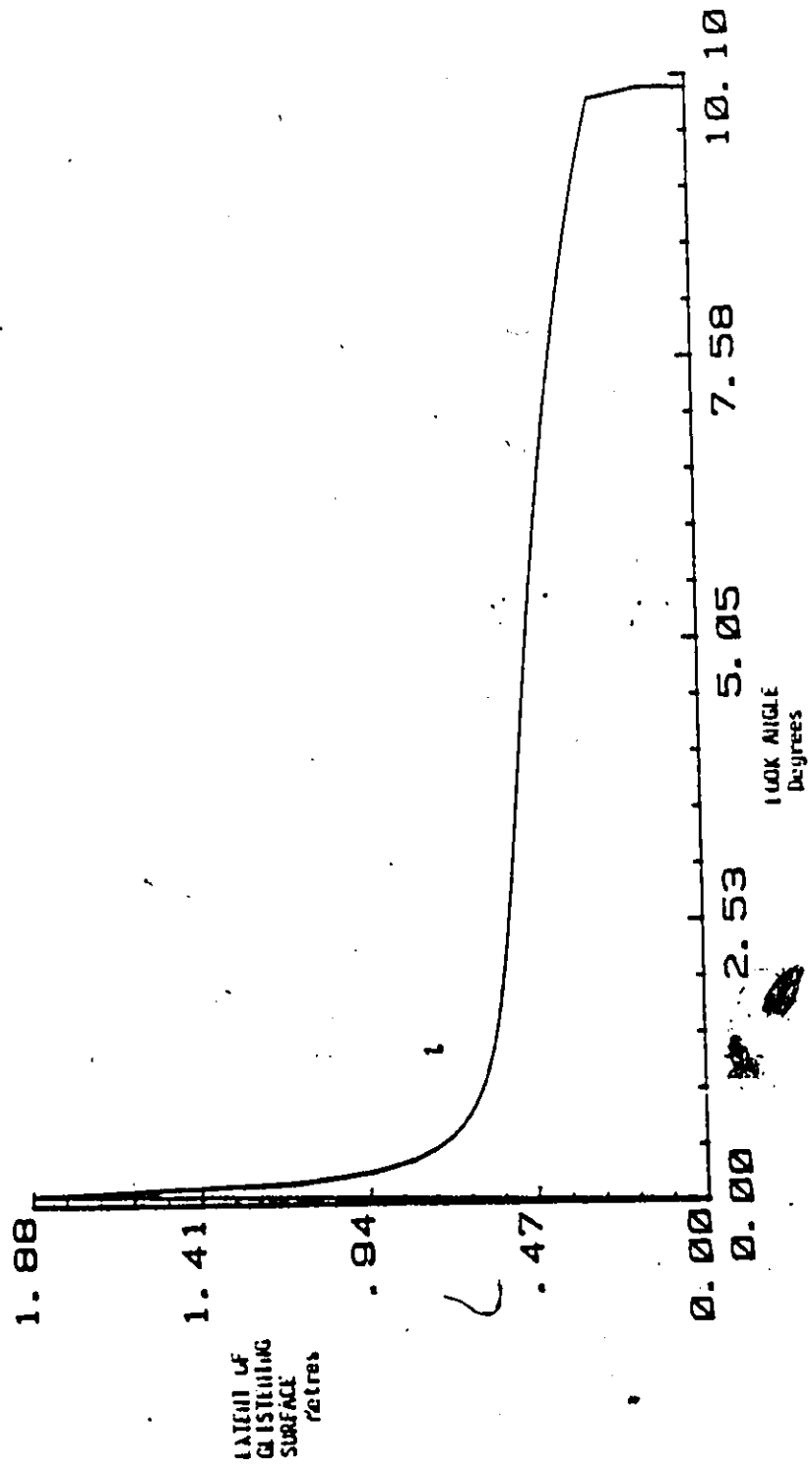


Figure 5.2.2.A Extent of glistening surface  
 RMS surface slope  $\theta_3 = .1$  radians, RMS surface height deviation  
 $\sigma_{sn} = .15$  metres, target elevation  $\theta_2 = .25$  degrees.

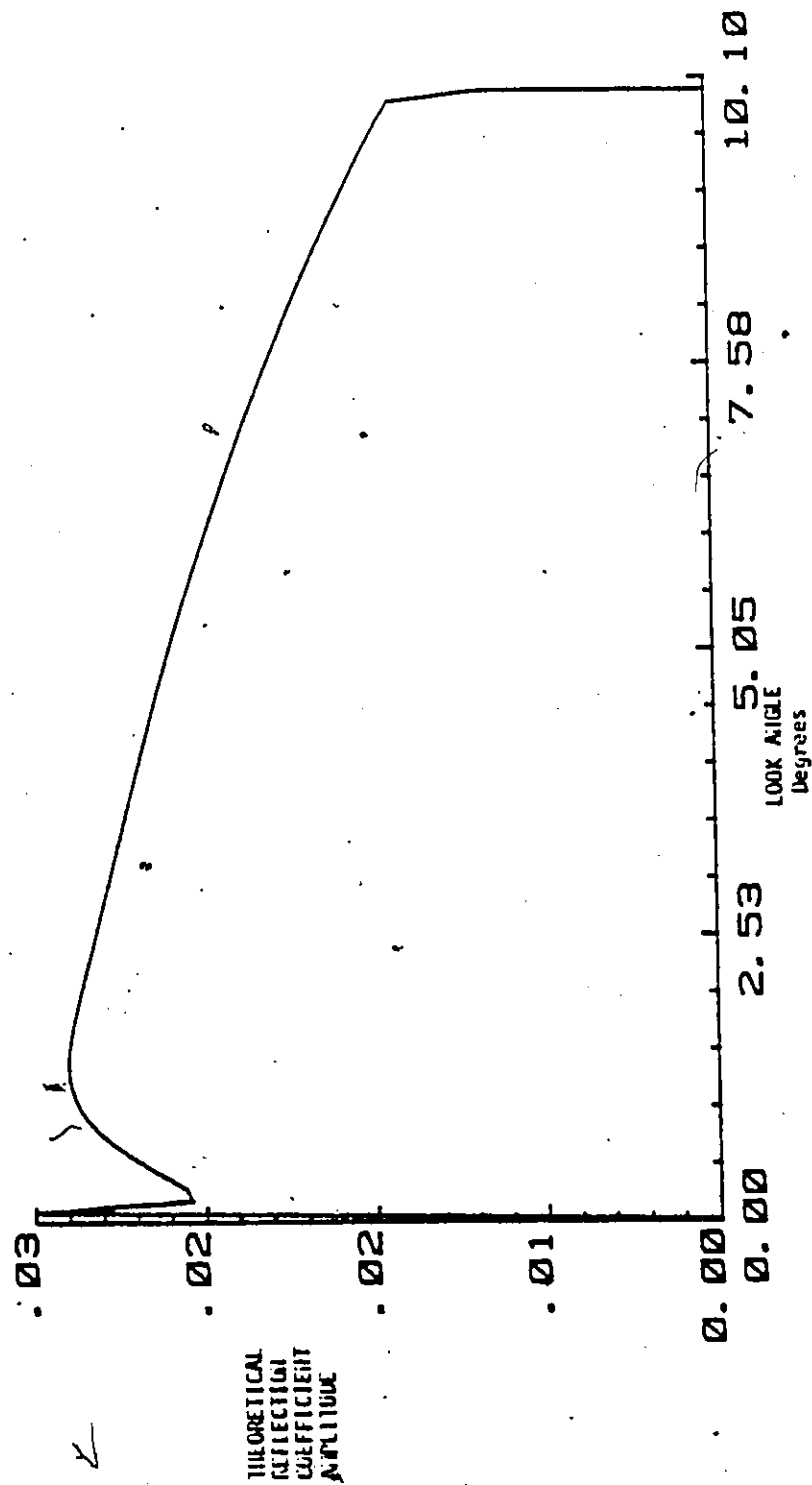


Figure 5.2.2.3 Magnitude of the diffusion reflection coefficient (theoretical)  
 RMS surface slope  $\theta_0 = .1$  radians, RMS surface height deviation  
 $\sigma_n = .15$  metres, target elevation  $\theta_s = .25$  degrees

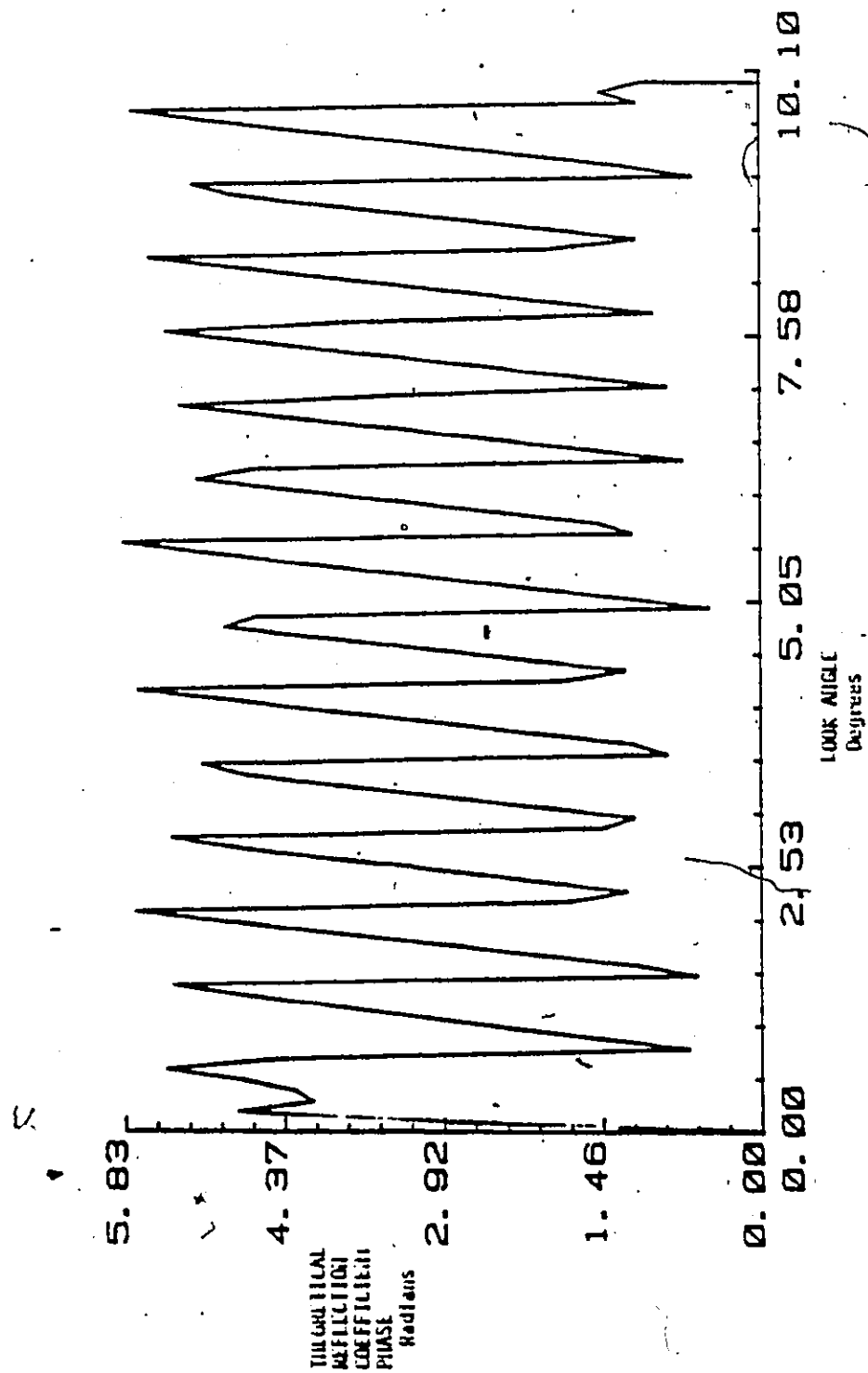


Figure 5.2.2.C Phase of the diffuse reflection coefficient (theoretical)  
 RMS surface slope  $\sigma_0 = .1$  radians, RMS surface height deviation  
 $\sigma_h = .15$  metres, target elevation  $\theta_t = .25$  degrees.

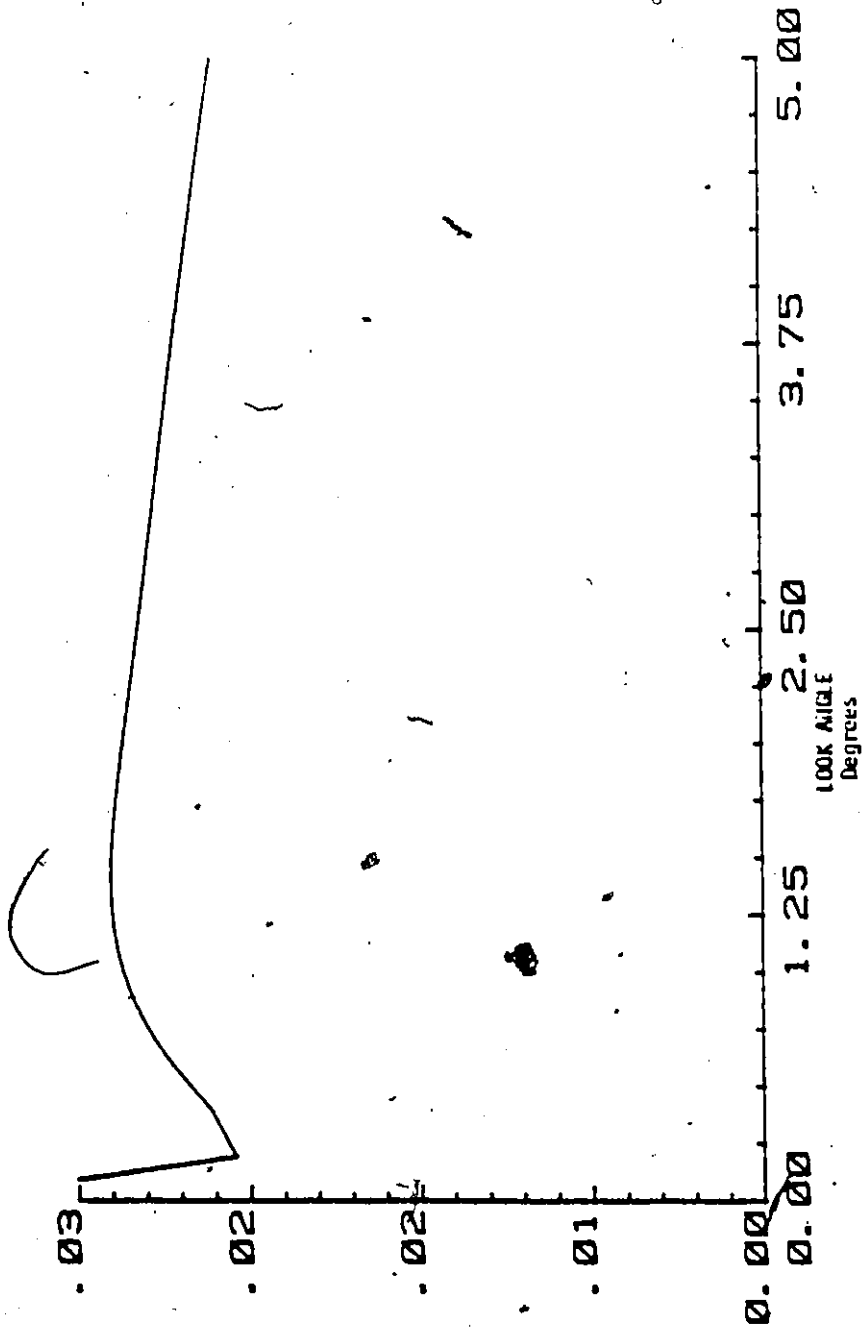


Figure 5.2.2.0 5.0 degree blow-up of the theoretical diffuse reflection coefficient's magnitude RMS surface slope  $\theta_n = .1$  radians, RMS surface height deviation  $\sigma_n = 1.5$  metres, target elevation  $\theta_e = .25$  degrees.



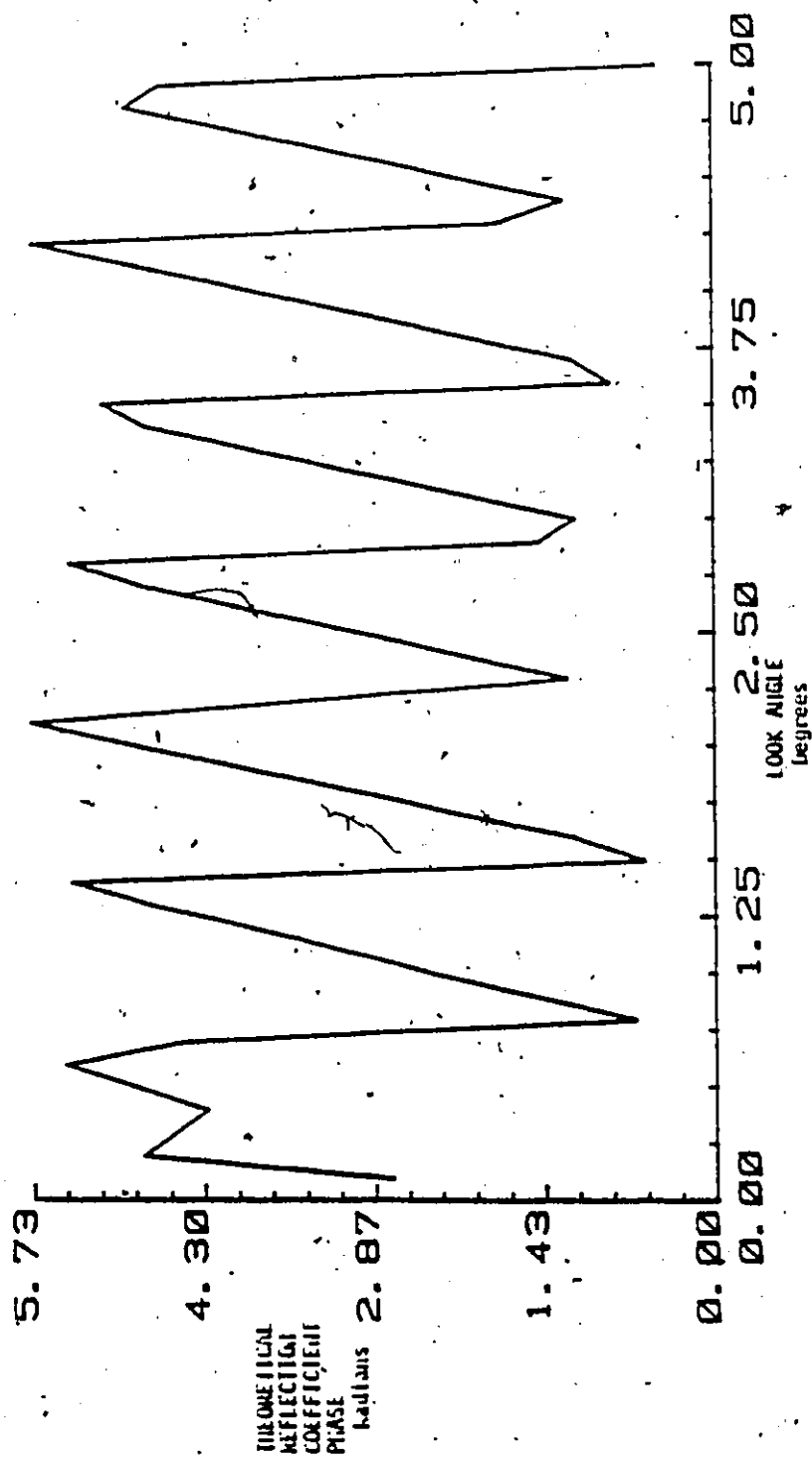


Figure 5.2.2.E 5.0 degree blow-up of the theoretical phase of the diffuse reflection coefficient: RMS surface slope  $\sigma_s = .1$  radians, RMS surface height deviation  $\sigma_h = .15$  metres, target elevation  $\theta_t = .25$  degrees.

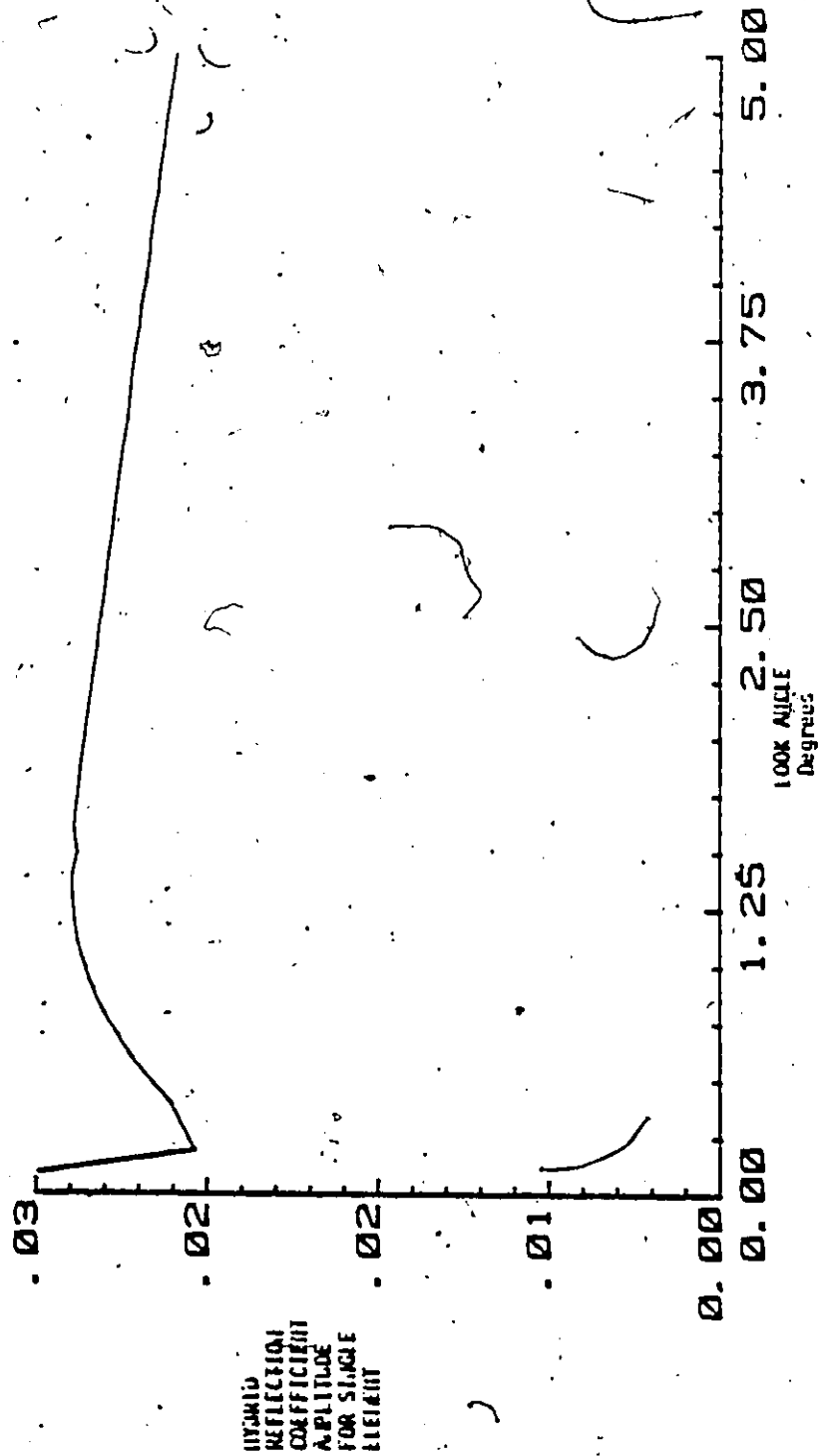


Figure 5.2.2.F : Magnitude of the reflection coefficient with experimental element pattern applied RMS surface slope  $\sigma_s = .1$  radians, RMS surface height deviation  $\sigma_h = .25$  metres, target elevation  $\theta_c = .25$  degrees.

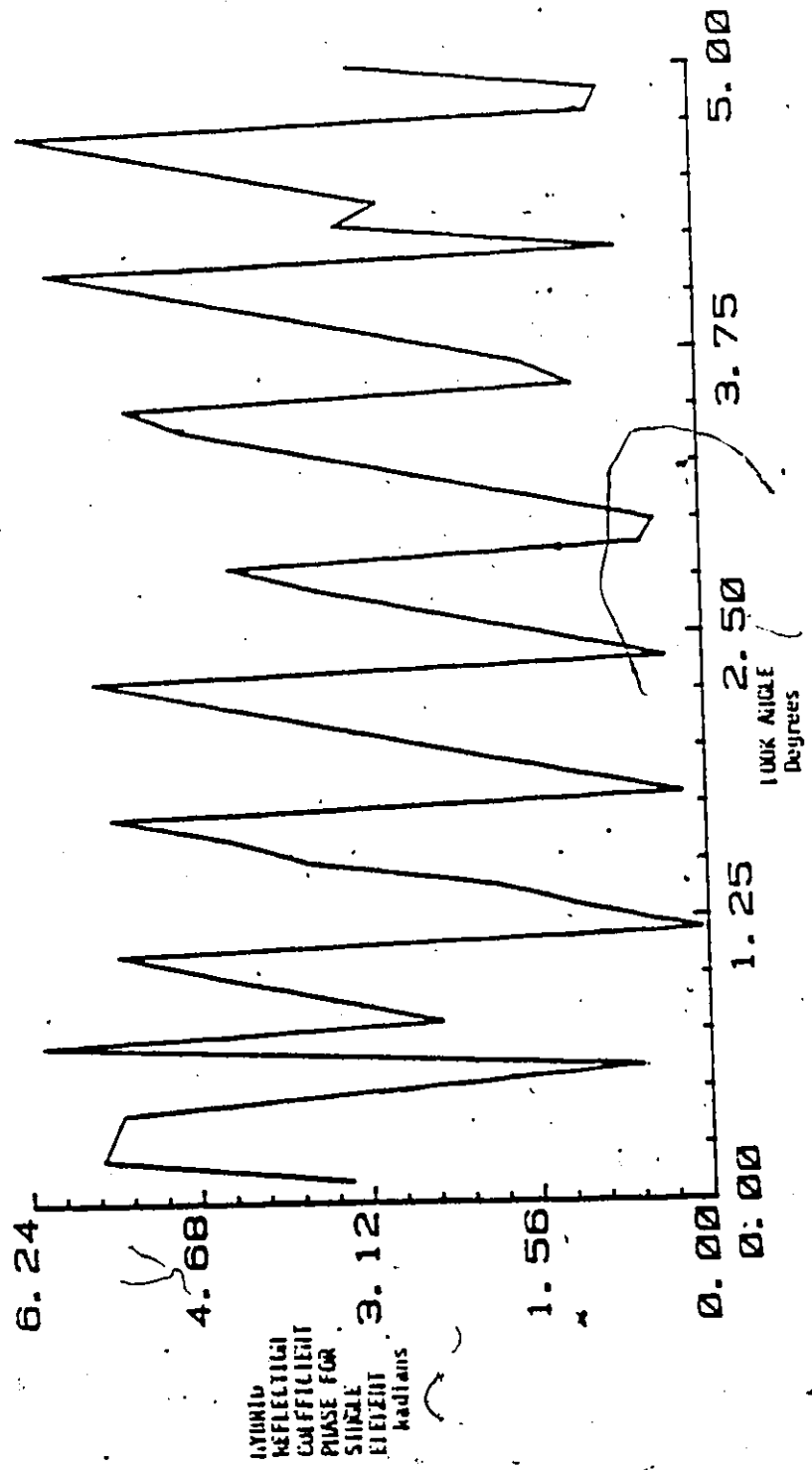


Figure 5.2.2.G Phase of the reflection coefficient with experimental element phase applied RMS surface slope  $\beta = .1$  radians, RMS surface height deviation  $\sigma_h = .15$  metres, target elevation  $\theta_t = .25$  degrees.

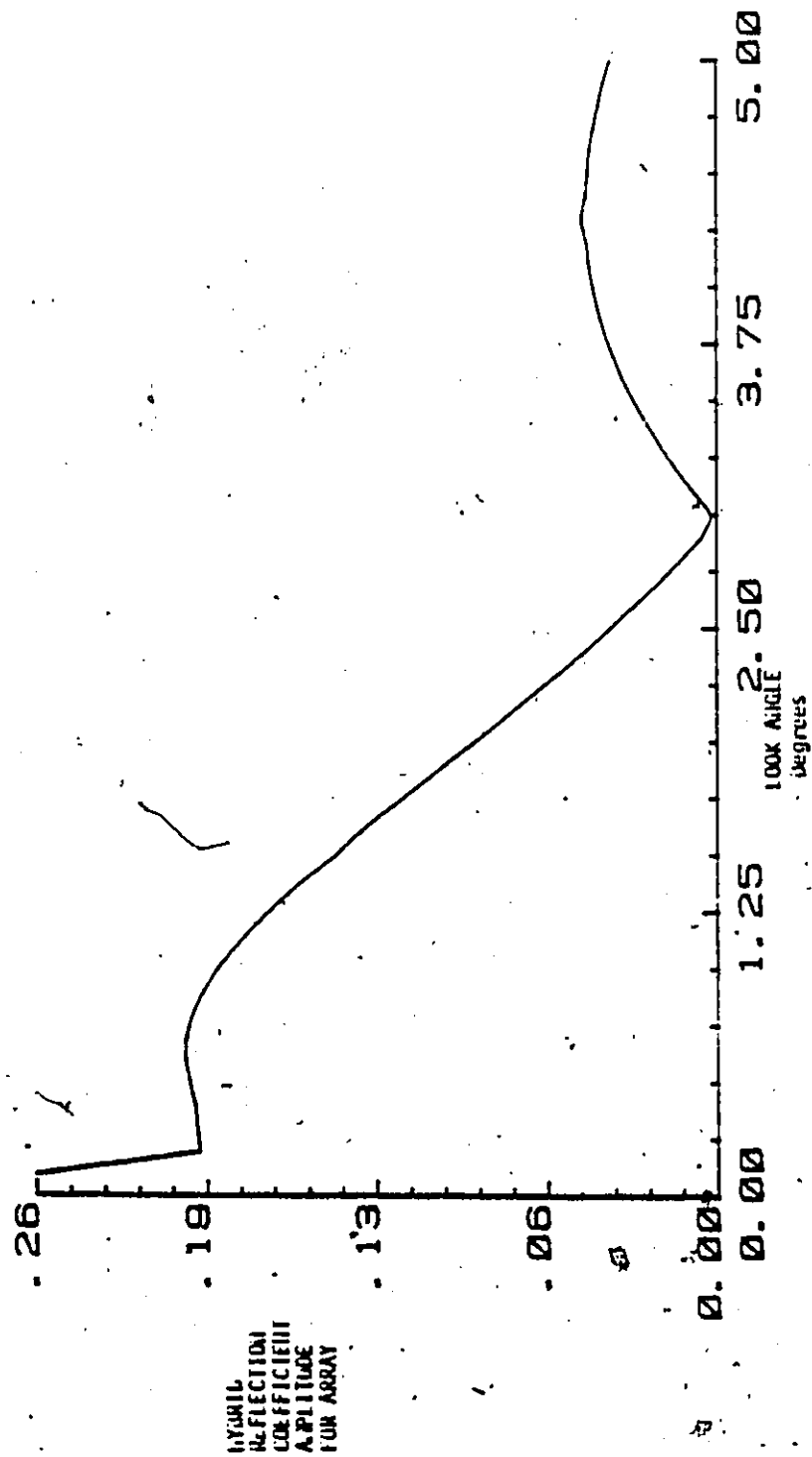


Figure 5.2.2.H Magnitude of the reflection coefficient for the combined-array pattern RMS surface slope  $\theta_0 = .1$  radians, RMS surface height deviation  $\sigma_h = .15$  metres, target elevation  $\theta_t = .25$  degrees.

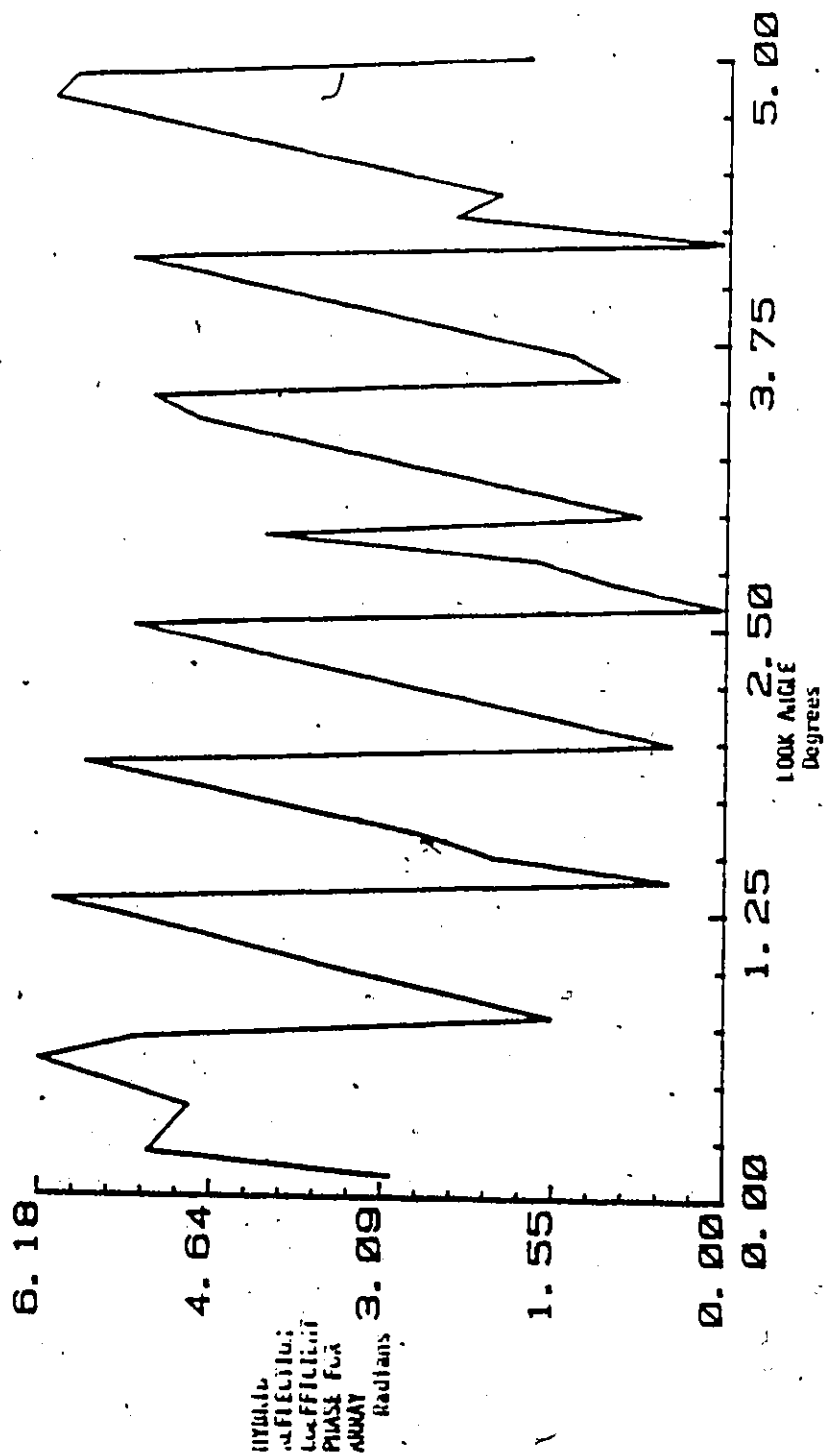


Figure 5.2.2.1 Phase of the reflection coefficient for the combined array pattern RMS surface slope  $\beta_0 = .1$  radians, RMS surface height deviation  $\sigma_h = .15$  metres, target elevation  $\phi_0 = .25$  degrees.

### 5.2.3 Case II

As in Case I, we are looking from a 5 m high radar at a target 10 kilometers away at an elevation of .25 degrees. In this case however the RMS slope of the surface ( $\beta_0$ ) is .01 radians with an RMS surface height deviation of .15 metres.

The figures of this section 5.2.3 A - I are arranged in the same format as in figures 5.2.2 A - I. Figure 5.2.3 A shows the extent of the glistening surface in  $y$  and look angle, it has been plotted on the same  $x$  scale as figure 5.2.2 A for comparison. Note that the glistening surface's extent in both elevation angle and in  $y$  has been greatly reduced by a reduction in  $\beta_0$ .

The reflection coefficient of figure 5.2.3 is shown on the scale of 0 - 10.1 degrees and again in figure 5.2.3 D over a 5. degree range. Upon application of the element pattern figure 5.2.3 F we again notice no apparent change in the distribution. It is, however, possible to detect a reduction in the amplitude of the reflection coefficient for increasing look angle in figure 5.2.3 H. Notice the extremely large effective reflection coefficient resulting from the combined array pattern of figure 5.2.3 H.

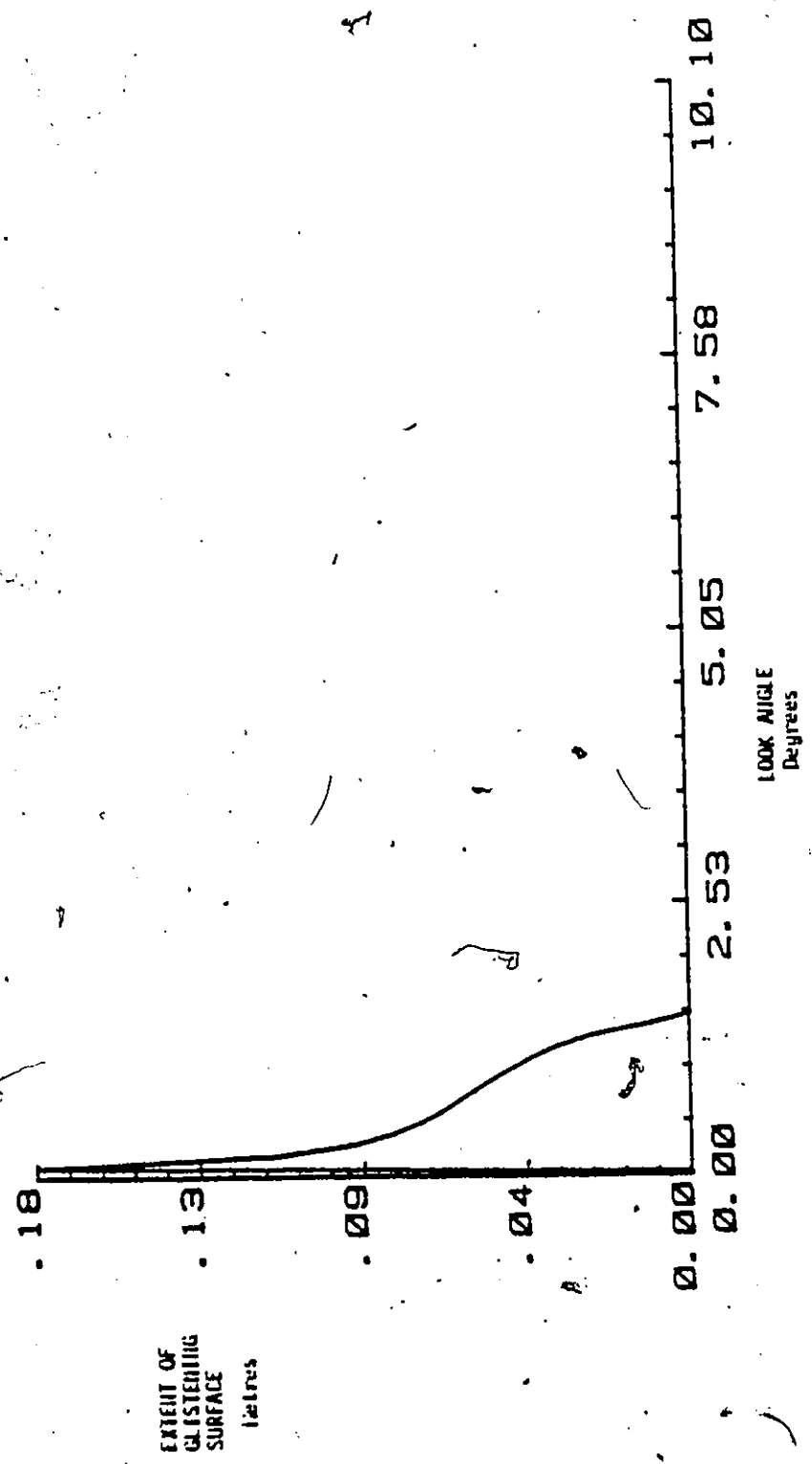


Figure 5.2.3.A Extent of glistening surface Case II.  $\phi_0 = .01$  radians,  $a_n = .15$  metres,  $\theta_0 = .25$  degrees.

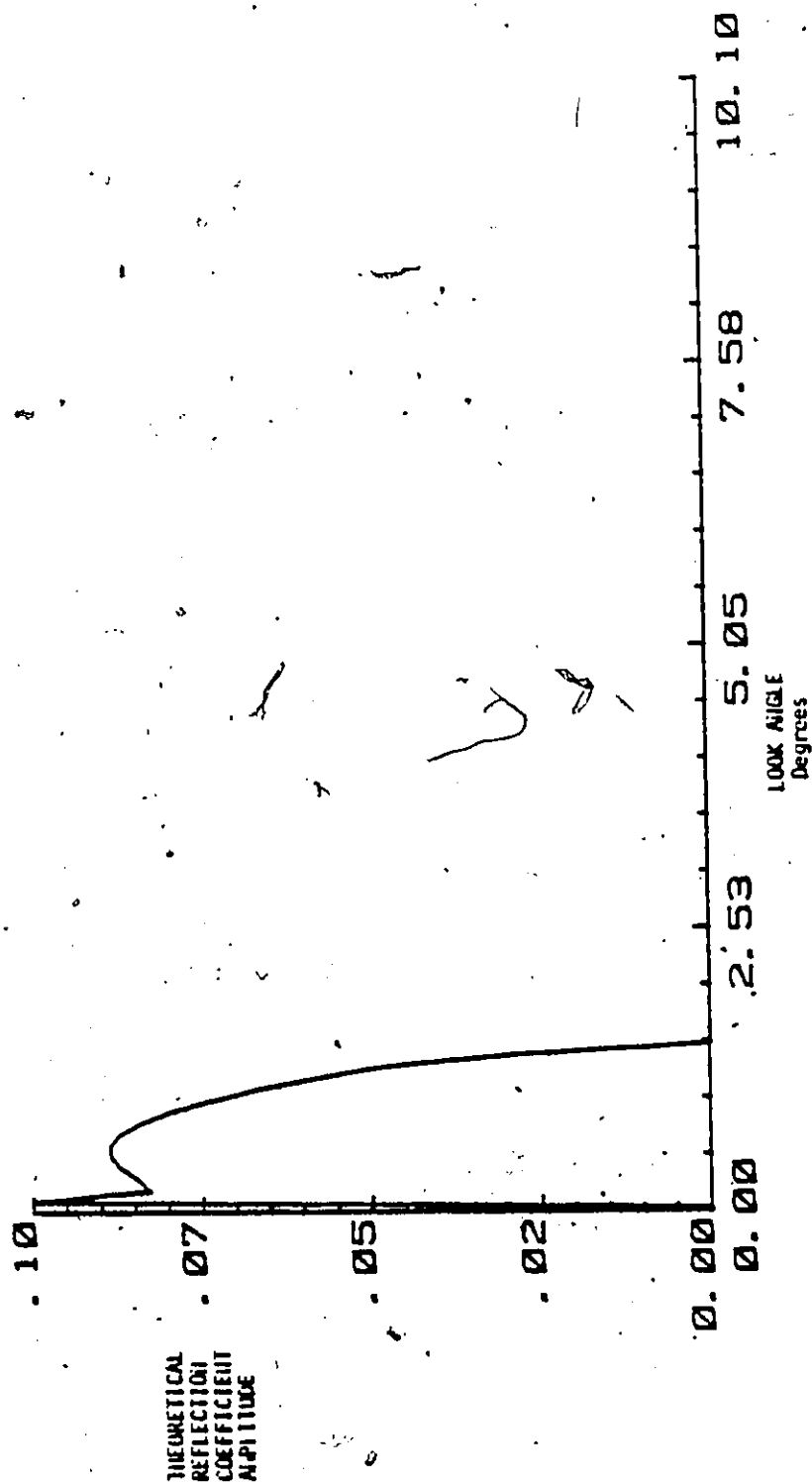


Figure 5.2.3.3 Magnitude of the diffusion reflection coefficient (theoretical)  
 Case II  $\theta_0 = .01$  radians,  $\sigma_n = .15$  metres,  $\phi_s = .25$  degrees.



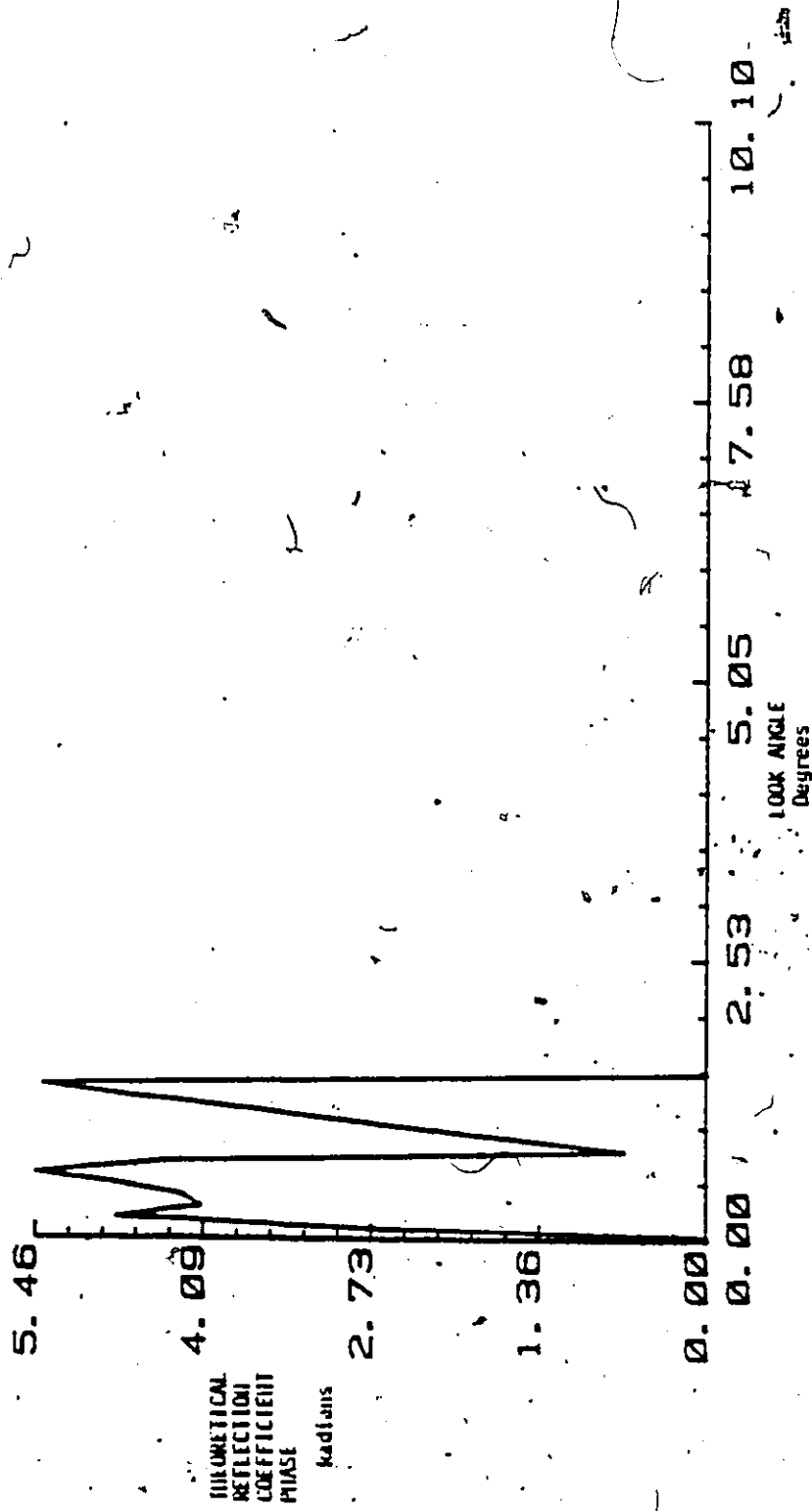


Figure 5.2.3.C Phase of the diffuse reflection coefficient (theoretical) Case II:  $\theta_0 = .01$  radians,  $\sigma_h = .15$  metres,  $\theta_c = .25^\circ$  degrees.

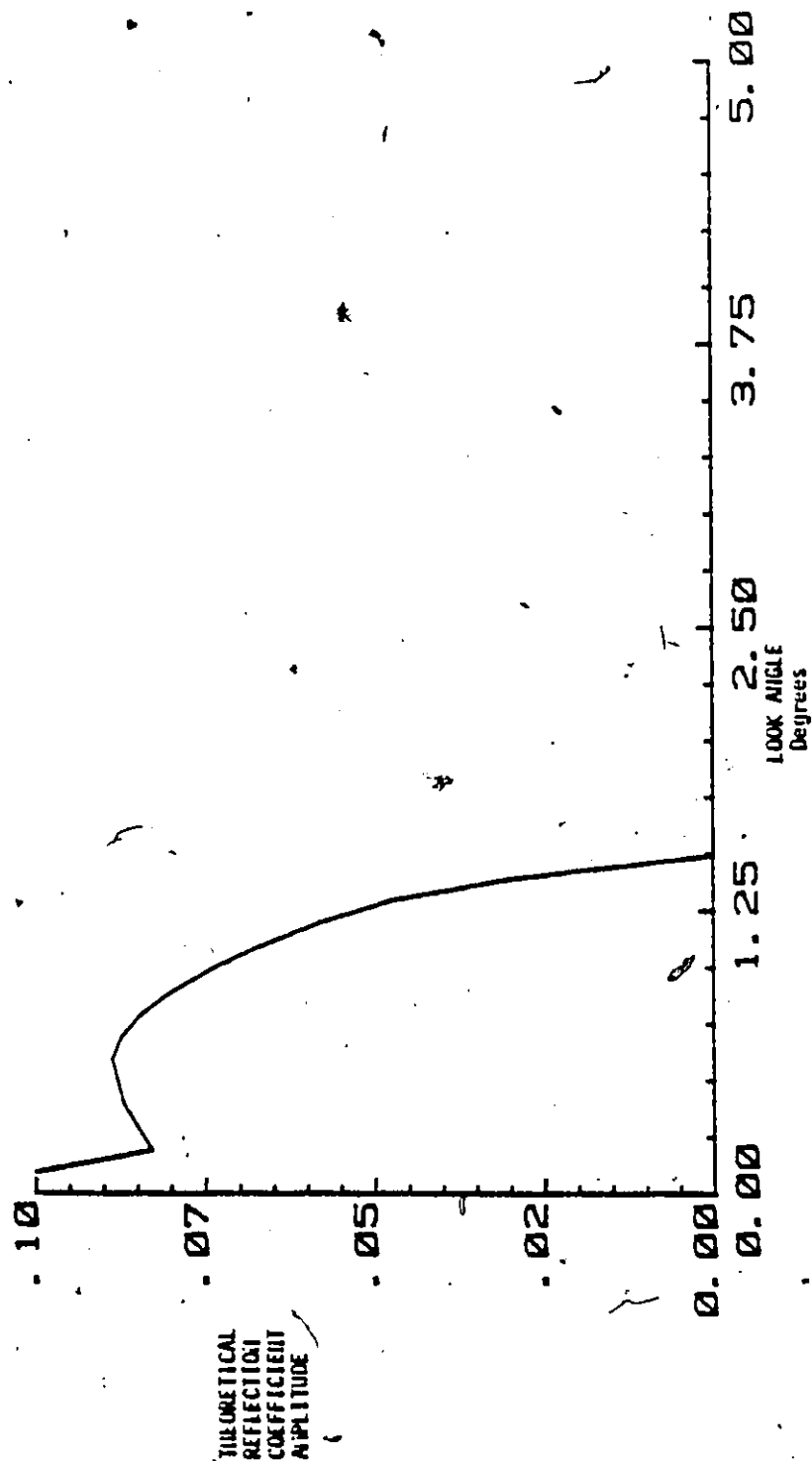


Figure 5.2.3.0 5.0 degree blow-up of the theoretical diffuse reflection coefficient's magnitude Case II  $\theta_0 = .01$  radians,  $\alpha_n = .15$  metres,  $\phi_n = .25$  degrees.

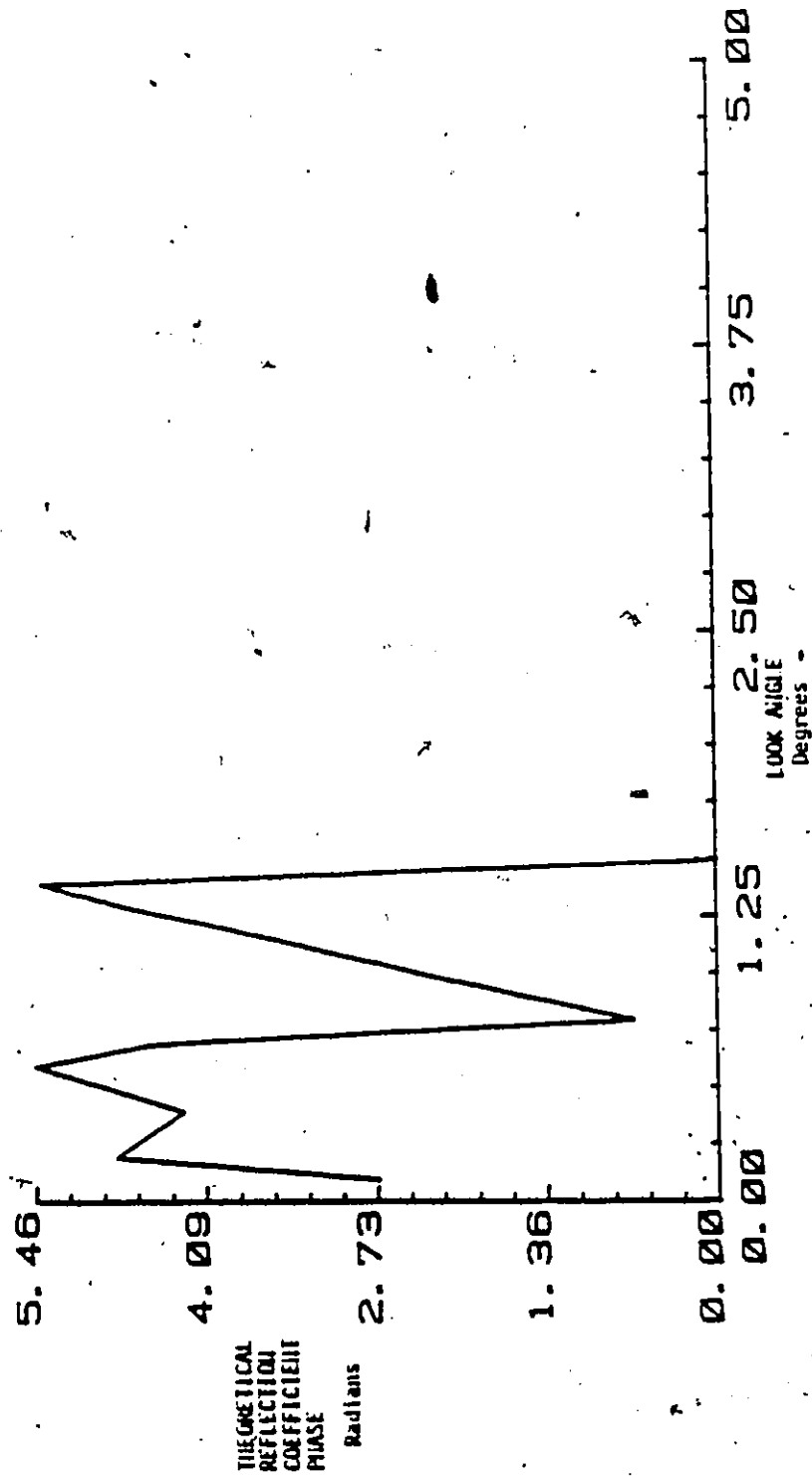


Figure 5.2.3.E 5.0 degrees blow-up of the theoretical phase of the diffuse reflection coefficient Case II  $\theta_0 = .01$  radians,  $d_h = .15$  metres,  $\theta_c = .25$  degrees.

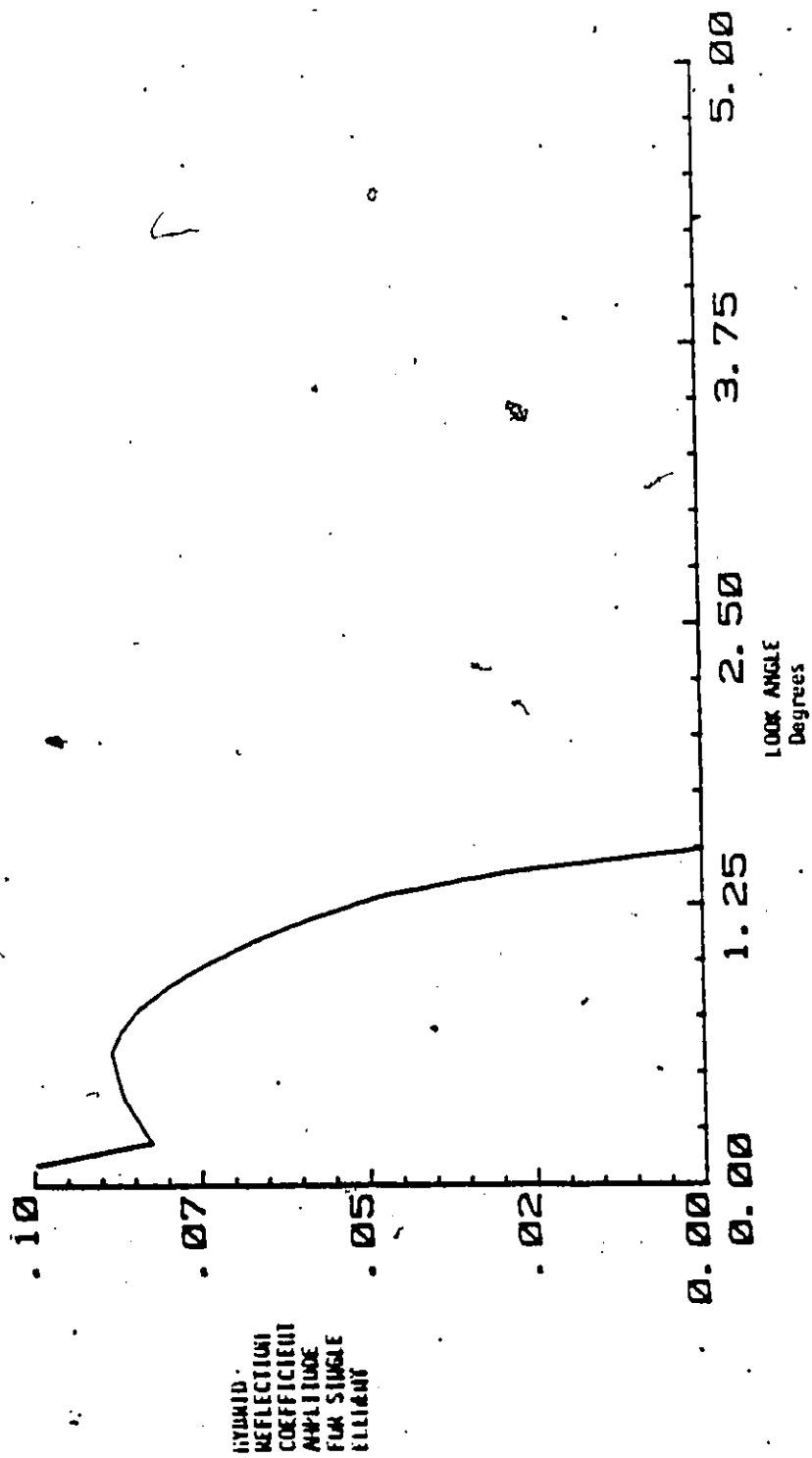


Figure 5.2.3.F Magnitude of the reflection coefficient with experimental element pattern applied. Case II  $\phi_0 = .31$  radians,  $\alpha_h = .15$  metres,  $\theta_c = .25$  degrees..

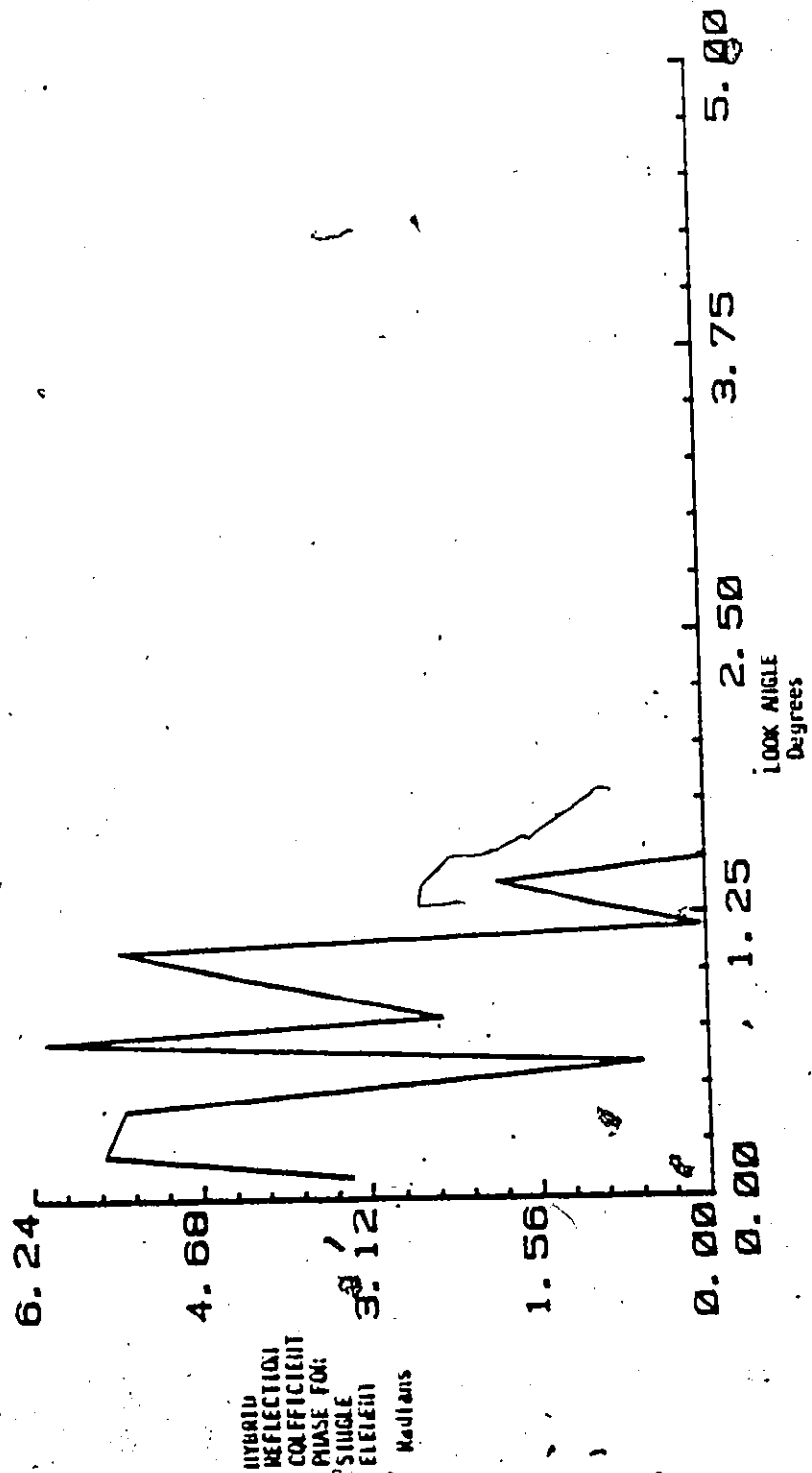


Figure 5:2.3.G Phase of the reflection coefficient with experimental element phase applied. Case II  $\theta_0 = .01$  radians,  $\sigma_h = .15$  metres,  $\theta_e = .25$  degrees.

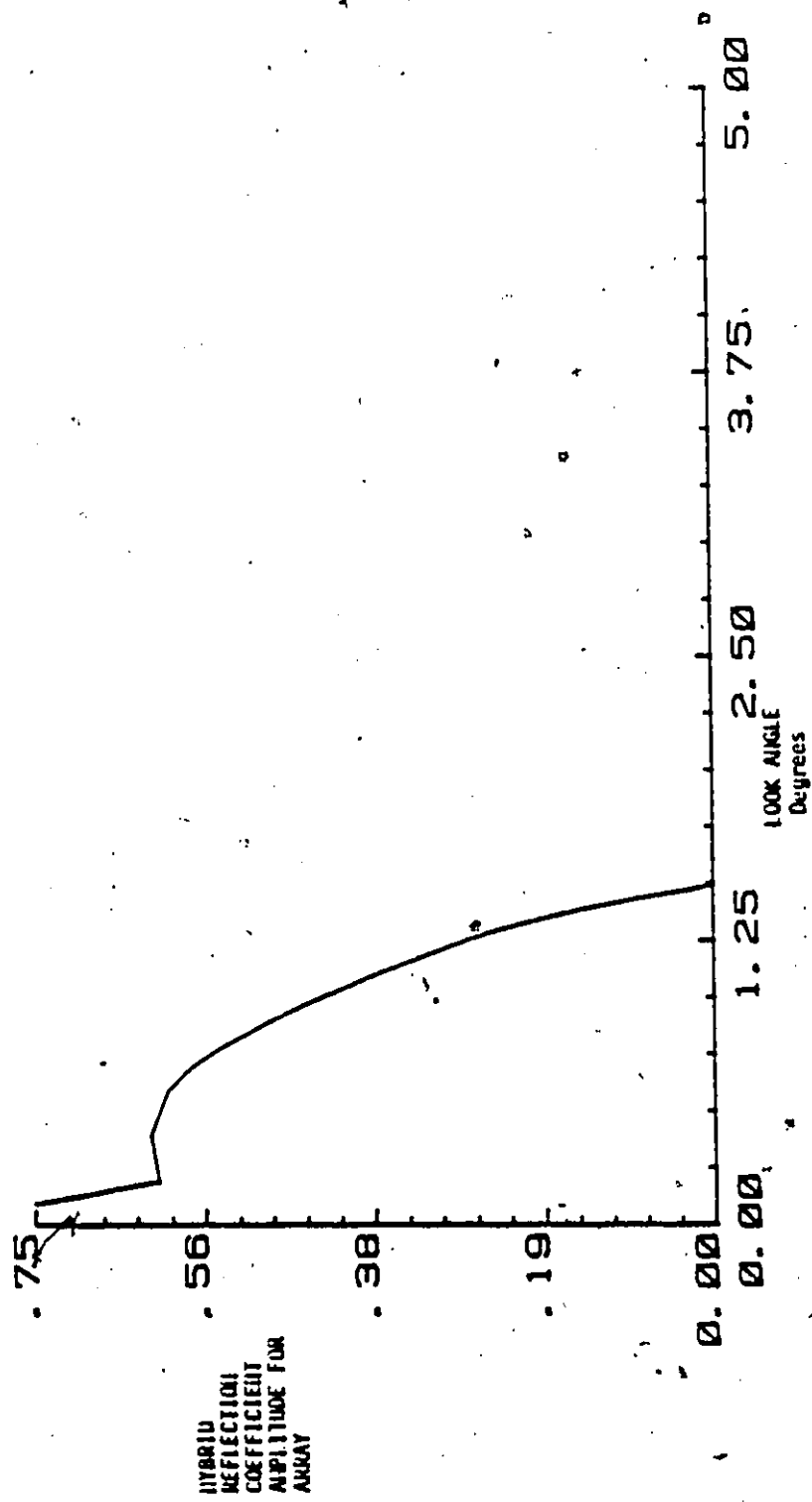


Figure 5.2.3.H Magnitude of the reflection coefficient for the combined array pattern. Case II  $\beta_0 = .01$  radians,  $\sigma_n = .15$  metres,  $\theta_c = .25$  degrees.

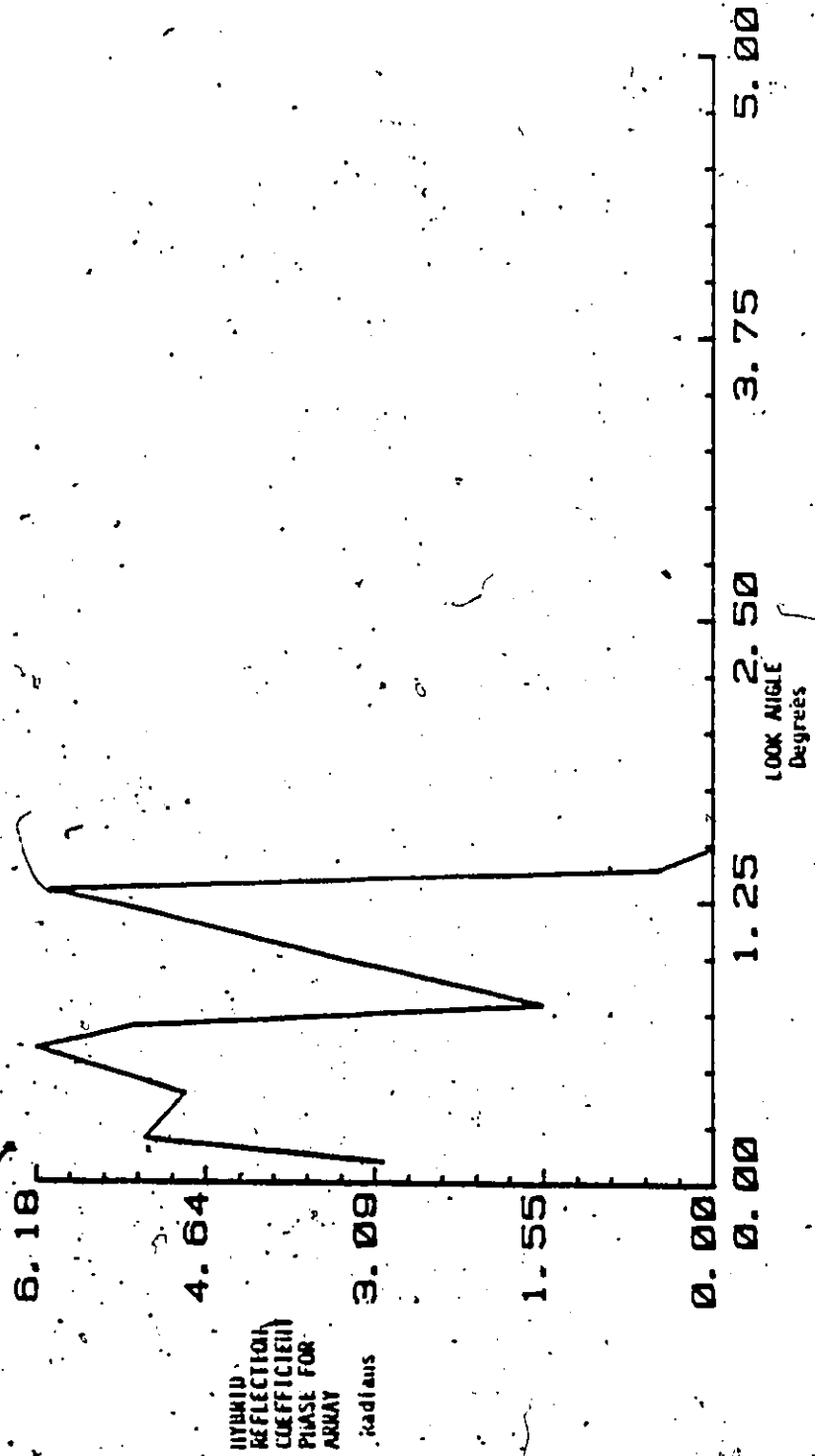


Figure 5.2.3.1. Phase of the reflection coefficient for the combined array pattern. Case II  $\theta_0 = .01$  radians,  $\lambda_n = .15$  metres,  $\theta_s = .25$  degrees.

#### 5.2.4 Case III

Keeping the radar at a height of 5 m, target at a range of 10 km, the values of  $\beta_0$  and  $\sigma_h$  at .01 and .15 respectively, the target was raised to an elevation of -2.5 degrees. Once again the figures are arranged in the same previous fashion. The glistening surface of figure 5.2.4 A is now somewhat symmetric about the specular reflection point of 2.5 degrees. This same symmetry is observed in the diffuse reflection coefficient of figure 5.2.4 B and its blow up (5.2.4 D). Notice that the  $\rho_d = 0$  point on the left is missing; this is because there is no data point within the glistening surface that corresponds to it. Since it has a value of zero, its absence makes no difference.

Applying the element pattern to this curve results in figure 5.2.4 F with no apparent change.

The combined pattern of figure 5.2.4 H shows a small amount of gain and shaping caused by the side lobe which this distribution is in since the main beam has been centred on the target at -2.5 degrees.



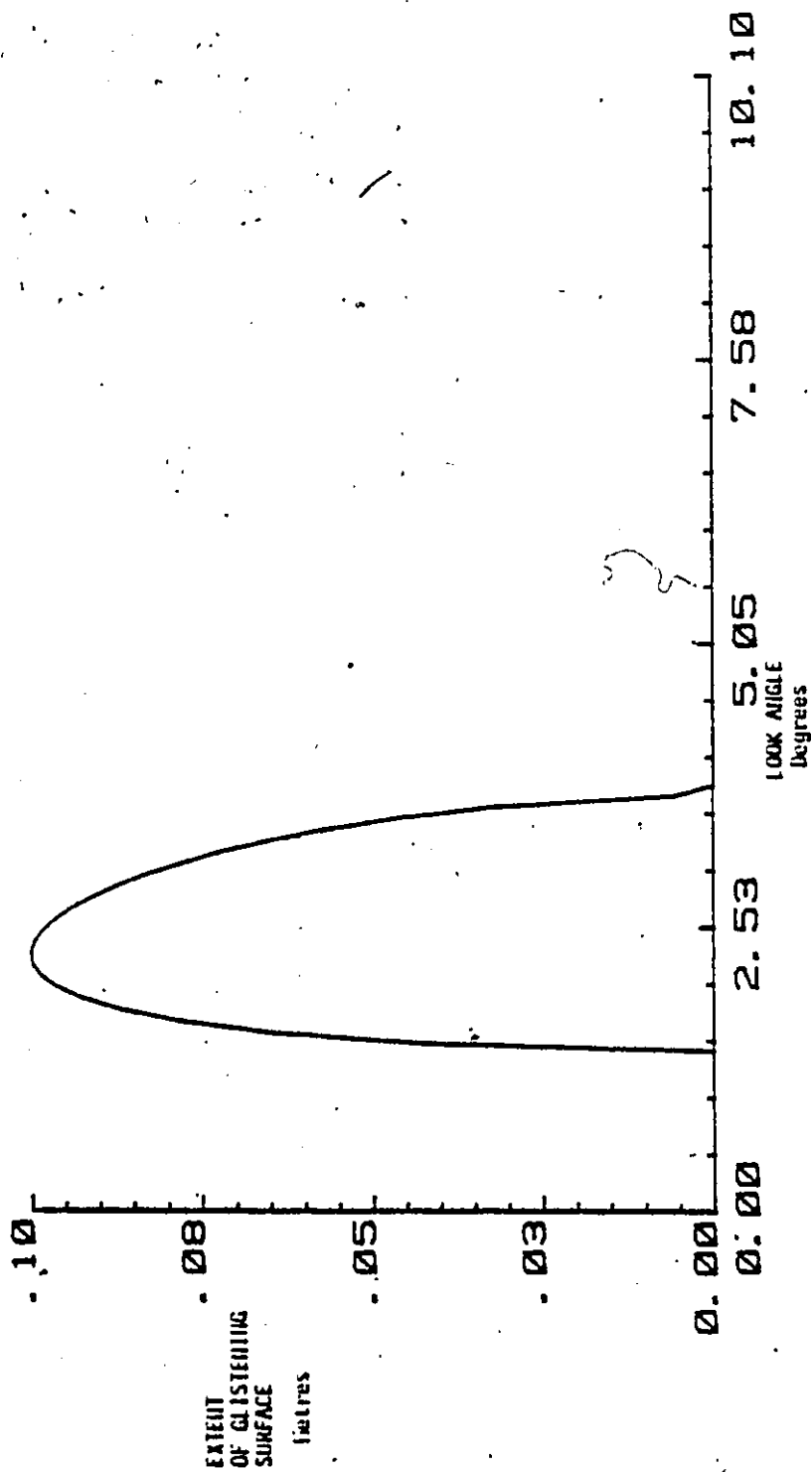


Figure 5.2.4.A Extent of glistening surface. Case III  $\phi_0 = .01$  radians,  
 $\sigma_n = .15$  metres,  $\theta_0 = 2.5$  degrees.

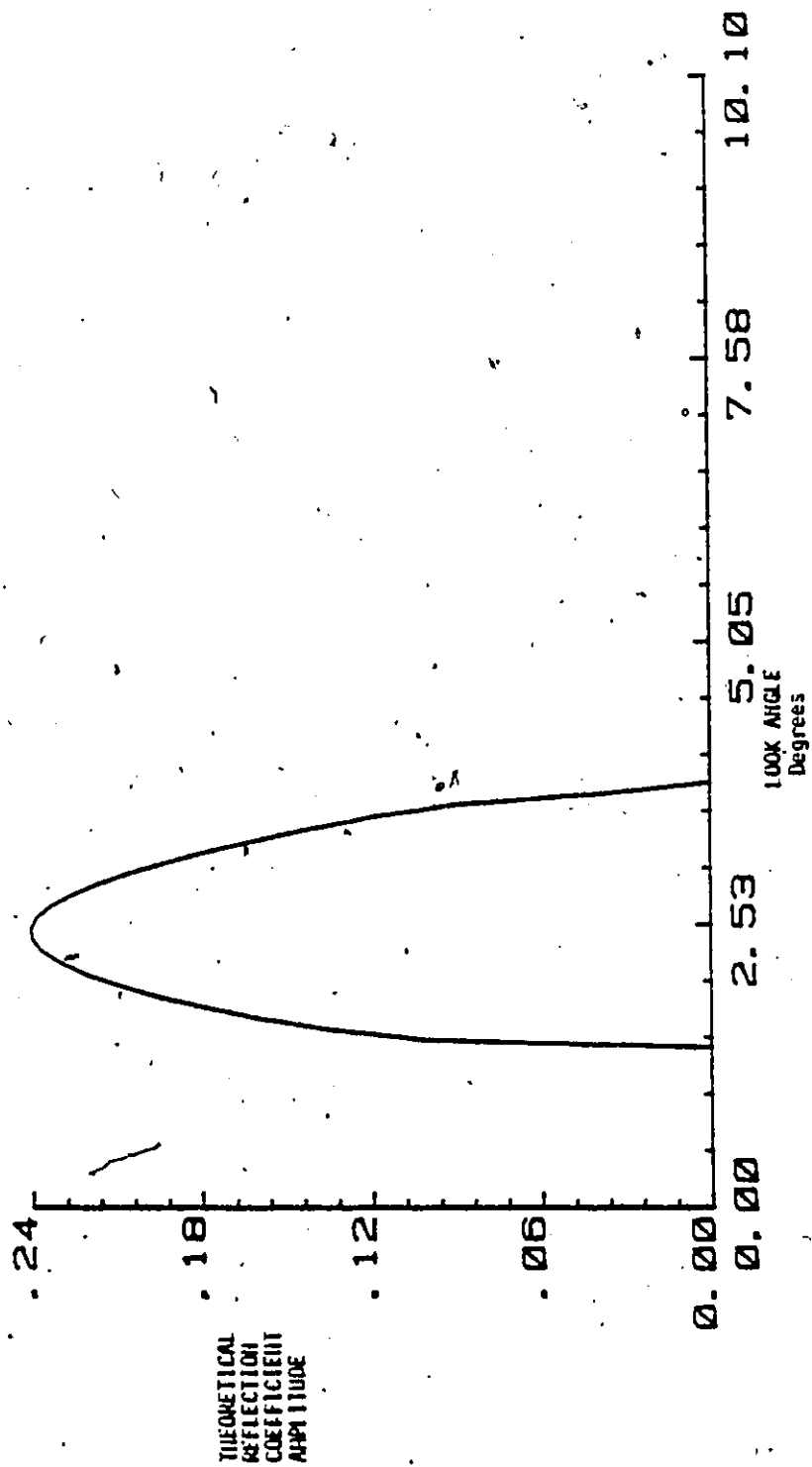


Figure 5.2.4.8 Magnitude of the diffusion reflection coefficient (theoretical).  
 Case III  $\phi_0 = .01$  radians,  $\sigma_h = .15$  metres,  $\phi_s = 2.5$  degrees.

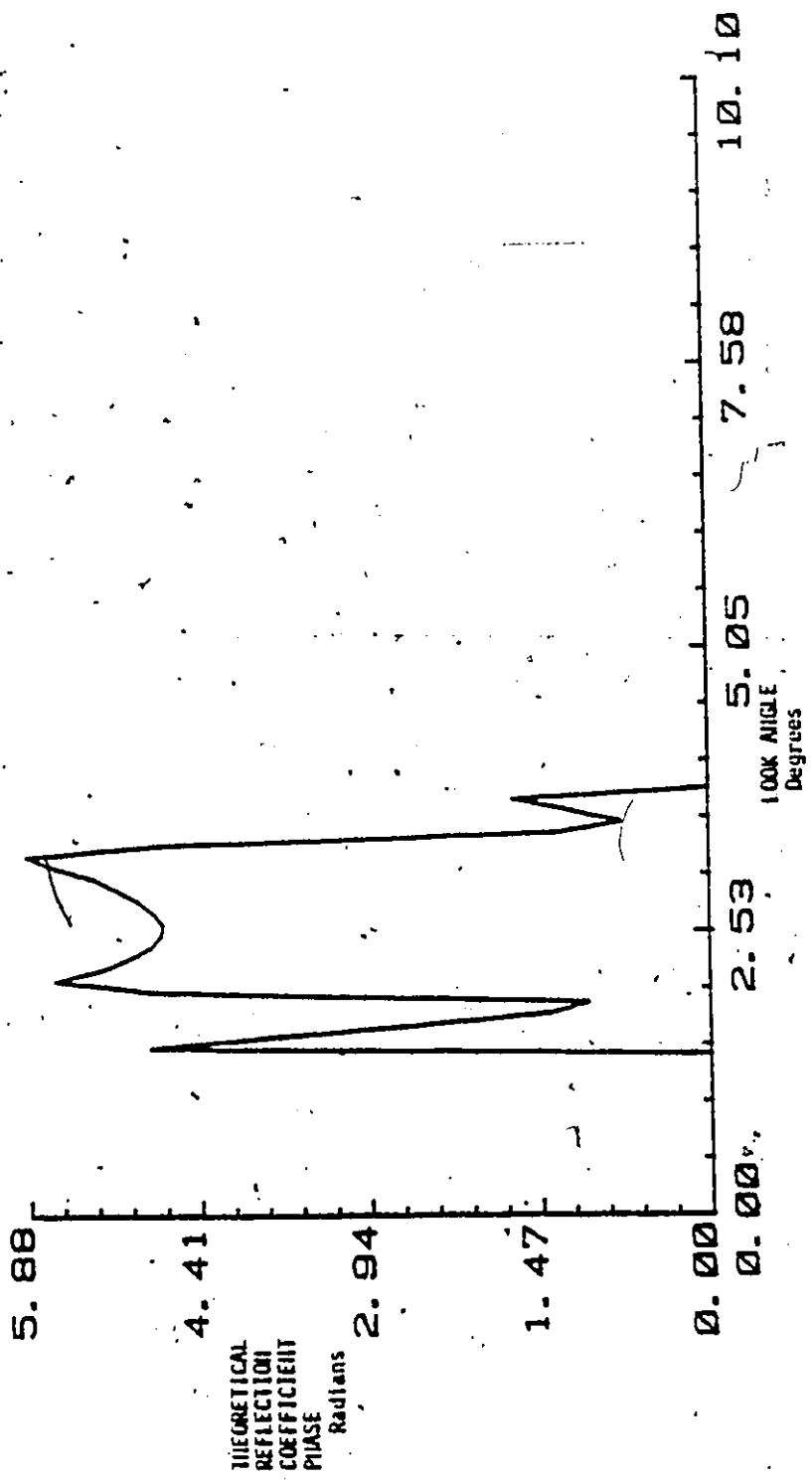


Figure 5.2.4.C Phase of the diffuse reflection coefficient (theoretical).  
Case III  $\theta_0 = .01$  radians,  $\sigma_n = .15$  metres,  $\alpha_s = 2.5$  degrees.

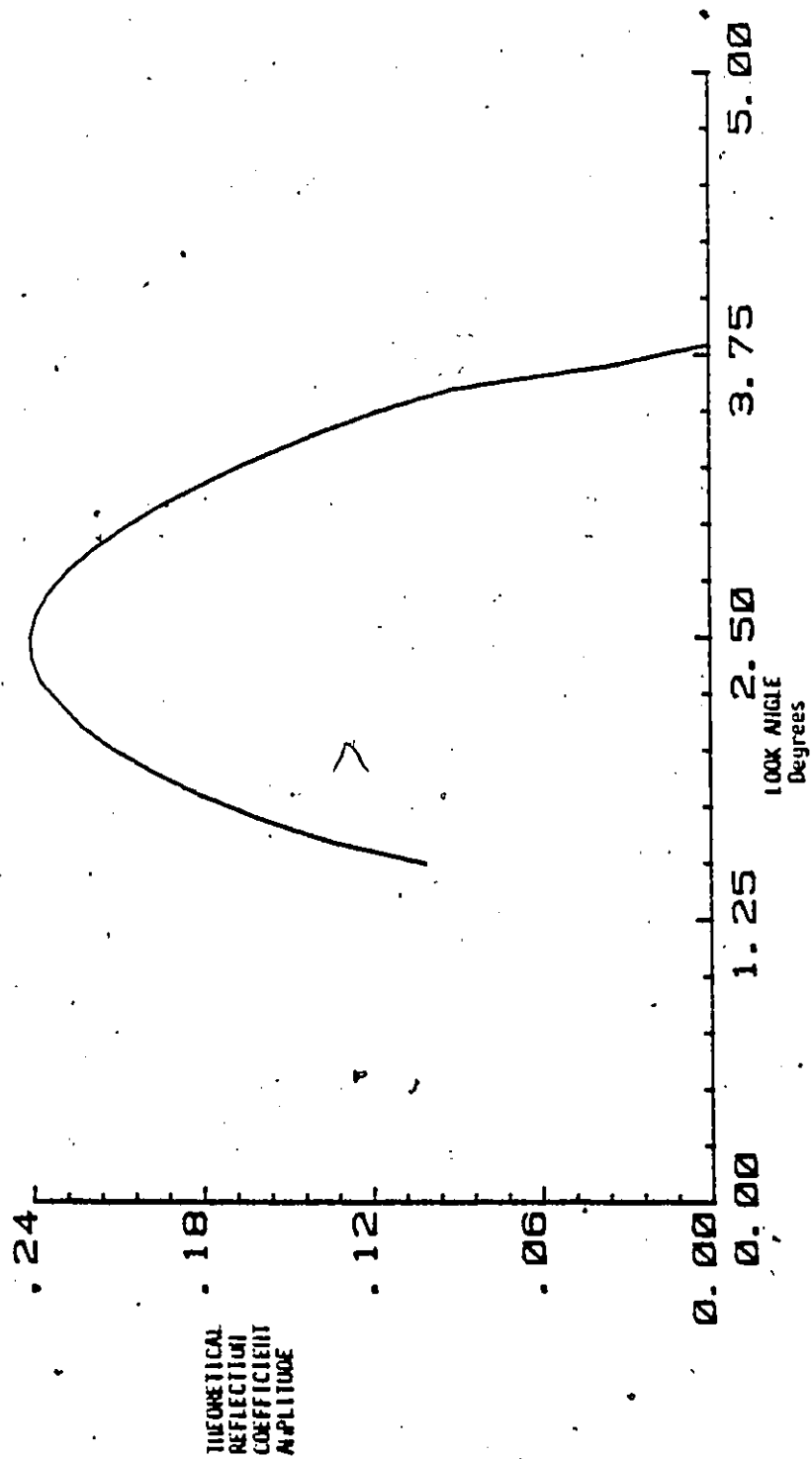


Figure 5.2.4.0 5.0 degree blow-up of the theoretical diffuse reflection coefficient's magnitude. Case III  $\theta_0 = .01$  radians,  $\alpha_h = .15$  metres,  $\theta_t = 2.5$ , degrees.

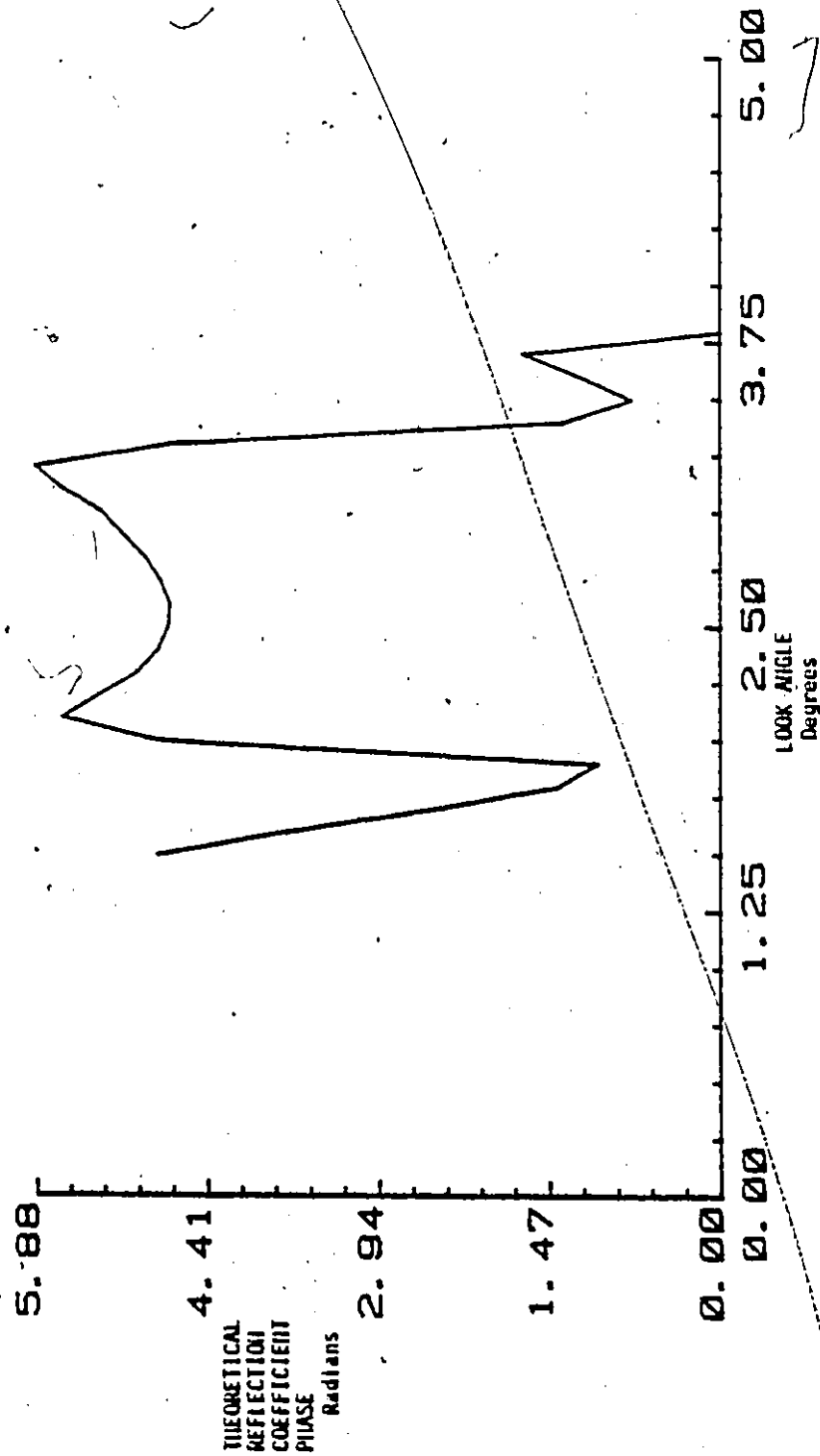


Figure 5.2.4.E 5.0 degree blow-up of the theoretical phase of the diffuse reflection coefficient. Case III  $\theta_0 = .01$  radians,  $\alpha_h = .15$  metres,  $\theta_c = 2.5$  degrees.

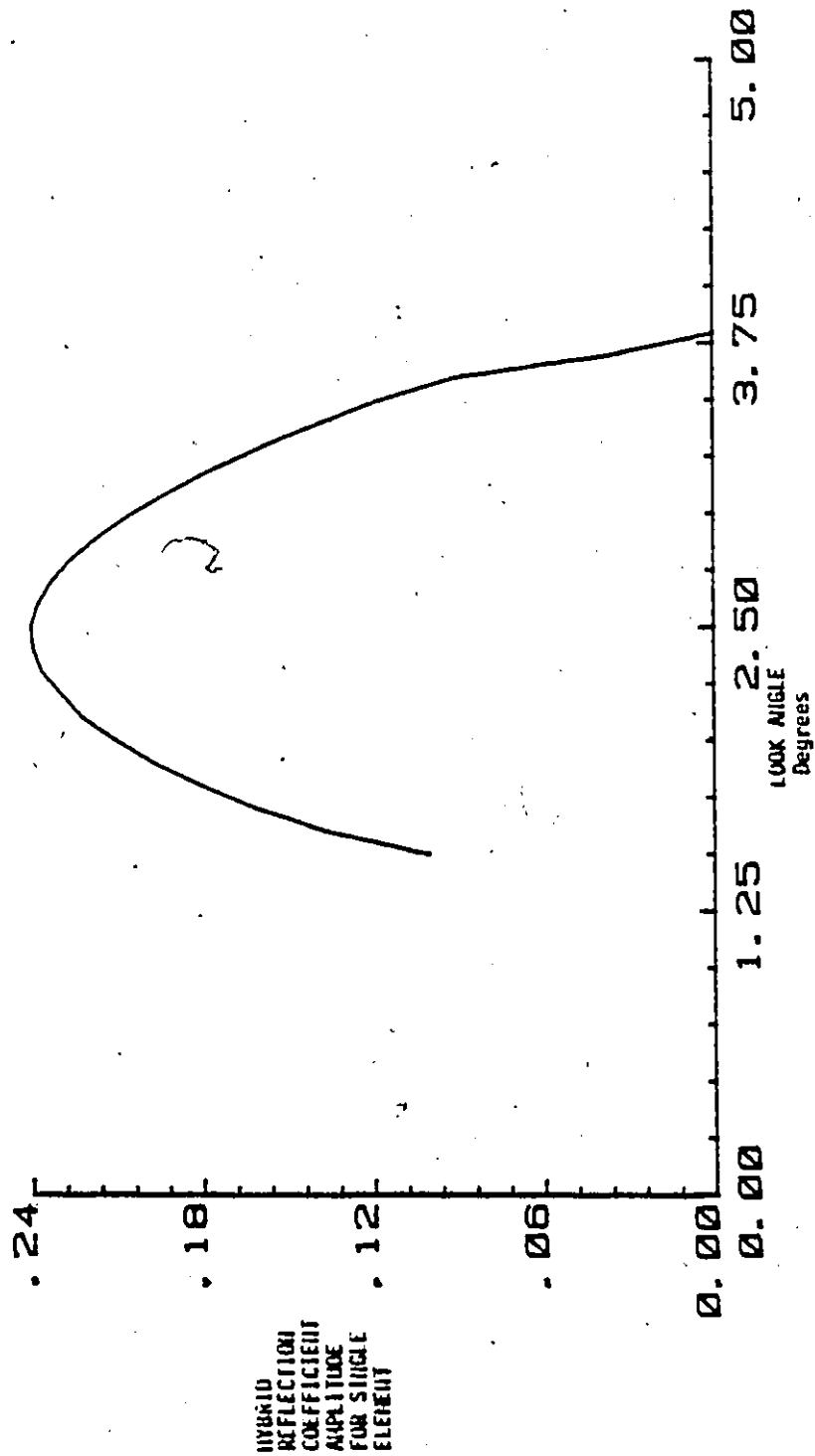


Figure 5.2.4.F Magnitude of the reflection coefficient with experimental element pattern applied. Case III  $\theta_0 = .01$  radians,  $\sigma_h = .15$  metres.  $\theta_c = 2.5$  degrees.

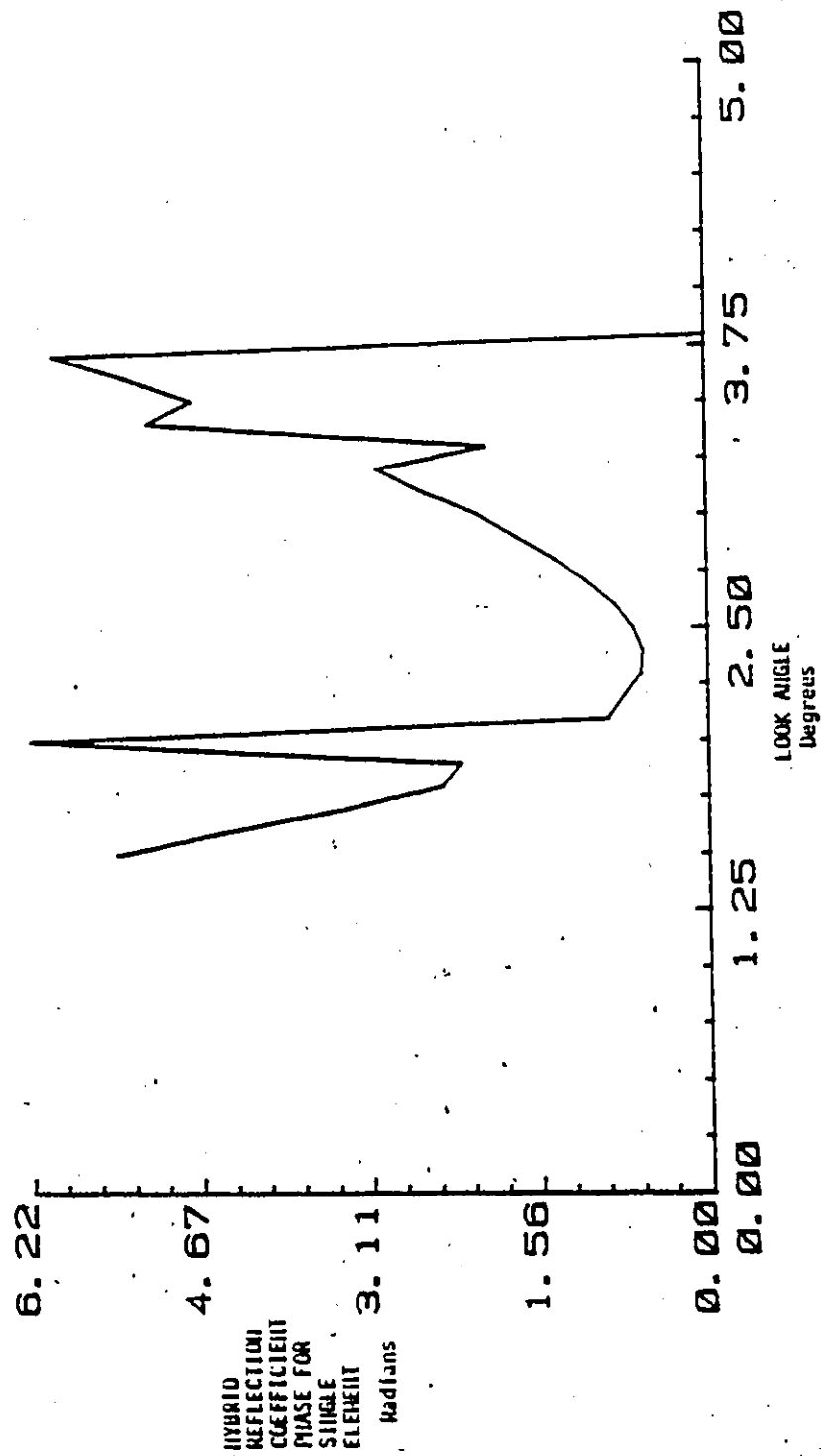


Figure 5.2.4.G Phase of the reflection coefficient with experimental element phase applied. Case III  $\theta_0 = .01$  radians,  $\alpha_h = .15$  metres,  $\theta_c = 2.5$  degrees.

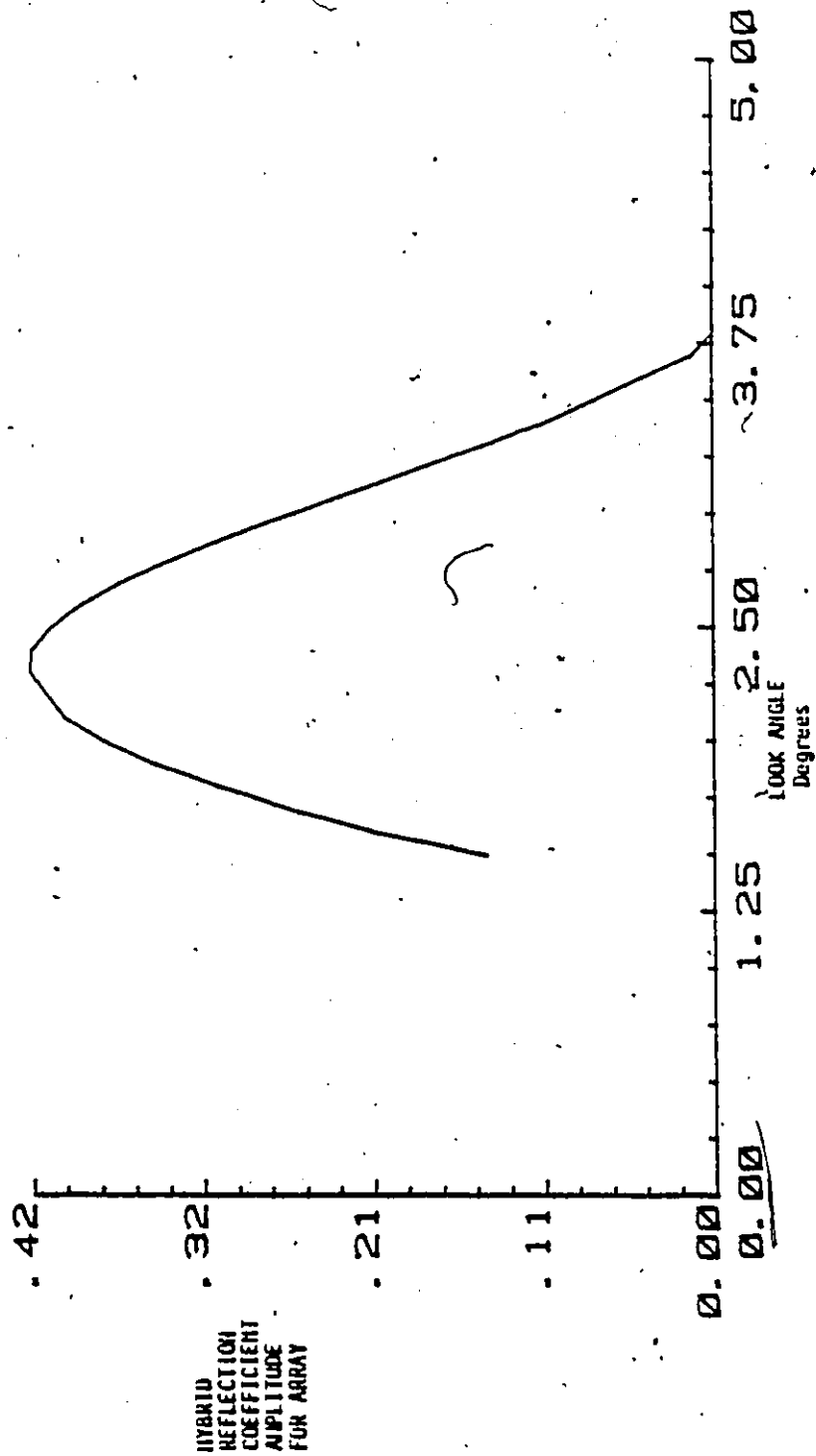


Figure 5.2.4.H Magnitude of the reflection coefficient for the combined array pattern. Case III  $\theta_0 = .01$  radians,  $\sigma_h = .15$  metres,  $\theta_r = 2.5$  degrees.



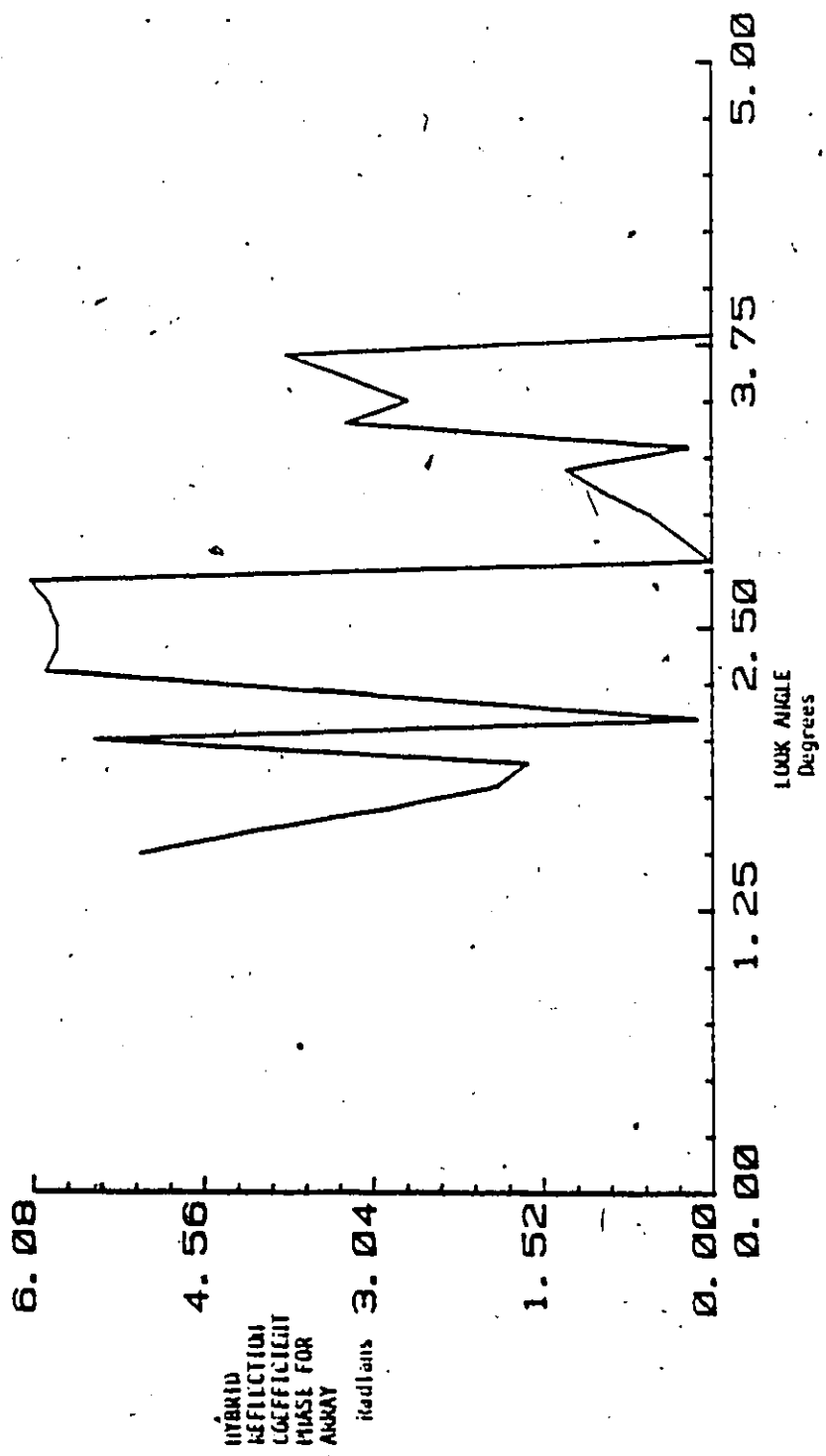


Figure 5.2.4.1 Phase of the reflection coefficient for the combined array pattern. Case III  $\theta_0 = .01$  radians,  $\alpha_h = .15$  metres,  $\theta_c = 2.5$  degrees.

### 5.2.5 Summary of Experimental Results

Although a far larger amount of power is directed in the vicinity of the radar when  $\beta_0$  is large, the amount of power observed maybe much smaller. For example when  $\beta_0$  was large as in Case I, the reflection coefficient was distributed over 11.9 degree; however, after applying the array pattern, the effective part of this between 0. and 3.0 degrees. The case when  $\beta_0$  was moderate (.01) and the elevation angle was .25, all of the glistening surface was within the main beam. Although the glistening surface was smaller and the resultant total power smaller, the reflection coefficient was much larger. If, however, the target is moved out of the main beam as in case III, the effective reflection coefficient is suppressed by the gain of the sidelobe.

It is for these reasons that we conclude that the most undesirable conditions occur for moderate  $\beta_0$ 's and very low target elevations. Note, however, that this analysis has been completed assuming a flat earth. If we were to consider the effects of a curved earth we would find that as the target got very low in elevation a large percentage of the glistening surface would lie beyond the radar's visible horizon. This may imply that moderately low targets provide more undesirable condition (i.e. more diffuse power in main beam) than do very low ones.

## CHAPTER 6

### CONCLUDING REMARKS

#### 6.1 Conclusions

In this thesis it was desired to produce a laboratory apparatus capable of generating a multipath environment appropriate to the study of diffuse multipath as it occurs in the case of low elevation tracking. Three simulation methods were investigated (holographic, phased array, and hybrid) with the hybrid model being implemented. The results of this implementation were displayed in Chapter 5.

From these results it can be seen that by using the hybrid method it is possible to produce a multipath environment containing virtually any number of multipath components. By using an array of some predesignated pattern as the receiver, it is possible to observe the ways in which this multipath will affect it. In the investigation of the effects of diffuse multipath on a given receiver, it was found that antenna pattern played an important role. It was found that large amounts of power were reflected in the direction of the receiver when the RMS surface slope ( $\theta_0$ ) was large. This was largely due to the fact that the glissening surface extended over a large range of angles. The power density was found to be higher for more moderately sloped surfaces, which leads to interesting results when considering

antenna aperture. If, for example, we have a target at extremely low elevation above two surfaces, the first being rough (large surface slope), the second moderately rough, we find the second case to be potentially more damaging to the radar. This is due to the fact that, if the target is at low elevation, the main lobe of the antenna pattern will lie on top of the target and a large amount of energy near the horizon. Although it is true that the target and its image are separated, for decreasing  $\beta_0$  the fact remains that this distance may still be unresolvable. The antenna will be affected mainly by the main beam, - since much of the remaining energy is suppressed. This means that the surface generating the largest power density within the main lobe will be the most damaging; and this has been found (for very low targets) to be the surface that is rough but not so rough that the power is extremely disperse.

If, however, the target and its image are separated by a large amount, without a doubt, the rougher the surface, the greater the effect on the radar. This is due to fact that as  $\beta_0$  decreases, the diffuse multipath becomes more and more symmetrical about the specular point with far less spread. This means that the power will move away from the horizon as the surface gets smoother and its effect lessened by the smaller sidelobe gain.

## 6.2 Recommendations

It is this author's opinion that there is little hope of

adequately resolving a target and the diffuse power reflected at small angles, unless we use the diffuse image to somehow enhance what is known about the target. The knowledge that there will be a sharp peak at low angles for low targets over rough and moderately rough surfaces should be of great value when tracking under such circumstances.

In conclusion, it seems the next logical step is to collect real data with a known target geometry for the worst possible case and apply a little creative thinking when approaching the signal processing.

## REFERENCES

- 1) Nathanson, Fred. E., Radar design principles: signal processing and the environment. New York: McGraw-Hill Book Co., [1969]
- 2) Meyer, Daniel P., Mayer, Herbert A., Radar target detection: handbook of theory and practice New York: Academic Press, [1949].
- 3) Skolnik, Merrill Ivan, Radar handbook, 1927 -. New York: McGraw-Hill, [1970].
- 4) Jakes, Williams C., Microwave Mobile Communications. New York: Wiley, [1974].
- 5) Sollenberger, T.E., "Multipath Phase Errors in CW-FM Tracking System". IRE TRANS. AP-3, No. 4, Oct. 1955, pp 185-92.
- 6) Long, Maurice W., Radar reflectivity of land and sea, Lexington, Mass.: Lexington Books, [1975].
- 7) Dedham, M.A., Radar Anti-jamming techniques: Artech House, [1979].
- 8) Beckmann, Petr, The Scattering of Electromagnetic Waves from Rough Surfaces, New York: MacMillan, [1963].
- 9) Barton, David K., "Low Angle Radar Tracking", Proceedings of IEEE, Vol 62 No.6, June 1974, pp 682-704.
- 10) Caeccacci, P.F., Russo, V., Scheggi, A.M., "Holographic Antennas", Proceedings of the IEEE, December 1968, pp 2165-2167.
- 11) Zajac, Alfred, Optics/Hecht, Eugene. Reading, Mass.: Addison-Wesley Pub. Co., [1974].
- 12) Farhat, Nabil H., "Holographically Steered Millimeter Wave Antennas", IEEE Transactions on Antennas and Propagation, Vol AP-28, No.4, July 1980 pp 476-480.
- 13) Brown, R.G., Sharpe, R.A., Hughes, W.L., Post, R.E., Lines, Waves and Antennas: The Transmission of Electric Energy, 2nd Ed. New York: Ronald Press Co., [1961].

APPENDIX A  
SYSTEM HARDWARE

## APPENDIX A

### A.1.1 Microwave

The microwave source in this system (Fig. A.1) is a 27 dBm (500 milliwatt) 9.97 GHz klystron oscillator. This power is divided in two (3 dB down) by way of a hybrid tee, which feeds the transmitter and receiver. On route to the transmitter, the first component encountered is an isolator. Its purpose is to suppress reflections caused by the apparent impedance mismatch of the next component, a precision variable phase shifter. This phase shifter is used to set the phase of the transmitted signal with respect to the in-phase local oscillator. At the output of the phase shifter is a klystron amplifier. This device adds 10 dB of gain to the transmitted signal, making it 34 dBm. Once again we encounter an isolator, this time it is used to attenuate reflected power caused by mismatches after this point. At this point, the rectangular waveguide is joined to a fifty-foot section of elliptical waveguide (VSWR test is found at end of this section). At the far end of the anechoic chamber, the elliptical waveguide is joined to a section of semi-ridged coaxial cable by means of an N-type bulk head connector. The signal, now around 28 dBm, is transmitted towards the receiver by means of a 25 dB horn.

The route from klystron to receiver mixers is first attenuated by 7 dB. This signal is then split (3 dB down) to provide in-phase and quadrature phase oscillators. The in-phase arm passes through an



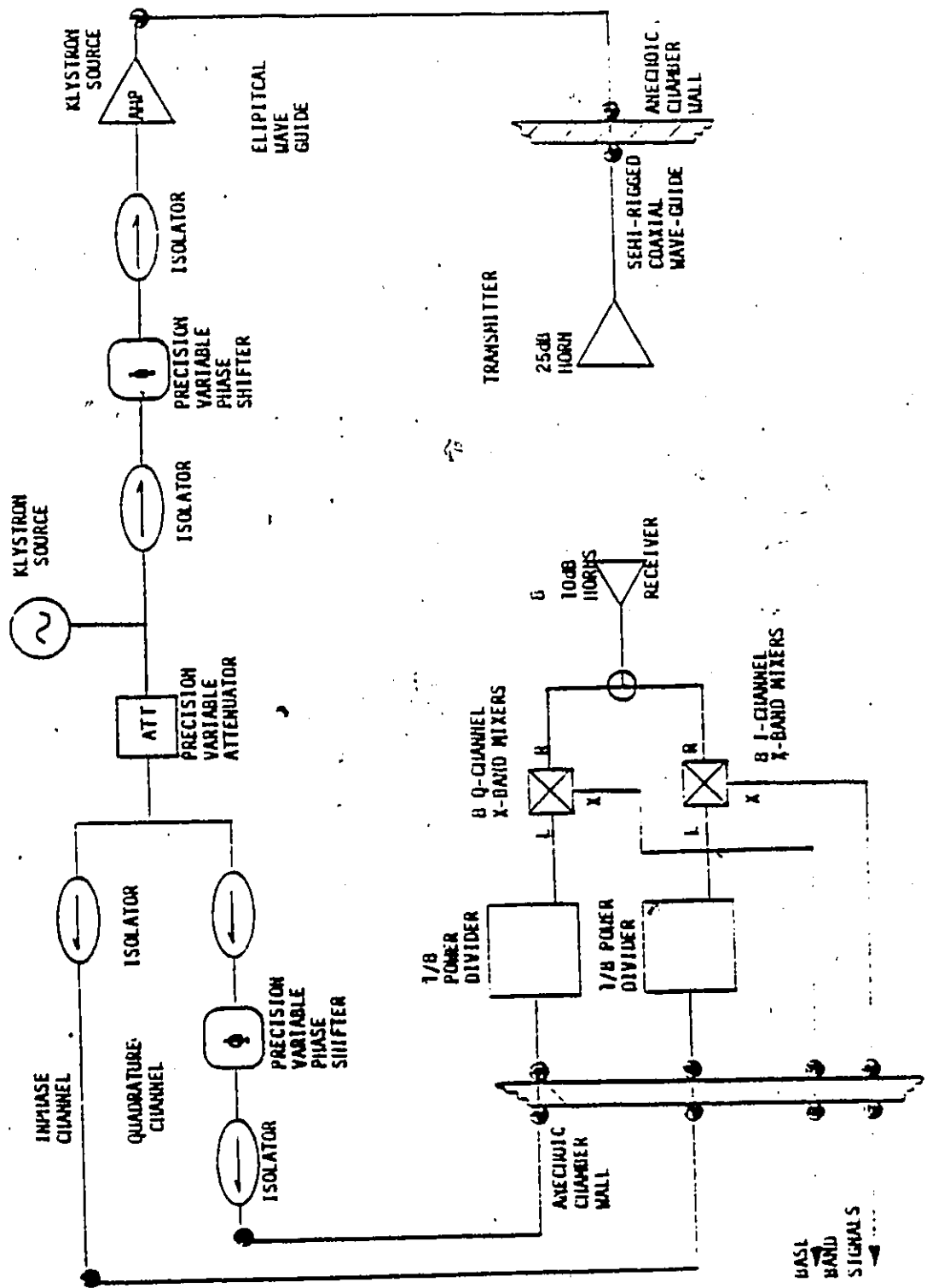


Figure A.1 Microwave hardware for hybrid multipath simulation system.

isolator, then continues to microwave hardware which is identical to the quadrature side. The quadrature arm first encounters an isolator suppressing phase shifter mismatches. This phase shifter is used to bring the two local oscillators in quadrature. Like the in-phase side, the quadrature side passes through another isolator. These isolators are used to attenuate reflection from the one by eight power dividers that follow. These two power-dividers are used to provide sixteen local oscillators (eight I, eight Q). Each of these signals (5 dBm) enters the L port of the RHG DM 8-12 double balanced mixers. The R port is fed from one side of a two way power divider dividing the power received from each of the eight element phased array 10 dB horns. The resulting base-band signal (port X) is then passed on to the data acquisition system.

#### A.1.2 VSWR Test Performed on New Elliptical Wave Guide

Figures A.2 and A.3 illustrate the test equipment used to measure the VSWR of the elliptical waveguide.

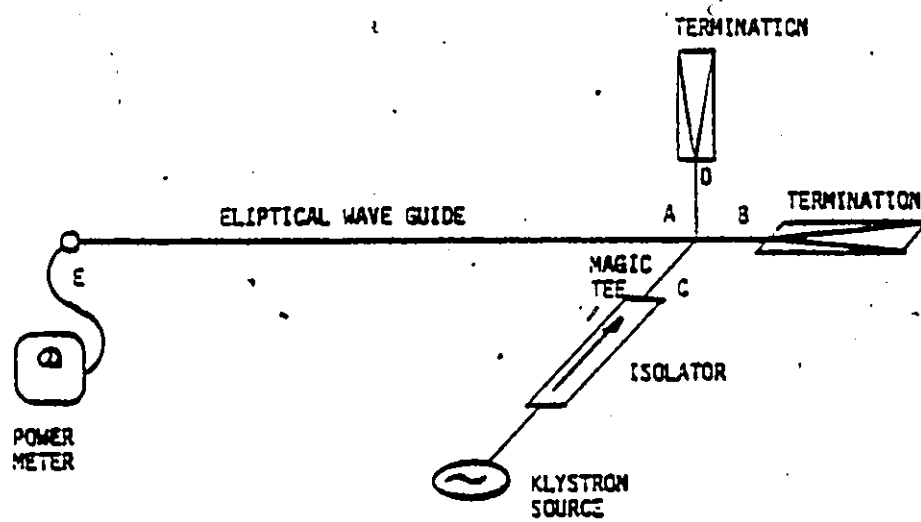
Forward Power

Figure A.2 Apparatus for forward power measurement.

Backward Power

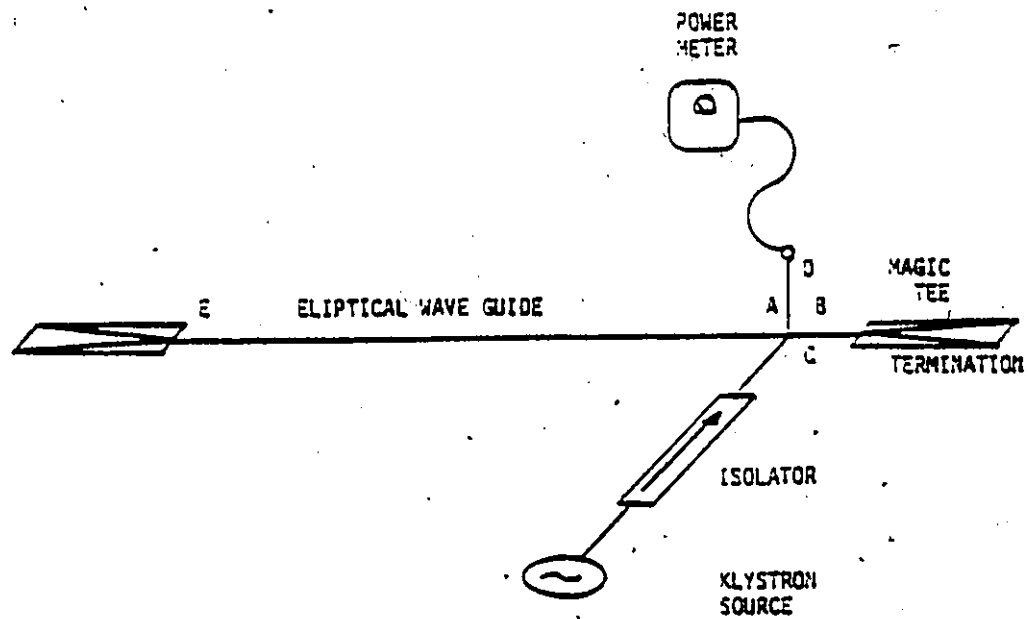


Figure A.3 Apparatus for reflected power measurement.

Let us first consider the operation of a Hybrid or Magic TEE of Fig.

A.4.

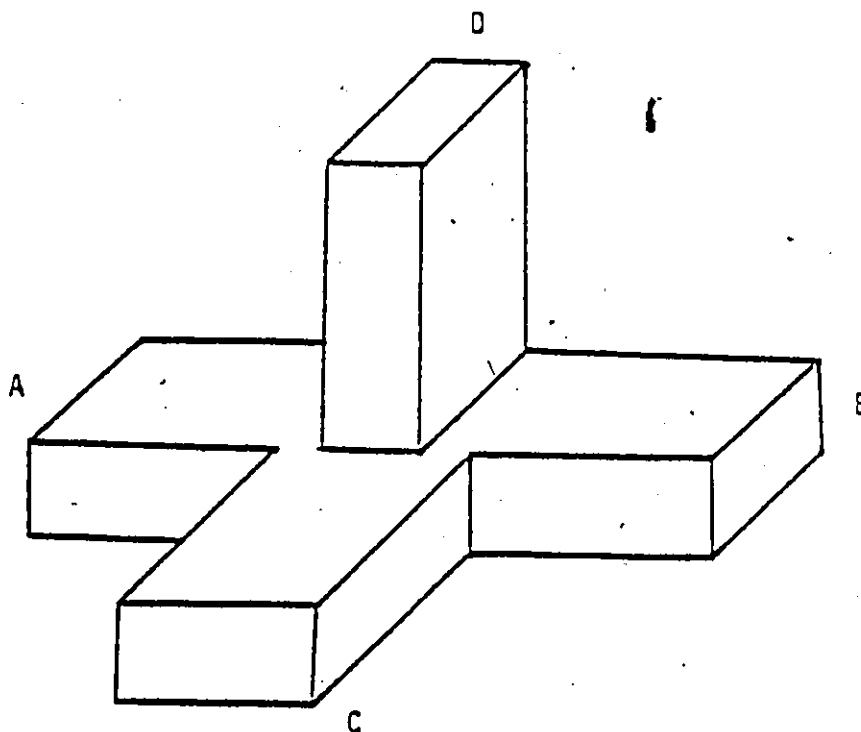


Figure A.4 Magic or Hybrid of Tee.

Energy transmitted into port C will be divided evenly between A and B, with none to D. If a signal is fed in A, its power will be divided evenly between D and C with no power transmitted to B [13]. The above two properties of the magic TEE will be sufficient to explain the operation of Figure A.2 and A.3.

In both Figures A.2 and A.3, the power transmitted to the cable through arm A is 3 dB down from that of the klystron source  $27 \text{ dBm} - 3 \text{ dBm} = 24 \text{ dBm}$ . This same power is transmitted through arm B. A matched

load or termination absorbs the power at B. An isolator located between arm C and our source attenuates any power reflected back from A. When measuring the forward power, a termination is placed at D to absorb the power at D reflected back from A. The transmitted power is then measured at the cable's end (E).

A matched load is placed at the end of the cable (E) when measuring the backward or cable mismatch reflected power. This load attenuates all power transmitted through the cable, so that the reflected power is due only to the cable characteristic impedance. The power reflected back into A is divided evenly between C and D. The portion going to C is attenuated by the isolator, while the part going to D is measured by the power meter. This means that the actual reflected power is 3 dB greater than that measured at D.

The reflection coefficient of the cable can then be calculated with equation A.1.

$$\begin{aligned} \rho &= \left[ \frac{\text{REFLECT POWER}}{\text{INCIDENT POWER}} \right]^{1/2} \\ &= \left[ \frac{2 \times \text{POWER AT D}}{\text{POWER AT E}} \right]^{1/2} \\ &= \log \left[ \frac{1}{20} (\text{PD}(\text{dbm}) + 3 \text{ dbm} - \text{PE}(\text{dbm})) \right] \end{aligned} \quad (\text{A.1})$$

The voltage standing wave ratio VSWR can then be calculated from equation (A.2)

$$\text{VSWR} = \frac{1 + \rho}{1 - \rho} \quad (\text{A.2})$$

The tests resulted in a VSWR of (1.48) which was considered acceptable.

### A.2.1 Data Acquisition System

#### Data Conversion:

The data acquisition system shown in Figures A.5 is based on a Burr-Brown SDM853 data acquisition system.

It has sixteen single-ended inputs, these signals being supplied by the eight in-phase and eight quadrature phase receiver outputs. These sixteen base band signals are first passed through passive low-pass filters with cut-off frequency of 200 Hz. The filter outputs are connected to two eight channel CMOS multiplexers. The channel selection is accomplished with use the of the four-bit address counter. The most significant bit selects the appropriate multiplexer, while the remaining three specify the channel number.

The selected channel now at the multiplexer output enters the positive side of a low drift, high speed instrumentation amplifier. The negative terminal is connected to the signal ground. The amplifier gain is controlled by means of a 2 K $\Omega$  external resistor and is presently set for a gain of 50. Next, the amplified signal (now in the range  $\pm 2.5$  V) is held by a sample and hold to the input of a 12-bit analog-to-digital converter.

The 12 data bits and 4 address bits are then sent via 50  $\Omega$  line drivers, as one 16-bit word to the HP 1000 computer.

### A.2.2 Timing

Figure A.6 shows the data acquisition system timing. Data acquisition is initiated by the device command line from pin number 17

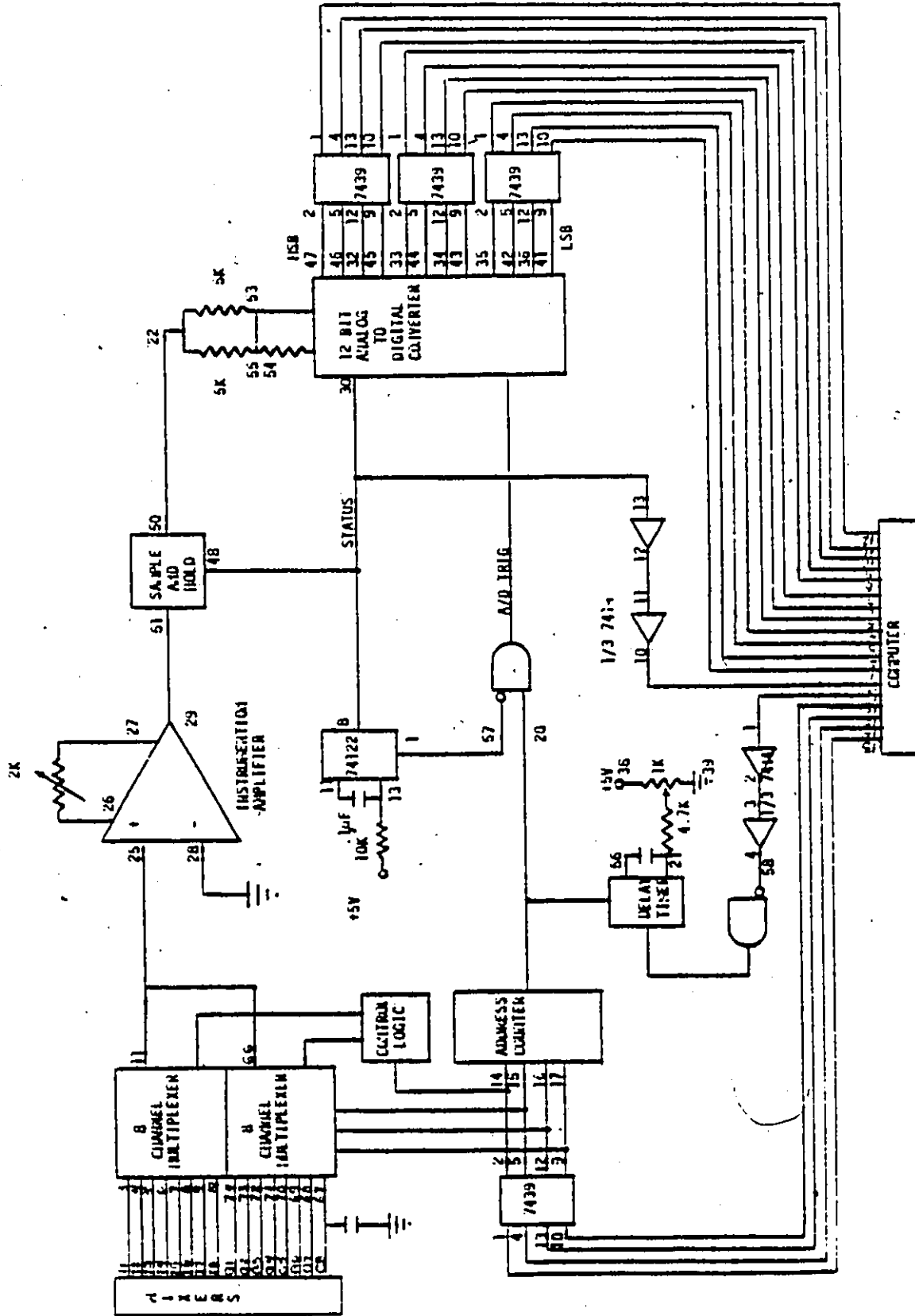


Figure A.5 Data Acquisition System circuit diagram.



of the HP1000 computer. This signal makes a high to low transition, at the STROBE pin 58 of the SDM 853. This transition first causes the address counter to be incremented by one, selecting the next multiplexer channel. It also initializes the delay timer, producing a falling edge at DELAY OUT (18), remaining low for 31 usec (set by means of the RC network between pins 21 and 56). This time-delay is sufficient to allow for the instrumentation amplifier and sample and hold to settle.

The rising edge of DELAY OUT (18), applied to A/D TRIG (20) and accompanied by a low level at A/D TRIG (57), triggers the A/D to converter. This causes the A/D STATUS line (30) to go high. The high level on this status line causes the sample and hold previously tracking the instrumentation amplifier to hold its output.

Twelve-bit conversion takes place over the 24 usec that the status line is high. A falling edge triggers a 476 usec monostable high and is also sent to pin 18 of the HP 1000 computer flagging valid data. The monostable's high output applied to A/D TRIG (57) presents further data conversion for the 476 usec time period. This delay is used to allow the computer time to transfer data.

When the monostable's level falls low, this causes the STATUS LINE to again go high, holding the sample and hold again. This process continues until the computer has received a software specified number of data samples. At this point, a device command once again increments the address counter and starts the process all over. This is continued until the specified number of data samples is received from all of the 16 channels.

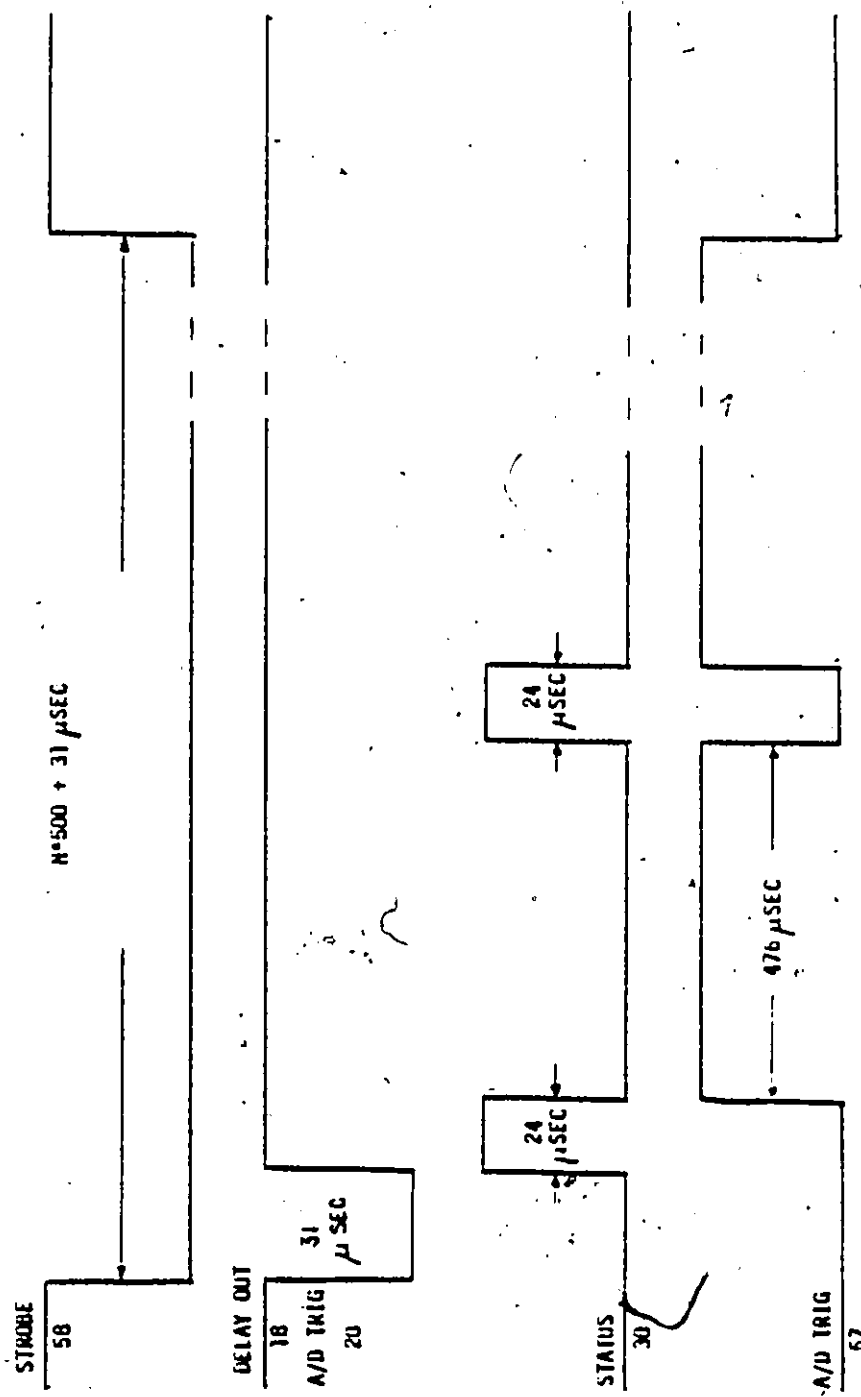


Figure A.5 Data Acquisition System timing diagram.

### A.2.3 Grounding

The SDM853 is contained within a shielded package. This, along with its support hardware, is contained within a shielded box. The box is securely mounted to the wall of the anechoic chamber providing a system ground. All power supplies, microwave and computer ground connect to a common point on the chamber wall thus completing the grounding requirements.

### A.3.1 Receiver Position Control System

The function of this system is to move the receiver in elevation to a specified angle. Figure A.7 is a block diagram showing the major component of this system.

The elevation angle of the Scientific Atlantic series 5300 Azimuth/elevation Fractional-Horsepower Positioner is sent in the form of synchro signals via the synchro transmitter to the scientific-Atlanta series 4422 indicator units. The three synchro signals S1, S2, S3 are converted in the trig module to sines and cosines of the elevation angle. These signals along with the 60 Hz reference signal are passed on to the converter module. This module compares the analog coded synchro information with the digital coded desired angle and generates the error signal proportional to the difference.

This error signal is used first of all to control the forward and reverse direction of the motor depending on its sign. Secondly, the motor's angular velocity is controlled proportionally with the magnitude of this error signal. When the desired angle has been reached, the

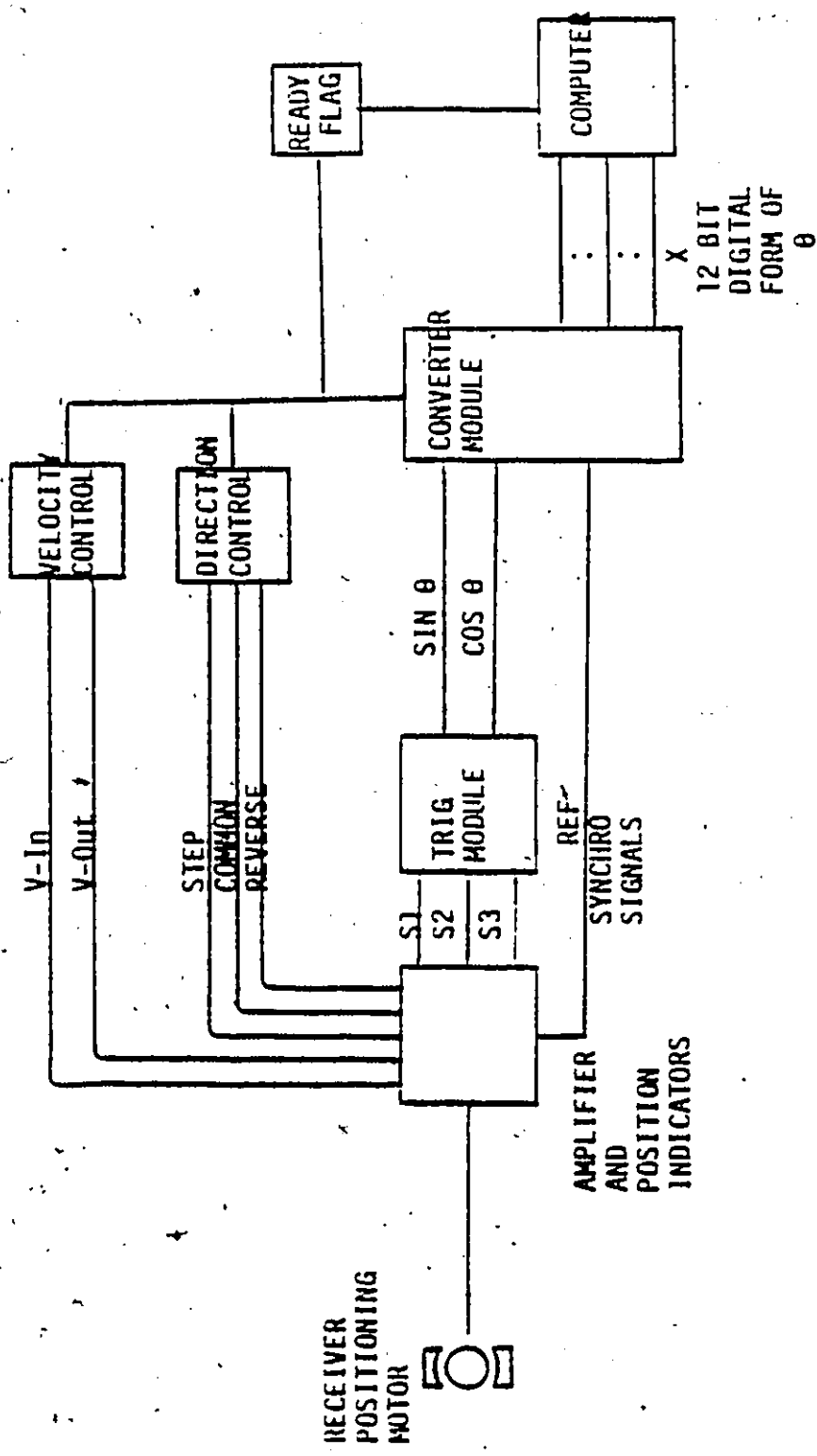


Figure A.7 Block diagram of Receiver Position Control system.

forward and reverse relays are opened (see switching) and the motor comes to a halt. At this point, a flag is sent to the computer, signaling completion.

Figure A.8 shows the complete system layout.

### A.3.2 Switching Circuits

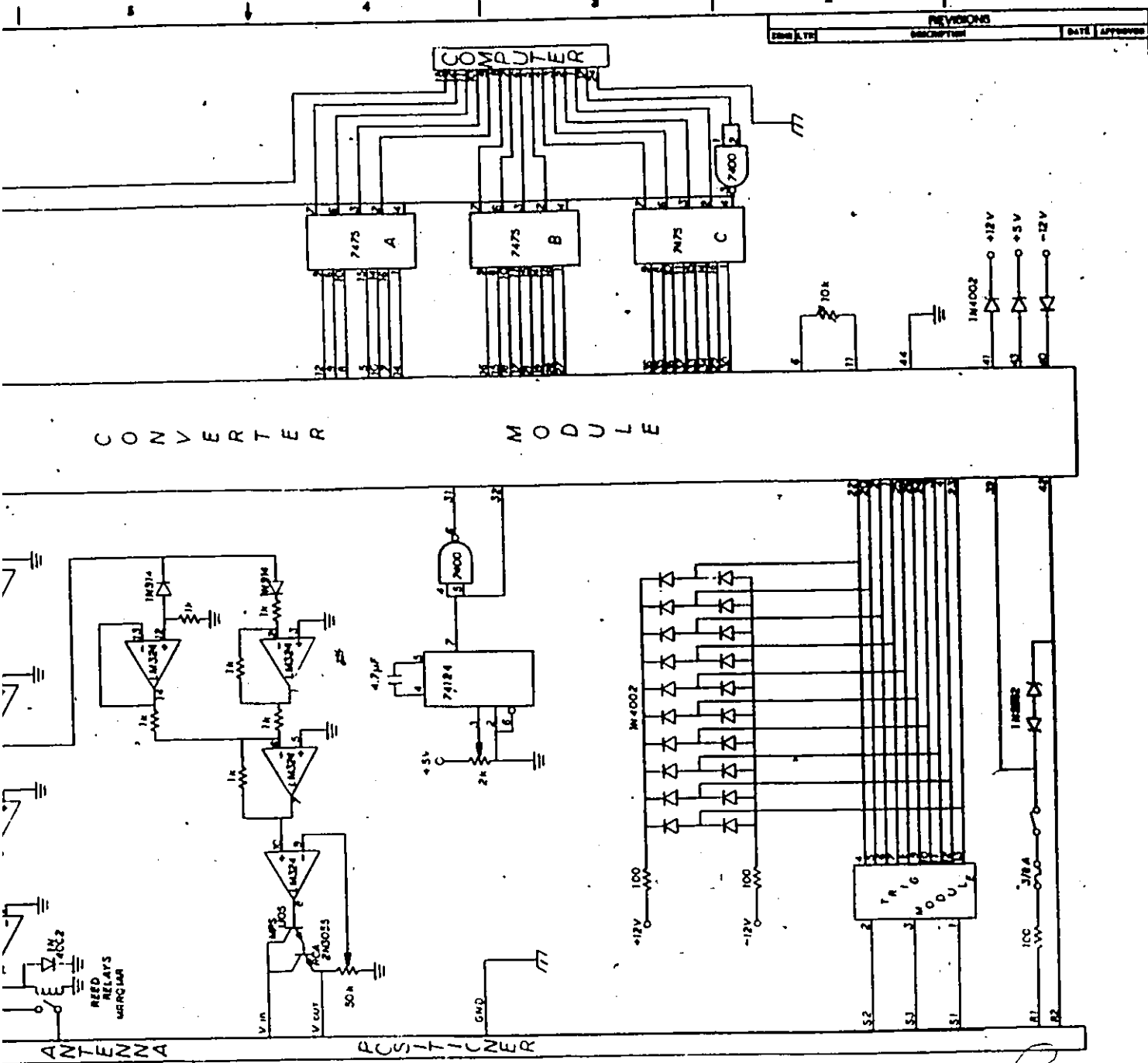
The scientific Atlanta positioner comes equipped with a port (J2) giving the user access to the motor supply voltages. These lines are STEP, REVERSE, COMMON and are used to control the positioner when the selection dial on the front panel is turned to PCP.

Joining the STEP and common causes the positioner to move in the forward direction at a speed governed by the variac supply voltage (controllable at the front panel). If, in addition, the common and reverse are joined, the positioner will move in the reverse direction. The positioner will not move if the step and common lines are not joined regardless of the reverse state.

The circuit of Figure A.9 is used to control the above functions. An error signal from the converter module passes through three filter stages (op amps 1, 2, 3) to clean up noise. This negative error signal is then compared to a small reference signal  $\delta \approx 10$  mV at the output of op amp 4 (an isolator). The next stage op amp #5 is a unity-gain inverting amplifier giving us a negative reference.

Ideally, we would want the motor to stop when the difference error between the desired angle and the actual angle was zero. It is, however, not possible to stop the motor "exactly" at zero error. This





A.8 Complete circuit diagram for Receiver Position Control system.

DATE: 05257

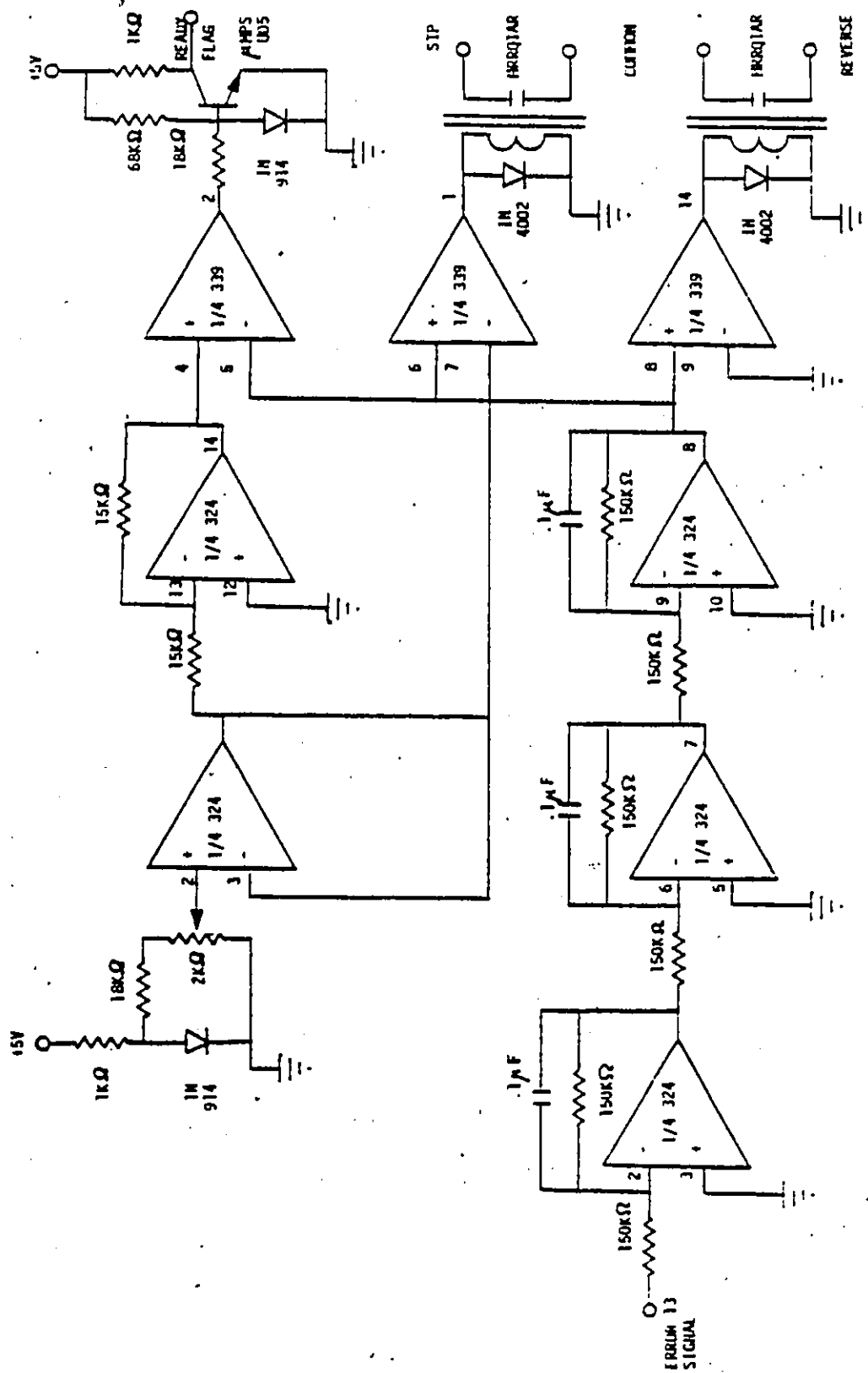


Figure A.9. Circuit diagram for relay switching.



is the reason for the small reference  $\delta$ , i.e. if the error voltage is within  $\delta$  of zero ( $-\delta < \epsilon < \delta$ ) the positioner will stop.

This means that the MRRQIAR reed relay (normally open) will be switched off whenever  $-\delta < \epsilon < \delta$ . This is done by means of voltage comparators 1 and 2. When the error voltage  $-\epsilon$  at terminal #5 of voltage comparator 1 is less than  $-\delta$  ( $|\epsilon| > +\delta$ ), the output (pin #2) is saturated to the negative supply voltage of  $-12$  V. The IN4002 diode will be reversed-biased and therefore off; this allows the output at pin 2 to maintain a 12 volt drop across the 1000  $\Omega$  relay coil causing it to turn on (close), connecting STEP and COMMON. When  $-\epsilon > -\delta$  ( $|\epsilon| < \delta$ ) (pin #2), the output is  $+12$  V. This  $+12$  V is held below the necessary 12 V coil voltage by the IN4002 diode thus preventing the relay from closing. Similarly, voltage comparator #2 compares  $-\epsilon$  against  $\delta$  if  $-\epsilon > \delta$  ( $+\epsilon < -\delta$ ) the relay will be closed (turned on).

Voltage comparator 3 is exactly the same as 2 and is used to close a relay joining REVERSE and COMMON to change the positioner's direction.

### A.3.3 Speed Control Circuit

The circuit of Figure A.10 is used to slow the positioner down as it approaches the desired elevation angle. The first two op amps are configured to give the absolute value of the error signal  $\epsilon$ . If  $\epsilon < 0$ , then diode #1 is turned on and the output of op amp #1 is  $-\epsilon$ . Diode number 2 is off and op amp #2, seeing a virtual ground at its input, has a zero voltage output. If  $\epsilon > 0$ , then diode #1 is off and op amp #1 has zero output. Diode #2 will be turned on, op amp number 2, being a unity

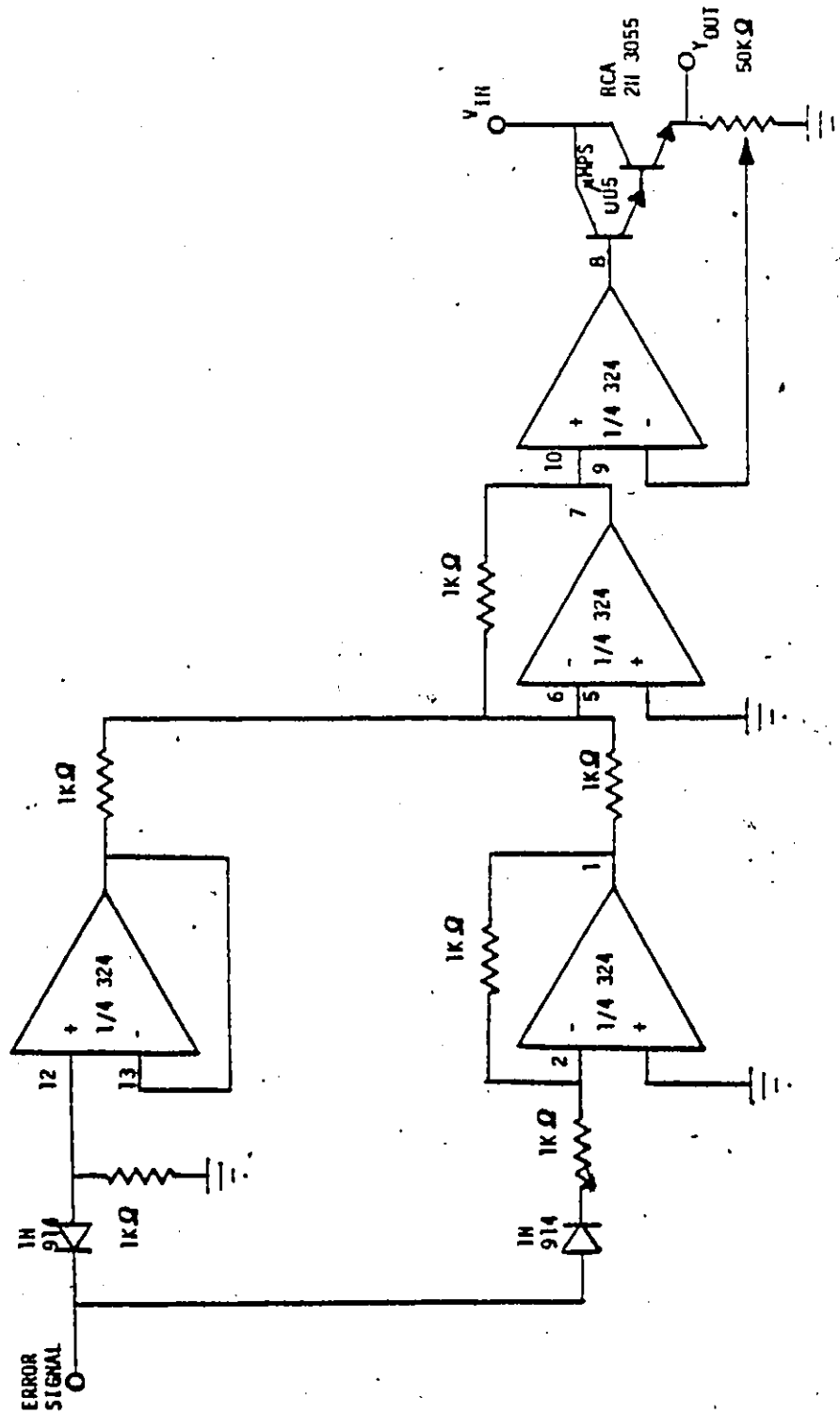


Figure A.10 Circuit diagram for speed control.

gain inverting amplifier, gives  $-\epsilon$  at its output.

The next stage op amp #3 is a unity gain inverting summer. It sums the outputs of op amps 1 and 2 (which is always  $-\epsilon$ ) then inverts the sum, resulting in a level of  $|\epsilon|$  at its output.

The following stage is a voltage regulator, which in this case, is an op amp. The Darlington coupled transistor pair form the emitter follower output stage of this new op amp. The resistor divider feedback provides the necessary gain. This circuit is capable of supplying over 8 amps of current to the positioner motor. The input voltage  $V_{in}$  is the source voltage used to drive the positioner motor. Its value can be set by means of the variac transformer in the position unit (this value should not exceed 20 V). The voltage drop from  $V_{in}$  to  $V_{out}$  will be proportional to  $|\epsilon|$ , such that  $V_{in}$  is equal to the stall Voltage of the motor (10 V) when  $|\epsilon| = 0$ .

#### A.3.4 Transmitter Positioning Device

The mechanism illustrated in figure A.11 is used to move two horns symmetrically in elevation about its mid-point. A special design feature is that the main beams of the horns are always focused on the centre of the receiving array. This has been accomplished by means of two screws. The main or lead screw and the tilt screw motor away or toward the mechanisms centre at different rates. This is a result of the difference in gear ratios and the number of threads per inch on each screw. The tilt screws moving at a faster rate than the lead screw causes the horns to tilt inward as the distance from the centre increases. Blue prints and parts list prepared by Peter Young of

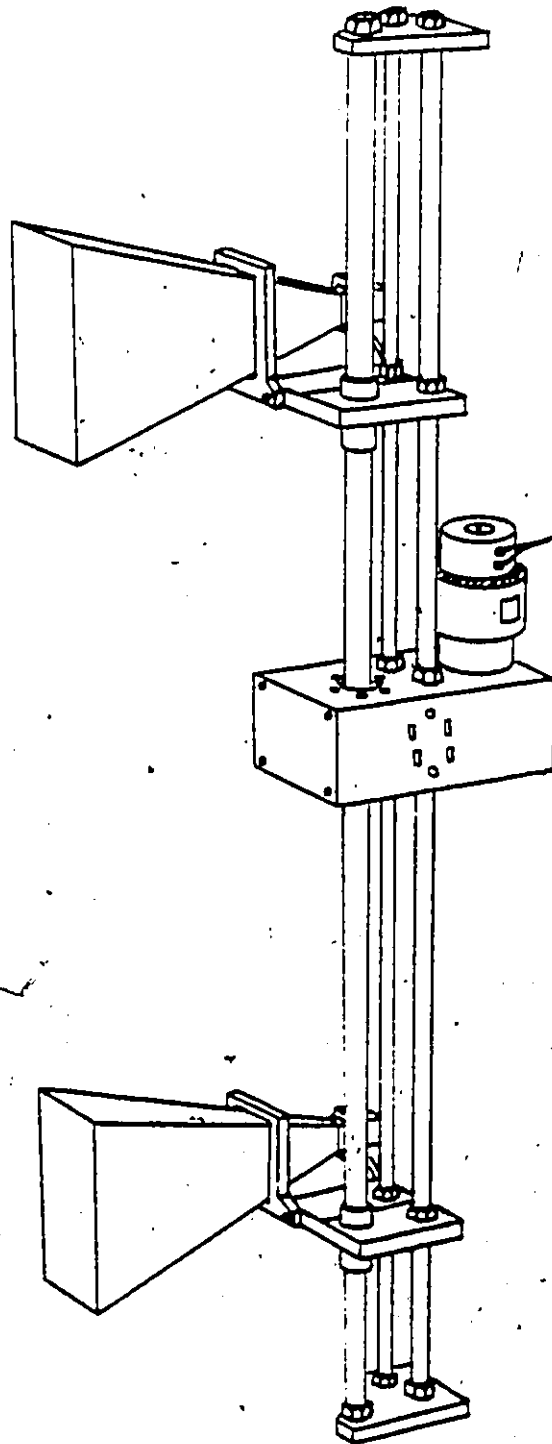


Figure A.11 Sketch of Transmitter Positioning Mechanism.

Mechanical Engineering are provided in figures A.12, A.13 and Tables A.3.4.1, A.3.4.2.

A handwritten signature or set of initials, possibly 'L.R.', written in dark ink on the right side of the page.

Figure A.12 Drive housing for Positioning Mechanism.

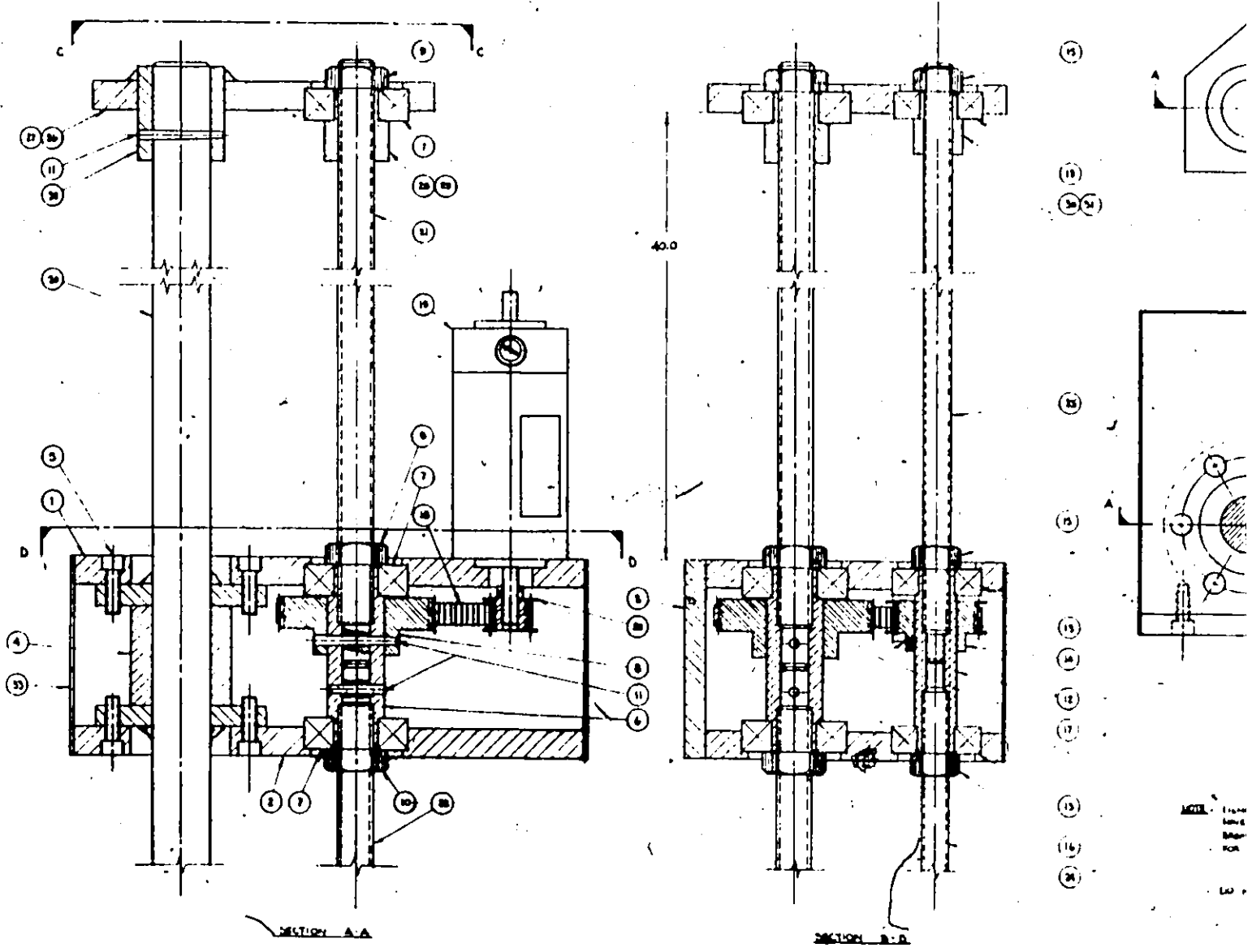
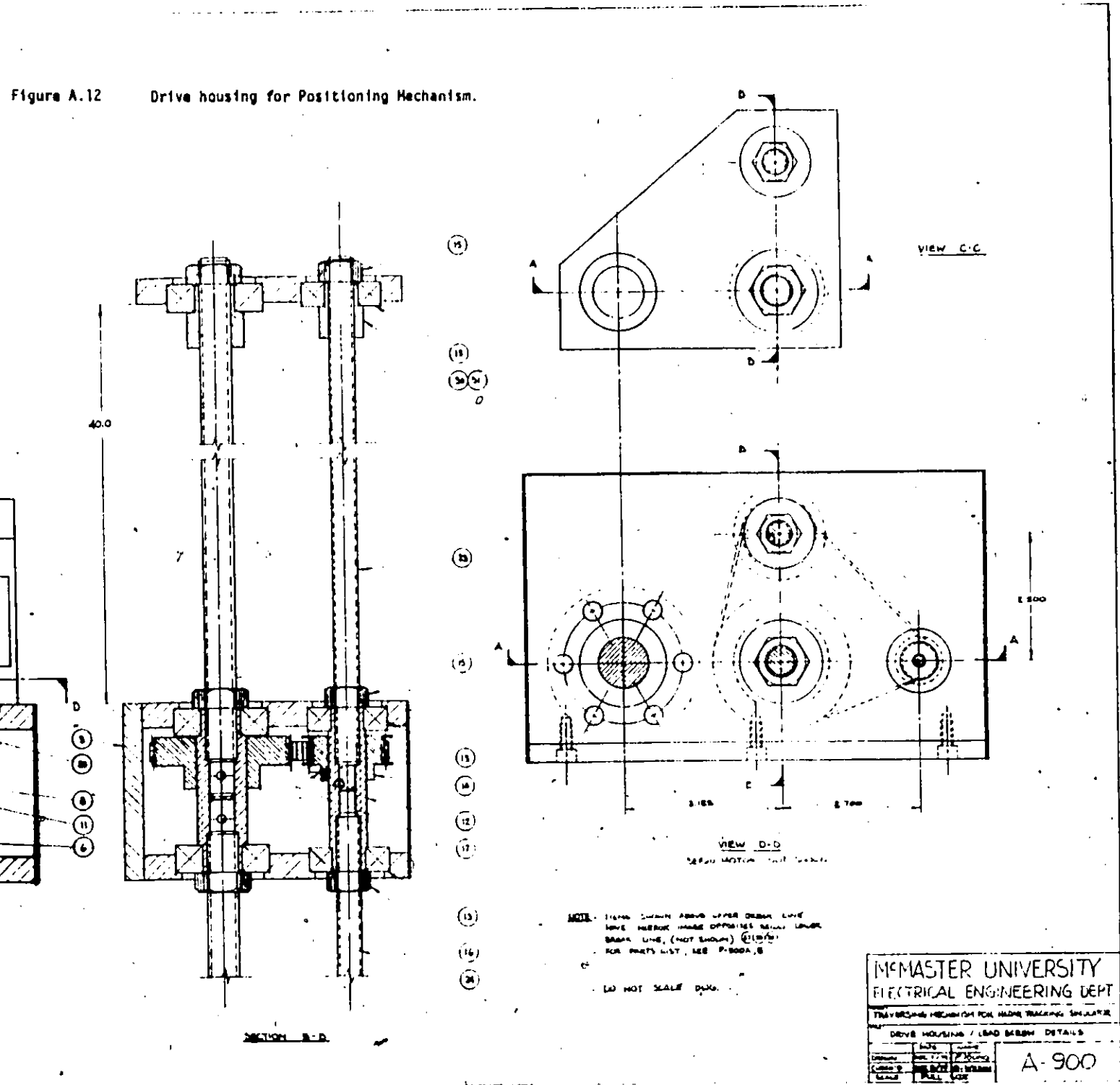


Figure A.12 Drive housing for Positioning Mechanism.



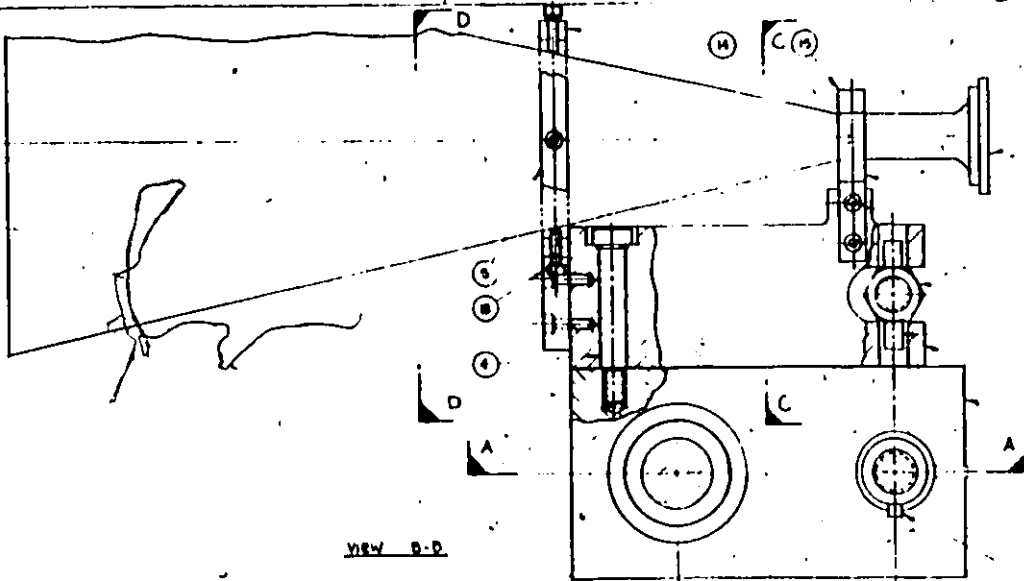
NOTE: DIMS SHOWN ABOVE UPPER DECK LINE  
 HAVE HORIZ IMAGE OPPOSITE SMALL LEVER  
 BARR LINE, (NOT SHOWN) (11/10/71)  
 FOR PARTS LIST, SEE P-300A, B

DO NOT SCALE DRAWING

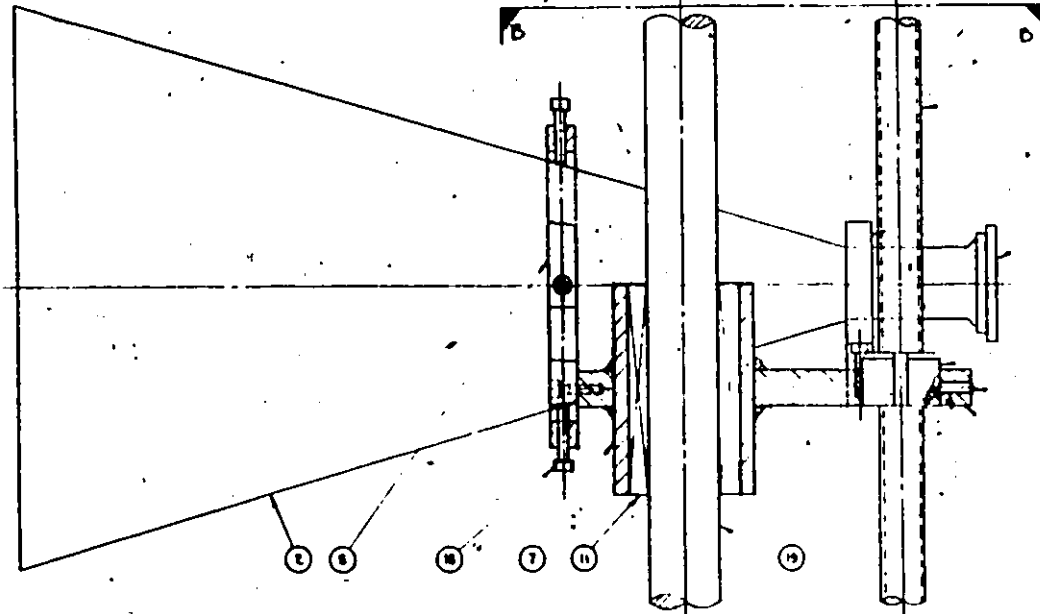
MCMMASTER UNIVERSITY	
ELECTRICAL ENGINEERING DEPT	
TRAVELING MECHANISM FOR MAGE TRACKING SIGNALER	
DRIVE HOUSING / LEAD SCREW DETAILS	
DATE	11/10/71
DESIGNED BY	W. J. WILSON
CHECKED BY	W. J. WILSON
SCALE	AS SHOWN
A-900	

2 of 2

Figure A.13



VIEW B-D



SECTION A-A

- (1)
- (2)
- (3)
- (4)
- (5)
- (6)
- (7)
- (8)
- (9)
- (10)
- (11)
- (12)
- (13)
- (14)
- (15)
- (16)
- (17)
- (18)
- (19)
- (20)

FOR MOUNTING ON  
S. S. RING  
MATERIAL: S.S.

FOR MOUNTING ON  
S. S. RING  
MATERIAL: S.S.

NOTE: UPPER ASSEMBLY  
A MIRROR IS  
BE MADE FOR  
FOR PARTS U

DO NOT SCALE

for





Table A.3.4.1

## PARTS FOR TRAVERSING A-900 MECHANISM

## Drive Housing:

Item	Name	Mat'l	Req'd	Description
1	Upper Plate	CRS	1	
2	Lower Plate	CRS	1	
3	Side Plate	CRS	1	
4	Guide Bar Support Ass'y		1	
5	Guide Bar Support Screws		12	1/4*20 UNC x 3/4" socketcap
6	Drive Screw Housing	CRS	1	
7	Drive Screw Bearing		4	SKF 6204-2RS or equivalent
8	Drive Screw Pulley		1	Dodge 44xLo37 (or equiv)
9	Upper nut		2	5/8-11-UNC-RH-2B JAM
10	Lower Nut		2	5/8-11-UNC-LH-2B JAM
11	Taper Pin		4	#4
12	Tilt Screw Housing	CRS	1	
13	Tilt Screw Bearing		4	SKF 6203-2RS or equivalent
14	Tilt Screw Pulley		1	Dodge 24xL037 (3/4 bore)
15	Upper Nut		2	1/2-20-UNF-RH-2B
16	Lower Nut		2	1/2-20-UNF-LH-2B
17	Set Screw		1	#6x1/2" socket hd.
18	Belt		1	Dodge 140xL x 3/8 wide

Table A.3.4.1

Drive Housing:					
Item	Name	Mat'l	Req'd	Description	
19	DC Servo Motor		1	ECC 586/91 or equiv. + 586 BPC	
20	Guide Bar		1	1" dia superior shaft ~ 78" long	
21	Upper Drive Screw		1	5/8-11-UNC-RH-3A	
22	Lower Drive Screw		1	5/8-11-UNC-LH-3A	
23	Upper Tilt Screw		1	1/2-20-NF-RH-3A	
24	Lower Tilt Screw		1	1/2-20-UNF-LH-3A	
25	Motor Pulley		1	11xL037 Dodge	
26	Upper End Plate	CRS	1		
27	Lower End Plate	CRS	1	Now Shown	
28	Upper Drive Bearing Retainer	CRS	1		
29	Lower Drive Bearing Retainer	CRS	1	Now Shown	
30	Upper Tilt Bearing Retainer	CRS	1	Not Shown	
31	Lower Tilt Bearing Retainer	CRS	1	Now Shown	
32	Guide Bar End Support	CRS	2		
33	Cover		1		

Table A.3.4.2

PARTS LIST FOR A901  
CARRIAGE DESIGN FOR TRACKING SIMULATOR

Item	Name	Mat'l	Req'd	Description
1	Carriage Plate	CRS	2	
2	Horn		2	12-8.2 SA
3	Tilt Plate	CRS	2	
4	Pivot Bolt		2	1/2" x 1.750 std. shoulder bolt
5	Front Horn Mount	CRS	2	
6	Rear Horn Mount	CRS	2	
7	Bearing Holder	CRS	2	
8	Drive Nut	Bronze	2	
9	Tilt Nut	Bronze	2	
10	Tilt Nut Pivots	CRS	4	
11	Bearing		2	
12	Nut Key		2	
13	Nut Set Screw		2	#8-32 x 1/2"
14	Front Horn Mount Cap		2	
15	Rear Horn Mount Cap		2	
16	Set Screw		2	
17	Horn Mount Assembly Screws		16	6-32 x 3/4 socket hd.
18	Horn Centering Screws		8	6-32 x 3/4 socket hd.
19	Guide Bar		1	1" superior shaft
20	Drive Screw (upper shown)		1	5/8-18 UNF CL 3A

APPENDIX B  
SYSTEM SOFTWARE



```
WRITE(1,3)
CALL POSIT(1)

DO 1 I=1,NAGP3

IF(I.LE.3)CALL MESS(I)
IF(I.GT.3)CALL POSIT(I)
CALL DATA(I)
```

```
1 CONTINUE
ENDFILE 10
```

```
2 FORMAT("FROM HOW MANY ANGLES IS DATA TO BE OBTAINED")
3 FORMAT("THE DEPRESSION-ANGLE SHOULD BE 0.0 DEGREES TO ALLOW FOR C
+ALIBRATION"//)
4 FORMAT(I4)
```

```
STOP
END
```

```
SUBROUTINE MESS(IMESS)
```

```
C SUBROUTINE MESS PROVIDES PROMPTS.
```

```
DIMENSION IPHASE(3)  
DATA IPHASE/180,90,0/
```

```
WRITE(1,1)IPHASE(IMESS)  
CALL BELL
```

```
1 FORMAT("SET THE TRANSMITTER PHASE AT ",I3," DEGREES")
```

```
RETURN  
END
```



## SUBROUTINE DATA(ICOUNT)

C \* DATA \* IS USED TO TRANSFER DATA FROM THE DATA ACQUISITION  
C SYSTEM (LOCATED IN ROOM 215), TO A FILE ON CARTRIDGE GW ACCESSED  
C THROUGH LU#10. THE NUMBER OF SAMPLES ACQUIRED FROM EACH  
C CHANNEL IS ALSO RECORDED ON LU#10. ON LU#10.

C >>>>> PARAMETERS <<<<<<

C ICODE : 1=READ FROM INPUT DEVICE.  
C LU : LOGICAL UNIT NUMBER OF 16-BIT INPUT PORT.  
C IBUFR : BUFFER WHERE INPUT DATA IS STORED IN MEMORY.  
C IBUPL : NUMBER OF WORDS TO BE READ FROM INPUT DEVICE.  
C IMODE : 1=INTERRUPT MODE, ONE DEVICE COMMAND SENT,  
C DEVICE FLAG INDICATES VALID DATA.

C <SEE HP 93552A GENERAL PURPOSE RTE DRIVER DVS72 MANUAL>

DIMENSION IBUFR(1000)

IF(ICOUNT.NE.1)GOTO 1  
WRITE(1,4)  
READ(1,\*)IBUPL  
WRITE(10,3)IBUPL  
ICODE=1  
LU=70B  
IMODE=1

1 DO 2 I=1,16  
CALL EXEC(ICODE,LU,IBUFR,IBUPL,IMODE)  
WRITE(10,3)(IBUFR(K),K=1,IBUPL)  
2 CONTINUE  
3 FORMAT(16)  
4 FORMAT("ENTER THE NUMBER OF SAMPLES REQUIRED")

RETURN  
END

## SUBROUTINE POSIT(ICOUNT)

C THIS SUBROUTINE IS USED TO POSITION THE RECEIVER TO  
 C THE APPROPRIATE ANGLE DETERMINED BY THE USER.  
 C THIS ANGLE IS WRITTEN ON LU#10 FOR FUTURE REFERENCE.

C >>>>> PARAMETERS <<<<<<

C ICODE : 2=WRITE TO POSITION CONTROL DEVICE.  
 C LU : LOGICAL UNIT NUMBER OF 16-BIT OUTPUT PORT.  
 C IWORD : WORD CONTAINING ANGULAR POSITION.  
 C NWORD : NUMBER OF WORD TO BE WRITEN.  
 C IMODE : 0=SEND DEVICE COMMAND, WAIT FOR DEVICE FLAG INTERRUPT.  
 C ICNTRL: SPECIFY RECEIVER OR TRANSMITTER CONTROL.  
 C ANGLE : ANGLE TO WHICH POSITIONER IS TO BE LOCATED.

IF(ICOUNT.NE.1)GOTO 1  
 WRITE(1,3)  
 READ(1,\*)ICNTRL  
 ICODE=2  
 LU=71B  
 NWORD=1  
 IMODE=0  
 1 WRITE(1,4)  
 READ(1,\*)ANGLE  
 WRITE(10,5)ANGLE  
 IF(ICNTRL.EQ.2)GOTO 2  
 IWORD=INT(ANGLE\*409.6)  
 CALL EXEC(ICODE,LU,IWORD,NWORD,IMODE)

RETURN

2 CALL BELL

3 FORMAT("INPUT : 1 / RECEIVER POSITION CONTROL"/9X"2 / TRANSMITTE  
 +R POSITION CONTROL")

4 FORMAT("WHAT IS THE DEPRESSION ANGLE DESIRED ?")

5 FORMAT(F10.6)

RETURN  
 END

## SUBROUTINE BELL

C SUBROUTINE BELL IS USE TO HALT THE PROGRAM TO  
C ALLOW TIME FOR THE USER TO SET UP THE REQUIRED HARDWARE.  
C RETURN TO PROGRAM IS POSSIBLE WITH USE OF THE "BR" COMMAND  
C WHILE IN BREAK MODE.

C >>>>> PARAMETERS <<<<<<

C IBELL : CONTROL "G" ASCII CHARACTER FOR BELL  
C IPBRK : SET TO 1 IF THE "BR" COMMAND IS USED IN BREAK MODE  
C EXEC : THIS EXEC PROVIDES A TIME DELAY OF 1 SEC

DATA IBELL/3400B/

1 WRITE(1,2)IBELL  
CALL EXEC(12,0,2,0,-1)  
IF(IPBRK(IDUM).EQ.0)GOTO 1  
2 FORMAT(A1)

RETURN  
END

FTN4,L  
SEMA(XYZ,0)  
PROGRAM AJUST

```
C      *
C      *
C      *
C      *      B.2.1      PROGRAM AJUST      *
C      *
C      *
C      *
C      *
```

```
C      This program is used to compensate for channel
C      nonuniformity. The first three data samples blocks of
C      "DVS72" are used to find the channel amplitudes, phases,
C      and offsets. These are then used to transform the
C      array into one with uniform channel characteristics.
C      This is not to say that the array characteristics will
C      be altered, all the information pertaining to the array
C      itself will be preserved. Each element's gain pattern
C      will not be changed by these transformations, and the
C      group pattern being of main interest will of course be
C      preserved in the relative phase between the array
C      elements.
```

```
C      Subroutine "INPUT" reads the prerecorded data
C      from LU#10. LU#10 is the data file "#DATA" into which
C      program "DVS72" wrote the array data. This data is
C      read in "INPUT" with a READ(10,format#). It is thus
C      necessary to spool LU#10 as a (read only) file, this is
C      done by the filemanager command :SL,10,#DATA:GW:37.
C      The number of angles from which data was
C      obtained and the number of samples per channel are
C      recorded on L 10 allowing the appropriate number of
C      data samples to be transferred. Each data word
C      consists of four address and twelve signal bits.
C      Subroutine "INPUT" performs the task of separating the
C      two words.
```

```
C      Subroutines "OPSET", "PHASE", and "AMPLI"
C      calculate the individual channel offset, phases and
C      amplitudes. This information is then passed on to
C      subroutine "NORM" which normalizes the data compen-
C      sating for variations in gain, phase shift, and DC
C      offset.
```

```
C      The next subroutine "SHIFT" shifts the phase of
C      all the channels by the phase of the bottom array
C      element. This is done so that all the channels are
C      phase relative to channel eight. In this way it
C      appears as if the array was rotating about a point
C      centered in that element. Future programing (in
C      program shape) will then be able to provide phase
C      shifts which correspond to the path length differences
C      and surface reflection characteristics, independent of
C      path length differences from within the chamber.
C      The resultant calibrated data is written on file
C      #AJUST accessed through LU#11. This file has been
C      spooled as a write only file by the file manager
C      command SL,11,#AJUST:GW:GW.WR.
```

```

COMMON/XYZ/A(16,1000)
COMMON/SPAC/ANORM(16)
COMMON//K,NSMPLS,AMEAN(16),OFSET(16),PHAZE(16),AMP(16)
COMMON//ANGLE/ANGLE

```

```

C >>>>> PARAMETERS <<<<<<
C NAGLS : NUMBER OF ANGLES FROM WHICH DATA IS AVAIVABLE
C ANGLE : SPECIFIC ANGLE TO WHICH PRESENT DATA CORRESPONDS
C NSMPLS : NUMBER OF DATA SAMPLES AVAILABLE FROM THESE ANGLES
C K : FLAG USED IN CALIBRATION STEPS.

```

```

REWIND 11
REWIND 10
REWIND 8
READ(10,2)NAGLS
READ(10,3)ANGLE
WRITE(8,5)ANGLE
READ(10,4)NSMPLS
IF(ANGLE.NE.0.0)PAUSE
K=1
CALL INPUT
CALL OFFST
CALL INPUT
CALL PHASE
CALL AMPLI
K=2
CALL INPUT
CALL OFFST
CALL PHASE
CALL AMPLI
CALL NORM
CALL SHIF

DO 1 K2=1,NAGLS

WRITE(1,6)K2
READ(10,3)ANGLE
WRITE(8,5)ANGLE
CALL INPUT
CALL NORM
CALL SHIF

1 CONTINUE

WRITE(11,7)666.

ENDFILE 11
ENDFILE 8

2 FORMAT(I4)
3 FORMAT(F10.6)
4 FORMAT(I6)

```

```
5   FORMAT("1 THE FOLLOWING INFORMATION CORRESPONDS TO A DEPRESSION AN  
+GLE OF "F5.3" DEGREES"///)  
6   FORMAT("THE DATA CORRESPONDING TO DEPRESSION, ANGLE # "I3  
+ " HAS JUST BEEN WRITTEN ON TAPE")  
7   FORMAT(G13.6)
```

```
STOP  
END
```

## SUBROUTINE PHASE

C This subroutine computes the phase of each  
C channel in the following manner.

C STEP #1: When the first call is made to phase  
C the transmitter phase is adjusted to 90 Degrees.  
C The average value of all sample for each channel  
C is stored by "INPUT" in vector AMEAN. When this  
C first call is made to "PHASE" this value is stored  
C in the first column of array FAZE.

C STEP #2: In the second call to "PHASE" AMEAN  
C contains the mean values of data corresponding to  
C a transmitter phase of 0 Degrees and is stored in  
C the second column of FAZE.

C STEP #3: Assuming the signals obtained to be  
C of the form  $AG(\theta)\cos(\theta) + OPSET$ . Then the  
C signal of Step #1 is  $AG(0)\cos(\theta - 90\text{Degrees}) +$   
C  $OPSET$ . Where A is the signal amplitude, G(theta)  
C is the element pattern for theta = 0Degrees and  
C OPSET the DC offset of a given channel.

C Subtracting the offset (calculated in  
C subroutine "OPSET") from each of Steps one and two,  
C we have

$$FAZE(I,1) = AG(0)\cos(\theta - 90) = AG(0)\sin(\theta)$$

$$FAZE(I,2) = AG(0)\cos(\theta)$$

C The ratio of FAZE(I,1) to FAZE(I,2) results  
C in the cancellation of the AG(0) term, giving us  
C  $\tan(\theta)$  from which  $\theta$  is obtained.

DIMENSION FAZE(16,2)  
COMMON//K,NSMPLS,AMEAN(16),OPSET(16),PHAZE(16)

TWOPI=8.0\*ATAN(1.0)

DO 1 I1=1,16

FAZE(I1,K)=AMEAN(I1)

1 CONTINUE

IF(K.EQ.1)RETURN

DO 2 I2=1,16

FAZE(I2,1)=FAZE(I2,1) - OPSET(I2)

FAZE(I2,2)=FAZE(I2,2) - OPSET(I2)

PHAZE(I2)=ATAN2(FAZE(I2,1),FAZE(I2,2))

IF(PHAZE(I2).LT.0.0) PHAZE(I2)=PHAZE(I2)+TWOPI

2 CONTINUE

RETURN

END

## SUBROUTINE AMPLI

```

C      The amplitude of each channel is calculated
C      assuming the signal (at transmitter phase set to
C      zero) to be of the form below.
C      X(0) = A*G(theta)cos(thi) + OPSET.
C      And the signal for transmitter phase of 90 degrees
C      to be of this form.
C      X(90) = A*G(theta)sin(thi) + OPSET
C      The signal amplitude is then calculated by
C      subtracting the offsets and summing the squares.
C
C      AMP = [(X(90)-OPSET)**2 + (X(0)-OPSET)**2]1/2
C      AMP = A*G(theta)
C
C      >>>>> PARAMETERS <<<<<<
C
C      AMP : VECTOR OF THE CALCULATED CHANNEL GAINS.
C      PHAZ : PHASE EXPRESSED IN DEGREES.
C
DIMENSION AMPTE(16,2)
COMMON//K,NSMPLS,AMEAN(16),OPSET(16),PHAZE(16),AMP(16)

RADEG=45./ATAN(1.0)
DO 1 I1=1,16
AMPTE(I1,K)=AMEAN(I1)
1 CONTINUE
IF(K.EQ.1)RETURN
WRITE(8,3)
DO 2 I2=1,16
AMPTE(I2,1)=AMPTE(I2,1) - OPSET(I2)
AMPTE(I2,2)=AMPTE(I2,2) - OPSET(I2)
AMP(I2)=SQRT(AMPTE(I2,1)**2 + AMPTE(I2,2)**2)
PHAZ=PHAZE(I2)*RADEG
WRITE(8,4) I2,AMP(I2),PHAZ,OPSET(I2)
2 CONTINUE
3 FORMAT(3X"CHANNEL #",7X,"AMPLITUDE",13X,"PHASE",15X,"OFFSET",/)
4 FORMAT(5X,I2,5(10X,F10.5))

RETURN
END

```



## SUBROUTINE BELL

C           This subroutine is used as an alarm to  
C indicate that some error has occurred in the data  
C handling. The alarm will be accompanied by an  
C appropriate message indicating the nature of the  
C error.

1           DATA IBELL/3400B/  
2           WRITE(1,2) IBELL  
            FORMAT(A1)  
            CALL EXEC(12,0,2,0,-1)  
            IF(IFBRK(IDUM).EQ.0)GOTO1

            RETURN  
            END

SEMA(XYZ,0)  
SUBROUTINE INPUT

C           Reading from LU#10, subroutine "INPUT" acquires  
C the original data obtained from the system hardware.  
C The data words read (IDATA) are 16 bit integers.  
C The four most significant bits contain the address  
C from which the data word (lower twelve bits) was  
C obtained. The 50 ohm line drivers of the data  
C acquisition system gives a ones complement of the  
C actual address and data words. For this reason the  
C the first step in decoding the data is to subtract  
C it from 177777B octal undoing the inverting effect  
C giving IDA.  
C           The address (IADR) is then obtained by masking  
C of the most significant four bits (LOGICAL AND with  
C 170000B), then shifting right twelve bits by dividing  
C by  $2^{12}=4096$ . If an error is detected in the address  
C word, an error message will be printed on the CRT  
C and subroutine "BELL" will be called. A logical  
C AND of the IDA with 007777B masks off the eleven bit  
C DATA magnitude word (IDA). The data word is in two's  
C complement form, with the sign bit in the 12th bit  
C place. The HP 1000 is a 16 bit computer with its  
C sign bit in the 16th location. Bit twelve is masked  
C to find the sign bit. If this bit is one, then bits  
C 12-16 of the computer words must be one so that the  
C sign and magnitude of the data word are correct.  
C           This number is then divided by 4096 to give a  
C number in the range of +/-1. A maximum, mean,  
C minimum and standard deviation are then calculated  
C for each channel.

COMMON/XYZ/A(16,1000)  
COMMON //K,NSMPLS,AHEAN(16)  
DOUBLE PRECISION AHESS(4)  
DIMENSION AMINI(16),AMAXI(16),SD(16)  
DATA AMESS/5HOMAXI,5H MEAN,5H MINI,5H SD /

DO 2 J=1,16

DO 2 I=1,NSMPLS

READ(10,10) IDATA  
IDAT=177777B-IDATA  
IADR=(IDAT.AND.170000B)/4096  
IF(IADR.LT.0) IADR=IADR+16  
IF(I.EQ.1) NEXT=IADR  
IF(IADR.EQ.NEXT) GOTO 1  
WRITE(1,9)  
CALL BELL  
1 IDA=(IDAT.AND.007777B)  
ISIGN=(IDAT.AND.004000B)  
IF(ISIGN.EQ.004000B) IDA= IDA + 170000B

```
A(IADR+1,I)= FLOAT(IDA)*.001221
2  CONTINUE
DO 7 I1=1,16
AMINI(I1)=3.
AMAXI(I1)=-3.
AMEAN(I1)=0.
SD(I1)=0.
DO 5 I2=1,NSMPLS
IF(A(I1,I2).LT.AMINI(I1))AMINI(I1)=A(I1,I2)
IF(A(I1,I2).GT.AMAXI(I1))AMAXI(I1)=A(I1,I2)
AMEAN(I1)=A(I1,I2)+AMEAN(I1)
5  CONTINUE
PLOTN=FLOAT(NSMPLS)
AMEAN(I1)=AMEAN(I1)/PLOTN
DO 6 I3=1,NSMPLS
SD(I1)=(A(I1,I3)-AMEAN(I1))**2 + SD(I1)
6  CONTINUE
SD(I1)=SQRT(SD(I1)/(PLOTN-1.0))
7  CONTINUE
WRITE(8,8)(AMESS(1),(AMAXI(II),II=1,16))
WRITE(8,8)(AMESS(2),(AMEAN(II),II=1,16))
WRITE(8,8)(AMESS(3),(AMINI(II),II=1,16))
WRITE(8,8)(AMESS(4),(SD(II),II=1,16))
8  FORMAT(A5,16(1X,F7.5))
9  FORMAT("AN ERROR HAS OCCURED <INPUT SEQUENCE>,TERMINATE RUN")
10 FORMAT(I6)

RETURN
END
```

## SUBROUTINE OFFST

C The first call to subroutine "OFFST" is made  
 C with the transmitter phase set at 180 degrees. The  
 C mean value of the signal at each channel given by  
 C AMEAN is stored in the first column of array OSET.  
 C When the second call is made to OFFST, the transmitter  
 C phase has been set to 0 degrees. This mean is then  
 C stored in the second column of OSET. We now have a  
 C measure of  $A \cdot G(0) \cos(\theta_i - 180) + \text{OFSET}$  and  
 C  $A \cdot G(0) \cos(\theta_i) + \text{OFSET}$  where A, G(0),  $\theta_i$ , and  
 C OFSET are the channel's amplitude, element gain,  
 C phase and DC offset respectively.  
 C The sum of these two components results in the  
 C cancellation of the first term. Division by two then  
 C gives the offset of each channel.

```

DIMENSION OSET(16,2)
COMMON//K,NSMPLS,AMEAN(16),OFSET(16)

```

```

DO 1 I=1,16

```

```

OSET(I,K)=AMEAN(I)

```

```

1 CONTINUE

```

```

IF(K.EQ.1)RETURN

```

```

DO 2 I1=1,16

```

```

OFSET(I1)=(OSET(I1,1)+OSET(I1,2))/2.0

```

```

2 CONTINUE

```

```

RETURN
END

```

## SUBROUTINE NORM

C This subroutine normalizes the data such that  
 C all the inphase channels have a maximum of unity for  
 C boresight alignment and 0 degree transmitter phase.  
 C The first step in the normalization process is  
 C to subtract the offsets and divide by the amplitude  
 C  $A \cdot G(0)$ . This is done to the I and Q pairs giving:

C  $I = G_n(\theta) \cos(\theta_i + \phi_{ii})$

C  $Q = G_n(\theta) \sin(\theta_i + \phi_{iq})$

C where  $\phi_{ii}$  and  $\phi_{iq}$  are the inphase and quadrature  
 C phase misalignments calculated in subroutine "PHASE"  
 C for  $\theta_i = 0$ . This is the channel phase which must  
 C be preserved, it will be common to both I and Q  
 C channels.  $G_n(\theta) = G(\theta) / G(0)$  is the element  
 C pattern normalized w.r.t. depression angle  $\theta = 0$   
 C (boresight). The normalized In and Qn channels are  
 C then calculated in the following fashion:

C  $I_n = [I \sin(\phi_{iq}) - Q \sin(\phi_{ii})] / \sin(\phi_{iq} - \phi_{ii})$   
 C  $= G_n(\theta) \cos(\theta_i)$

C  $Q_n = [I \cos(\phi_{iq}) - Q \cos(\phi_{ii})] / \sin(\phi_{iq} - \phi_{ii})$   
 C  $= G_n(\theta) \sin(\theta_i)$

C Notice that  $Q_n$  is now a sine function as it should  
 C be in the strict sense of quadrature.

COMMON/SHIP/ANORM(16)  
 COMMON//K, NSMPLS, AMEAN(16), OPSET(16), PHASE(16), AMP(16)

DO 1 I1=1,8

I2=I1+8  
 C1=COS(PHASE(I1))  
 C2=COS(PHASE(I2))  
 S1=SIN(PHASE(I1))  
 S2=SIN(PHASE(I2))  
 DIFFER=PHASE(I2)-PHASE(I1)  
 SINDIF=SIN(DIFFER)  
 TEMP1=(AMEAN(I1)-OPSET(I1))/AMP(I1)  
 TEMP2=(AMEAN(I2)-OPSET(I2))/AMP(I2)  
 ANORM(I1)=(TEMP1\*S2 - TEMP2\*S1)/SINDIF  
 ANORM(I2)=(TEMP1\*C2 - TEMP2\*C1)/SINDIF

1 CONTINUE

WRITE(8,2) (ANORM(I2), I2=1,16)

2 FORMAT(1X, "NORM", 16(1X, F7.3))

RETURN  
 END

## SUBROUTINE SHIFT

```

C      In this subroutine the normalized signals In and
C      Qn are shifted in phase so that no matter which angle
C      the array is being illuminated from, the first element
C      always has a phase of zero. This means that the
C      bottom element of the array is our reference, and the
C      array is rotating about this point. The signal
C      amplitude of this element will be zero for the quadrature
C      component and G(theta) (gain of the horn for look
C      angle theta) for the inphase component. The resulting
C      gain phase and signal value are then stored file
C      #AJUST (LU#11) to be used later by program "SHAPE".
C
COMMON/SHIF/ANORM(16)
COMMON/ANGLE/ANGLE
DIMENSION SIGNAL(16),GAIN(8),PHASE(8)

TWOPI=8.0*ATAN(1.0)

DO 1 I=1,8

  IP8=I+8
  PHASE(I)=ATAN2(ANORM(IP8),ANORM(I))
  GAIN(I)=SQRT(ANORM(IP8)**2 + ANORM(I)**2)
  IF(I.EQ.1)PASE1=PHASE(1)
  PHASE(I)=PHASE(I)-PASE1
  IF(PHASE(I).LT.0.0)PHASE(I)=PHASE(I)+TWOPI
  SIGNAL(I)=GAIN(I)*COS(PHASE(I))
  SIGNAL(IP8)=GAIN(I)*SIN(PHASE(I))

1. CONTINUE

WRITE(8,3)(SIGNAL(I),I=1,16)
WRITE(8,4)
RADEG=45.0/ATAN(1.0)

DO 2 I=1,8

  PHAZE=RADEG*PHASE(I)
  WRITE(8,5)I,GAIN(I),PHAZE

2. CONTINUE

TEMP1=ANGLE*ATAN(1.0)/45.0
WRITE(11,6)TEMP1
WRITE(11,7)(GAIN(I),PHASE(I),I=1,8)

3. FORMAT(1X,"SGNL",16(1X,F7.3))
4. FORMAT(1H0,6X"THE SIGNAL GAIN AND PHASE AT EACH HORN "///.8(I10,5
+X,F10.5,/))
5. FORMAT(1X,I5,3(10X,F10.6))
6. FORMAT(G13.6)
7. FORMAT(8G13.6)

RETURN
END

```

BLOCK DATA

COMMON/SHIF/ANORM(16)  
COMMON/ANGLE/ANGLE

END

FTN4,L  
PROGRAM DPGEN

```

C      * * * * *
C      * * * * *
C      * *          B.3.1    PROGRAM DPGEN          * *
C      * * * * *
C      * * * * *
C      * * * * *

```

C The purpose of this program is to generate the  
C diffuse reflection coefficients required to shape  
C the antenna pattern acquired through "DVS72" and  
C transformed with "AJUST".

C Subroutine "INTI" initializes the starting  
C parameters. "GEOM" calculates the target geometry  
C defining the extent of the glissening surface. This  
C surface is divided into equal angular steps by  
C subroutine "ANGL". The function  $d(\text{RHOD}^{**2})/d(\text{angle})$   
C is then formed via "PD2" which calls upon two  
C functions "YSIZE" and "PD2".

```

REWIND 12
CALL INTI
CALL GEOM
CALL ANGL
CALL PD2
CALL RHO
CALL OUTPT
WRITE(12,1)666.,666.,666.
ENDFILE 12

```

FORMAT(3G13.6)

```

STOP
END

```



## SUBROUTINE INTI

```

C      >>>>> PARAMETERS <<<<<<
C      RADEG : ONE DEGREE EXPRESSED IN RADIANS
C      P1DEG : ONE TENTH OF A DEGREE EXPRESSED IN RADIANS
C      WAVLEN : RADARS WAVELENGTH ( 3 CENTIMETERS )
C      RANGE : TARGET'S RANGE
C      ELEVA : TARGET'S ELEVATION IN DEGREES
C      ELEV  : TARGET'S ELEVATION IN RADIANS
C      RADHI : RADAR'S HEIGHT FROM GROUND
C      TARHI : TARGET'S HEIGHT FROM GROUND
C      BETA0 : RMS SURFACE SLOPE OF GLISSENING SURFACE
C      SIGMAH : RMS SURFACE HEIGHT DEVIATION
C      FFSHOL : FOUR PI SIGMAH OVER LAMBDA

```

```

COMMON/GEONI/RANGE,ELEV,RADHI,TARHI,ANGLA,THETA,ANGLB
COMMON/SURFU/BETA0,SIGMAH,RADEG,PI,P1DEG,WAVLEN,FFSHOL
COMMON/PLT/LU, ID

```

```

TEMP=ATAN(1.0)
RADEG=TEMP/45.0
PI=4.0*TEMP
P1DEG=.1*RADEG
WAVLEN=.03
WRITE(1,10)
READ(1,*)RANGE,ELEVA,RADHI,BETA0,SIGMAH
LU=40
ID=2
ELEV=ELEVA*RADEG
FFSHOL=4.0*PI*SIGMAH/WAVLEN

```

```

10  FORMAT(// "INPUT:  1 / TARGET RANGE"/9X"2 / TARGET ELEVATION"/9X
+ "3 / RADAR HEIGHT"/9X"4 / RMS SLOPE OF SURFACE FACETS"/9X
+ "5 / RMS SURFACE HEIGHT DEVIATION")

```

```

RETURN
END

```

## SUBROUTINE GEOM

C THIS SUBROUTINE PERFORMS THE FUNCTION OF SOLVING  
 C EQUATION 13 CHAPTER #2 FOR Y=0. THIS GIVES THE  
 C EXTENT OF THE GLISSING SURFACE IN TERMS OF RANGE.  
 C THE RANGE COORDINATES ARE THEN CONVERTED TO ELEVATION  
 C ANGLES.

C >>>>> PARAMETERS <<<<<<

C ANGLA : NEAR LIMIT OF GLISSING SURFACE  
 C ANGLB : FAR LIMIT OF GLISSING SURFACE  
 C RANGE : TARGET RANGE  
 C ELEVA : TARGET ELEVATION  
 C RADHI : RADAR HEIGHT FROM SURFACE  
 C TARHI : TARGET HEIGHT FROM SURFACE  
 C THETA : DEPRESSION ANGLE FOR SPECULAR REFLECTION  
 C BETA0 : RMS SLOPE OF SURFACE FACETS  
 C GROUND : GROUND RANGE OF TARGET

COMMON/GEOMI/RANGE,ELEV,RADHI,TARHI,ANGLA,THETA,ANGLB  
 COMMON/SURFU/BETA0,SIGMAH,RADEG,PI,PIDEG,WAVLEN,FPSHOL  
 COMMON/IN/ANGLE(1024),PD(1024),DELAY(1024),WIDTH(1024),RHOD(1024)  
 COMMON/STUFF/N,DELRAD  
 COMMON/XAXES/X1,X2,GROUND

TARHI=RANGE\*SIN(ELEV)+RADHI  
 THETA=ATAN(TAN(ELEV)\*(RADHI+TARHI)/(TARHI-RADHI))  
 WRITE(1,2)  
 READ(1,\*)ISPEC  
 IF(ISPEC.EQ.0)GOTO 1  
 ANG=AIN(THETA/PIDEG)  
 TEST=ANG\*PIDEG-THETA  
 IF(TEST.GE.HALF)THETA=ANG\*PIDEG  
 IF(TEST.LT.HALF)THETA=(ANG+1.0)\*PIDEG  
 TEMP=TAN(THETA)/TAN(ELEV)  
 TARHI=RADHI\*(TEMP+1)/(TEMP-1)  
 RANGE=(TARHI-RADHI)/SIN(ELEV)  
 GROUND=RANGE\*COS(ELEV)  
 BA=-(RADHI+TARHI+2.0\*BETA0\*GROUND)  
 BB=-(RADHI+TARHI-2.0\*BETA0\*GROUND)  
 XA=(-BA-SQRT(BA\*BA-8.0\*BETA0\*GROUND\*RADHI))/(4.0\*BETA0)  
 XB=(-BB-SQRT(BB\*BB+8.0\*BETA0\*GROUND\*RADHI))/(-4.0\*BETA0)  
 ANGLA=ATAN(RADHI/XA)  
 ANGLB=ATAN(RADHI/XB)

2 FORMAT("SPECULAR POINT A INTEGER MULTIPLE OF PIDEG ? 1/0")

RETURN  
 END

## SUBROUTINE ANGL

```

C      THE GLISSING SURFACE DEFINED IN SUBROUTINE "GEOM"
C      IS NOW BROKEN UP INTO SMALL STEPS.

C      >>>>> PARAMETERS <<<<<<<

C      ANGLE(I):  VECTOR OF ANGLES ANALYSIED
C      DELRAD   :  STEP SIZE BETWEEN SUCCESSIVE ANGLES
C      ANGLA    :  ANGLE OF REFLECTION AT NEAR EDGE OF GLISSING SURFACE
C      ANGLB    :  ANGLE OF REFLECTION AT FAR EDGE OF GLISSING SURFACE
C      THETA    :  ANGLE OF SPECULAR REFLECTION

COMMON/GEOMI/RANGE,ELEV,RADHI,TARHI,ANGLA,THETA,ANGLB
COMMON/SURFU/BETA0,SIGMAH,RADEG,PI,P1DEG,WAVLEN,FPSHOL
COMMON/IN/ANGLE(1024),PD(1024),DELAY(1024),WIDTH(1024),RHOD(1024)
COMMON/STUFF/N,DELRAD

RADEG=ATAN(1.0)/45.0
ANGA=ANGLA/RADEG
WRITE(1,5)ANGA
READ(1,*)IOK
IF(IOK.EQ.1)GOTO 7
WRITE(1,6)
READ(1,*)ANGA
ANGLA=ANGA*RADEG
7  DELRAD=(ANGLA-ANGLB)/100.
   IF(DELRAD.LE.P1DEG)GOTO 1
   DELRAD=AINT(DELRAD/P1DEG)*P1DEG
   GOTO 2
1  DELRAD=P1DEG
2  ANGLE(1)=ANGLA
   START=AINT(ANGLA/DELRAD)*DELRAD+DELRAD

DO 3 I=2,1024

N=I
ANGLE(I)=START+FLOAT(I-1)*DELRAD
IF(ANGLE(I).LT.ANGLB)GOTO 4

3  CONTINUE

4  ANGLE(N)=ANGLB

5  FORMAT("THE GLISSING SURFACE EXTENDS TO "P6.4" OK ? 1/0")
6  FORMAT("AT WHAT ANGLE SHALL IT BE TERMINATED ?")

RETURN
END

```

## SUBROUTINE PD2

```

C      HERE THE POWER DENSITY IS CALCULATED.  THE POWER
C      DENSITY  $d(\text{RHOD}^{**2})/d(\text{angle})$  IS GIVEN BY EQUATION 19
C      OF CHAPTER #2.  THE TERMS PD AND Y OF THIS EQUATION
C      ARE CALCULATED IN FUNCTION "PD2" AND "YSIZE".

C      >>>>>  PARAMETERS  <<<<<<

C      SIGMAH   :   RMS SURFACE HEIGHT DEVIATION
C      PD(I)    :   VECTOR OF REFLECTION COEFFICIENTS' SLOPES AT ANGLE(I)
C      PD2      :   ROUGHNESS FACTOR (SEE FUNCTION PD2)
C      WAVLEN   :   WAVELENGTH OF THE RADAR

COMMON/GEOMI/RANGE,ELEV,RADHI,TARHI,ANGLA,THETA,ANGLB
COMMON/SURFU/BETA0,SIGMAH,RADEG,PI,P1DEG,WAVLEN,PPSHOL
COMMON/IN/ANGLE(1024),PD(1024),DELAY(1024),WIDTH(1024),RHOP(1024)
COMMON/STUFF/N,DELRAD
COMMON/XAXES/X1,X2,GROUND

AMULT=(RANGE**2)/(2.0*PI)
STEP=P1DEG/300.
HALF=P1DEG/2.

DO 2 I=2,N-1

TEMP1=0.0
TEMP2=0.0
STORE=0.0

DO 1 J=1,300

ANG=ANGLE(I)+FLOAT(J-1)*STEP-HALF
IF((ANG.LT.ANGLB).OR.(ANG.GT.ANGLA))GOTO 1
Y=YSIZE(ANG)
WIDTH(I)=WIDTH(I)+Y
CALL DELA(I)
STORE=DELAY(I)+STORE
IF(Y.EQ.0.0)GOTO 1
F=PD2(ANG)
TEMP1=1.0/(((GROUND-RADHI/TAN(ANG))**2)*(COS(ANG)**2))
TEMP2=AMULT*Y*F*TEMP1/RADHI + TEMP2

1  CONTINUE

PD(I)=TEMP2/300.
WIDTH(I)=WIDTH(I)/300.
DELAY(I)=STORE/300.
IF(PD(I).EQ.0.0)DELAY(I)=0.0

2  CONTINUE

RETURN
END

```

SUBROUTINE DELA(I)

C THIS SUBROUTINE IS USED TO FIND THE PATH LENGTH  
C DIFFERENCE BETWEEN THE DIRECT AND REFLECTED PATHS.

C >>>>> PARAMETERS <<<<<<

C R1 : THE PATH LENGTH FROM RECEIVER TO REFLECTION POINT  
C R2 : THE PATH LENGTH FROM TARGET TO REFLECTION POINT  
C RANGE : THE PATH LENGTH FROM RECEIVER TO TARGET  
C DELTA : THE PATH LENGTH DIFFERENCE (IN FRACTIONS OF WAVELENGTHS)  
C DELAY : PHASE DELAY DUE TO DIFFERENCE IN PATHS  
C THI : PHASE SHIFT INDUCED BY THE REFLECTING SURFACE

COMMON/XAXES/X1,X2,GROUND  
COMMON/GEOMI/RANGE,ELEV,RADHI,TARHI,ANGLA,THETA,ANGLB  
COMMON/IN/ANGLE(1024),PD(1024),DELAY(1024),WIDTH(1024),RHOD(1024)  
COMMON/SURFU/BETA0,SIGMAH,RADEG,PI,PIDEG,WAVLEN,FPSHOL

R1=SQRT(X1\*\*2+RADHI\*\*2)  
R2=SQRT(X2\*\*2+TARHI\*\*2)  
THI=.015  
DELTA=(R1+R2-RANGE)/WAVLEN + THI  
DELTA=DELTA-AINT(DELTA)  
DELAY(I)=2.0\*PI\*DELTA

RETURN  
END

FUNCTION YSIZE(ANG)

C THE EXTENT OF THE GLISSENING SURFACE IN THE Y  
C DIRECTION IS EVALUATED HERE.

C >>>>> PARAMETERS <<<<<<

C YSIZE : WIDTH OF THE GLISSENING SURFACE AT ANGLE ANG

COMMON/GEOMI/RANGE,ELEV,RADHI,TARHI,ANGLA,THETA,ANGLB  
COMMON/SURFU/BETA0,SIGMAH,RADEG,PI,P1DEG,WAVLEN,FPSHOL  
COMMON/IN/ANGLE(1024),PD(1024),DELAY(1024),WIDTH(1024),RHOD(1024)  
COMMON/STUFF/N,DELRAD  
COMMON/XAXES/X1,X2,GROUND

TEMP1=TAN(ANG)  
X1=RADHI/TEMP1  
X2=GROUND-X1  
TEMP2=TARHI/X2  
TEMP3=(X1\*X2/(X1+X2))\*(TEMP1+TEMP2)  
TEMP4=BETA0\*\*2-((TEMP1-TEMP2)\*\*2)/4.0  
IF(TEMP4.LE.0.0)GOTO 1  
YSIZE=TEMP3\*SQRT(TEMP4)

RETURN

1 YSIZE=0.0

RETURN  
END

FUNCTION FD2(ANG)

C THE ROUGHNESS FACTOR(FD2, EQUATION 16 CHAPTER #2), IS  
C CALCULATED HERE.

C >>>>> PARAMETERS <<<<<<

C FD2 : THE ROUGHNESS FACTOR AT ANGLE ANG  
C PS11 : REFLECTION ANGLE SEEN BY RADAR  
C PS12 : INCIDENT ANGLE OF RADIATION FROM TARGET  
C PS12 : SPECULAR REFLECTION COEFFICIENT FOR PS11  
C PS22 : SPECULAR REFLECTION COEFFICIENT FOR PS12  
C BETA : BISTATIC ANGLE  
C SIGMA0 : BISTATIC RADAR SCATTERING COEFFICIENT

COMMON/GEOMI/RANGE,ELEV,RADHI,TARHI,ANGLA,THETA,ANGLB  
COMMON/SURPU/BETA0,SIGMAH,RADEG,PI,P1DEG,WAVLEN,FPSHOL  
COMMON/XAXES/X1,X2,GROUND

PS11=ATAN(RADHI/X1)  
PS12=ATAN(TARHI/X2)  
PS12=EXP(-(FPSHOL\*SIN(PS11))\*\*2)  
PS22=EXP(-(FPSHOL\*SIN(PS12))\*\*2)  
BETA=(PS12-PS11)/2.0  
SIGMA0=EXP(-(TAN(BETA)/TAN(BETA0))\*\*2)/(TAN(BETA0)\*\*2)  
FD2=SIGMA0\*SQRT((1.0-PS12)\*(1.0-PS22))

RETURN  
END

## SUBROUTINE RHO

C IN THIS SUBROUTINE THE VALUE OF THE DIFFUSE  
C REFLECTION COEFFICIENT (RHOD) IS EVALUATED. THE  
C ANGLE, MAGNITUDE, AND PHASE OF THE REFLECTION  
C COEFFICIENT ARE WRITTEN ON LU#12 IN FILE #DFGEN.

C >>>>> PARAMETERS <<<<<<

C PD : RHO d SQUARED PER P1DEG  
C RHOD : THE DIFFUSE REFLECTION COEFFICIENT

COMMON/IN/ANGLE(1024),PD(1024),DELAY(1024),WIDTH(1024),RHOD(1024)  
COMMON/STUFF/N,DELRAD  
COMMON/SURFU/BETA0,SIGMAH,RADEG,PI,P1DEG,WAVLEN,PPSHOL

RHOSQ=0.0

DO 1 I=N,1,-1

RHOD(I)=SQRT(PD(I)\*P1DEG)  
WRITE(12,2)ANGLE(I),RHOD(I),DELAY(I)

1 CONTINUE

2 FORMAT(3G13.6)

RETURN  
END



## SUBROUTINE OUTPT

```
COMMON/GEOMI/RANGE,ELEV,RADHI,TARHI,ANGLA,THETA,ANGLB
COMMON/SURFU/BETA0,SIGMAH,RADEG,PI,PLDEG,WAVLEN,FPSHOL
COMMON/IN/ANGLE(1024),PD(1024),DELAY(1024),WIDTH(1024),RHOD(1024)
COMMON/STUFF/N,DELRAD
COMMON/PLT/LU, ID
```

```
ELEVA=ELEV/RADEG
A=ANGLA/RADEG
B=ANGLB/RADEG
THET=THETA/RADEG
DELRAD=DELRAD/RADEG
```

```
DO 1 I=1,N
```

```
ANGLE(I)=ANGLE(I)/RADEG
YMAX2=AMAX1(YMAX2,RHOD(I))
YMAX=AMAX1(YMAX,PD(I))
FAZEM=AMAX1(FAZEM,DELAY(I))
WIDMAX=AMAX1(WIDMAX,WIDTH(I))
IF(PD(I).EQ.YMAX)ANGMAX=ANGLE(I)
IF(RHOD(I).EQ.YMAX2)ANGHX2=ANGLE(I)
```

```
1 CONTINUE
```

```
XMAX=ANGLE(2)+DELRAD
WRITE(6,10)RANGE,ELEVA,RADHI,TARHI,A,THET,B,BETA0,SIGMAH,DELRAD,N
+,YMAX,ANGMAX,YMAX2,ANGMX2
CALL GRAPH(ANGLE,WIDTH,N,1,1,0.,XMAX,0.,WIDMAX)
WRITE(1,40)
PAUSE
CALL GRAPH(ANGLE,RHOD,N,1,1,0.,XMAX,0.,YMAX2)
WRITE(1,40)
PAUSE
CALL GRAPH(ANGLE,DELAY,N,1,1,0.,XMAX,0.,FAZEM)
WRITE(6,20)
WRITE(6,36)(I,ANGLE(I),PD(I),RHOD(I),WIDTH(I),I=1,N)
```

```
10 FORMAT(" TARGET STATISTICS"////) TARGET RANGE : "G13.6/
+" TARGET ELEVATION : "G13.6/" RADAR HEIGHT : "G13.6/
+" TARGET HEIGHT : "G13.6/" NEAR REFLECT : "G13.6/
+" SPECULAR POINT : "G13.6/" DISTANT REFLECT : "G13.6/
+" RMS SURFACE SLOPE : "G13.6/" RMS SURFACE DEVI.: "G13.6/
+" INTEGRATION STEP : "G13.6/" NUMBER OF STEPS : "15/
+" MAX. POWER PD : "G13.6/" MAX. POWER ANGLE : "G13.6/
+" MAX. RFLCT COEF. : "G13.6/" MAX. RFLCT ANGLE : "G13.6/////
20 FORMAT(" SAMPLE#*5X"DEPRESS ANGLE*9X"d(RHOD**2)/d(THETA)*9X"RHOD"
+9X"YSIZE"/////))
30 FORMAT(1X,15,7X,G13.6,13X,G13.6,13X,G13.6,13X,G13.6/)
40 FORMAT("CHANGE PAPER IN PLOTTER BED")
```

```
RETURN
END
```

## BLOCK DATA

```
COMMON/GEOMI/RANGE,ELEV,RADHI,TARHI,ANGLA,THETA,ANGLB  
COMMON/SURPU/BETA0,SIGMAH,RADEG,PI,P1DEG,WAVLEN,FPSHOL  
COMMON/STUFF/N,DELRAD  
COMMON/XAXES/X1,X2,GROUND  
COMMON/IN/ANGLE(1024),PD(1024),DELAY(1024),WIDTH(1024),RHOD(1024)
```

END

FTN4,L  
 \$ENA(DFSIG,0)  
 PROGRAM SHAPE

```

C      * * * * *
C      * * * * *
C      * *          B.4.1    PROGRAM SHAPE          * *
C      * * * * *
C      * * * * *
  
```

C The purpose of this program is to shape the surface  
 C reflection coefficient with the antenna pattern  
 C acquired from the phased array receiver. The computer  
 C generated diffuse reflection coefficients are acquired  
 C from file #DFGEN via LU#12. The experimentally acquired  
 C element gains and phases are read from #AJUST at LU#11.  
 C In the main program these two files are then processed in  
 C subroutine " DFSIG " to form the hybrid diffuse reflection  
 C coefficient accounting for antenna gain.

```

C      >>>>>  PARAMETERS  <<<<<<
C      AGHX1  :  MAXIMUM ANGLE OF THE GLISSING SURFACE
C      AGHX2  :  MAXIMUM ANGLE FOR WHICH DATA IS AVAILABLE
C      RHOD   :  DIFFUSE REFLECTION COEFFICIENT
C      DELAY  :  PHASE DELAY OF REFLECTION COEFFICIENT
C      GAIN   :  ELEMENT PATTERN
C      PHASE  :  RELATIVE PHASE OF A GIVEN ELEMENT
C      IEOP   :  END OF FILE MARKER
  
```

```

COMMON/DFSIG/AMP(200,8),FAZE(200,8)
COMMON/LU12/ ANGL(200),RHOD(200),DELAY(200)
COMMON/LU11/ GAIN(200,8),PHASE(200,8)
  
```

```

REWIND 13
REWIND 12
REWIND 11
  
```

```

IEOP=666
RADEG=ATAN(1.0)/45.0
P1DEG=.1*RADEG
AHALF=.5*P1DEG
MAHALF=-AHALF
  
```

```

K=1
ANG2=-1.
1 READ(12,10) ANGL(K),RHOD(K),DELAY(K)
  DIFFER=ANG2-ANG1(K)
  IF(IFIX(ANG1(K)).EQ.IEOP)GOTO 4
  IF(AGHX1.LT.ANGL(K))AGHX1=ANG1(K)
  
```

```

IF(DIFFER.GT.AHALF)GOTO 1
IF(ABS(DIFFER).LT.AHALF)GOTO 3
2 READ(11,11)ANG2
DIFFER=ANG2-ANG1(K)
IF(IFIX(ANG2).EQ.IEOF)GOTO 5
READ(11,14)(GAIN(K,I),PHASE(K,I),I=1,8)
IF(AGHX2.LT.ANG2)AGHX2=ANG2
IF(DIFFER.LT.MAHALF)GOTO 2
IF(ABS(DIFFER).GT.AHALF)GOTO 1
3 WRITE(6,99)K,ANG1(K),ANG2,GAIN(K,1),RHOD(K)
99 FORMAT(" INDEX# "14" ANGLE1 "G13.6" ANGLE2 "G13.6
+" GAIN "G13.6" RHO d "G13.6)
CALL DIFSG(K)
K=K+1
GOTO 1
4 TEMP1=AGMX1/RADEG
WRITE(1,12)TEMP1
GOTO 6
5 TEMP2=AGHX2/RADEG
WRITE(1,13)TEMP2
6 CALL SUMER(K)
CALL PLOTR(K)
ENDFILE 13

10 FORMAT(3G13.6)
11 FORMAT(G13.6)
12 FORMAT("END OF FILE ENCOUNTERED AT LU#12 THE MAXIMUM ANGLE PROCESS
+ED WAS "F10.6" DEGREES")
13 FORMAT("END OF FILE ENCOUNTERED AT LU#11 DATA ONLY AVAILABLE UP TO
+ A MAXIMUM ANGLE OF "F10.6" DEGREES")
14 FORMAT(8G13.6)

STOP
END

```

```
SEMA(DFSIG,0)
  SUBROUTINE DIFSG(K)
```

```
C      The resultant diffuse reflection coefficient is the
C      product of the generated coefficient on the receiver
C      element gain pattern. The signal phase is the antenna element
C      phase (PHASE) relative to the eighth element plus the phase
C      of the generated diffuse model (DELAY) and the phase shift (FI)
C      input to position the receivers main lobe. to (ANGLE).
```

```
COMMON/DFSIG/AMP(200,8),FAZE(200,8)
COMMON/LU/2/ANGL(200),RHOD(200),DELAY(200)
COMMON/LU/1/GAIN(200,8),PHASE(200,8)
COMMON/MAX/AMPMAX,FAZMAX,RHOMAX,DELMAX
```

```
IF(K.GT.1)GOTO 4
RADEG=ATAN(1.0)/45.0
TWOPI=8.0*ATAN(1.0)
ALAM=3.01
D=6.68
WRITE(1,3)
READ(1,*)ANGLE
ANGLE=RADEG*ANGLE
AL=D*SIN(ANGLE)
FI=TWOPI*AL/ALAM
```

```
4 DO 1 I=1,8
```

```
C IF(GAIN(K,I).EQ.0.0)GAIN(K,I)=GAIN(K-1,I)
C IF(GAIN(K,I).EQ.0.0)PHASE(K,I)=PHASE(K-1,I)
AMP(K,I)=RHOD(K)*GAIN(K,I)
FAZE(K,I)=PHASE(K,I)+DELAY(K)-(I-1)*FI
5 IF(FAZE(K,I).LT.0.0)FAZE(K,I)=FAZE(K,I)+TWOPI
IF(FAZE(K,I).LT.0.0)GOTO 5
6 IF(FAZE(K,I).GT.TWOPI)FAZE(K,I)=FAZE(K,I)-TWOPI
IF(FAZE(K,I).GT.TWOPI)GOTO 6
IF(AMP(K,I).EQ.0.0)FAZE(K,I)=0.0
IF(AMPMAX.LT.AMP(K,I))AMPMAX=AMP(K,I)
IF(FAZMAX.LT.FAZE(K,I))FAZMAX=FAZE(K,I)
IF(RHOMAX.LT.RHOD(K))RHOMAX=RHOD(K)
IF(DELMAX.LT.DELAY(K))DELMAX=DELAY(K)
WRITE(13,2)AMP(K,I),FAZE(K,I)
```

```
1 CONTINUE
```

```
ANGL(K)=ANGL(K)/RADEG
```

```
2 FORMAT(1X,2G13.6)
```

```
3 FORMAT("AT WHICH ANGLE DO YOU WISH TO PLACE THE MAIN BEAM?")
```

```
RETURN
END
```

```
SEMA(DFSIG,0)
  SUBROUTINE SUHER(K)
```

```
C      In this subroutine the I and Q's of the eight
C      elements are summed for each angle and the resulting
C      amplitude and phase values are determined.
```

```
COMMON/DFSIG/AMP(200,8),FAZE(200,8)
COMMON/MAX2/APSMAX,FZSHAX
COMMON/SUM/AMPSM(200),FAZSM(200)
COMMON/LU12/ANGL(200),RHOD(200),DELAY(200)
COMMON/LU11/GAIN(200,8),PHASE(200,8)
```

```
TWOPI=8.0*ATAN(1.0)
K=K-1
DO 2 I2=1,K
```

```
SUMI=0.0
SUMQ=0.0
```

```
DO 1 I1=1,8
```

```
SUMI=SUMI+GAIN(I2,I1)*COS(FAZE(I2,I1))
SUMQ=SUMQ+GAIN(I2,I1)*SIN(FAZE(I2,I1))
```

```
1 CONTINUE
```

```
FAZSM(I2)=ATAN2(SUMQ,SUMI)
IF(FAZSM(I2).LT.0.0)FAZSM(I2)=FAZSM(I2)+TWOPI
IF(FZSHAX.LT.FAZSM(I2))FZSHAX=FAZSM(I2)
AMPSM(I2)=SQRT(SUMI**2+SUMQ**2)*RHOD(I2)
IF(APSMAX.LT.AMPSM(I2))APSMAX=AMPSM(I2)
```

```
2 CONTINUE
```

```
RETURN
END
```

```
SEHA(DFSIG,0)
  SUBROUTINE PLOTR(K)
```

```
C      In this subroutine the various amplitude and phase
C      plots are generated.
```

```
COMMON/PLT/LU, ID
COMMON/LU12/ANGLE(200), RHOD(200), DELAY(200)
COMMON/DFSIG/AMP(200,8), FAZE(200,8)
COMMON/MAX/ANPMAX, FAZMAX, RHOMAX, DELMAX
COMMON/MAX2/APSMAX, FZSHAX
COMMON/SUN/AMPSH(200), FAZSH(200)
DIMENSION ANPLT(200), FZPLT(200)
```

```
WRITE(1,4)
READ(1,*)IPLT
LU=40
ID=2
CALL GRAPH(ANGLE, RHOD, K, 1, 1, 0., ANGLE(K), 0., RHOMAX)
WRITE(1,2)
PAUSE
CALL GRAPH(ANGLE, DELAY, K, 1, 1, 0., ANGLE(K), 0., DELMAX)
WRITE(1,2)
PAUSE
```

```
DO 1 I=1,8
DO 3 J=1,K
AMPLT(J)=AMP(J,I)
FZPLT(J)=FAZE(J,I)
CONTINUE
```

```
IF((IPLT.EQ.1).AND.(I.NE.8))GOTO 1
CALL GRAPH(ANGLE,AMPLT,K,1,1,0.,ANGLE(K),0.,AMPMAX)
WRITE(1,2)
PAUSE
CALL GRAPH(ANGLE,FZPLT,K,1,1,0.,ANGLE(K),0.,FAZMAX)
WRITE(1,2)
PAUSE
```

```
CONTINUE
```

```
CALL GRAPH(ANGLE,AMPSH,K,1,1,0.,ANGLE(K),0.,APSHAX)
WRITE(1,2)
PAUSE
```

```
CALL GRAPH(ANGLE,FAZSH,K,1,1,0.,ANGLE(K),0.,FZSHAX)
```

```
FORMAT("CHANGE THE PAPER IN PLOTTER BED")
```

```
FORMAT("IF YOU WANT TO PLOT ONLY ONE ELEMENT PATTERN ENTER 1")
```

```
RETURN
END
```

## BLOCK DATA

COMMON/LU11/GAIN(200,8),PHASE(200,8)  
COMMON/LU12/ANGL(200),RHOD(200),DELAY(200)  
COMMON/SUM/SUNI(200),SUNQ(200)  
COMMON/MAX/AMPMAX,FAZMAX,RHOMAX,DELMAX  
COMMON/MAX2/APSHAX,PZSHAX

END





```
SEMA(MATRX,0)  
SUBROUTINE PTRHO
```

```
COMMON/COUNT/ICOUNT  
COMMON/MATRX/RHO(100,100),ANGLE(3000),SLOPE(3000)  
COMMON/STEP/RADSTP,XSTEP,STPFLG
```

```
IF(STPFLG.EQ.1.0)STEP=RADSTP  
IF(STPFLG.EQ.2.0)STEP=XSTEP
```

```
DO 2 J=1,100
```

```
ASLOPE=0.0  
K2=J*30  
K1=K2-29
```

```
DO 1 I=K1,K2
```

```
ASLOPE=SLOPE(I) + ASLOPE
```

```
1 CONTINUE
```

```
RHO(ICOUNT,J)=SQRT(STEP*ASLOPE/30.)
```

```
2 CONTINUE
```

```
RETURN  
END
```

SEMA(MATRX,0)  
SUBROUTINE PLOT

COMMON/LABEL/LABEL(23)  
COMMON/WAIT/IWAIT  
COMMON/PRMTR/PRMTR(10)  
COMMON/MATRX/Z(100,100),ANGLE(3000),SLOPE(3000)  
COMMON/SURFU/BETA0,SIGMAH,RADEG,PI,ELEVA  
COMMON/STEP/RADSTP,XSTEP,STPFLG  
COMMON/PRINT/IPRAM,ANGMAX,ANGMIN,VARLO,VARUP,XMAX,XMIN

DOUBLE PRECISION LABEL,PRINT(5),MES1(5),MES2(5),MES3(5)  
DOUBLE PRECISION MES4(5),MES5(5),MES6(5),MES7(5),MES8(5)  
DOUBLE PRECISION MES9(5),MESA(5),BET,SIG,ELE  
DATA PRINT/8HSIGMA H ,8HBETA 0 ,8HELEVATON,8HLOOK ANG,7HDIFFUSE/  
DATA MES1/8HTHE DIFP,8HUSE REFL,8HSECTION C,8HOEFFICIE,8HNT VS. L/  
DATA MES2/8HOOK ANGL,8HE FOR VA,8HRYPING RM,8HS SURFAC,8HE HEIGHT/  
DATA MES3/8HOOK ANGL,8HE FOR VA,8HRYPING RM,8HS SURFAC,8HE SLOPE /  
DATA MES4/8HOOK ANGL,8HE FOR VA,8HRYPING TA,8HGET ELE,8HVATION ./  
DATA MES5/8H RMS ,8HSURFACE ,8HSLOPE = ,8H ,8H radians/  
DATA MES6/8H RMS S,8HSURFACE H,8HEIGHT = ,8H ,8H meters /  
DATA MES7/8H RMS ,8HSURFACE ,8HSLOPE = ,8H ,8H radians/  
DATA MES8/8H TAR,8HGET ELEV,8HATION = ,8H ,8H degrees/  
DATA MES9/8H TAR,8HGET ELEV,8HATION = ,8H ,8H degrees/  
DATA MESA/8H RMS S,8HSURFACE H,8HEIGHT = ,8H ,8H meters /

LABEL(21)=PRINT(IPRAM)  
LABEL(22)=PRINT(4)  
LABEL(23)=PRINT(5)  
C HORIZONTAL EXTENT OF PAPER  
PRMTR(1)=23.  
C VERTICAL EXTENT OF PAPER  
PRMTR(3)=20.  
PRMTR(4)=VARUP  
PRMTR(5)=VARLO  
PRMTR(7)=ANGMIN/RADEG  
PRMTR(8)=ANGMAX/RADEG  
IF(STPFLG.EQ.1.0)GOTO 1  
LABEL(12)=6HRANGE  
PRMTR(7)=XMAX  
PRMTR(8)=XMIN  
1 DO 2 I=1,5  
LABEL(I)=MES1(I)  
2 CONTINUE  
DO 3 I=6,10  
IF(IPRAM.EQ.1)LABEL(I)=MES2(I-5)  
IF(IPRAM.EQ.2)LABEL(I)=MES3(I-5)  
IF(IPRAM.EQ.3)LABEL(I)=MES4(I-5)  
3 CONTINUE  
DO 4 I=11,15  
IF(IPRAM.EQ.1)LABEL(I)=MES5(I-10)  
IF(IPRAM.EQ.2)LABEL(I)=MES6(I-10)  
IF(IPRAM.EQ.3)LABEL(I)=MES7(I-10)  
4 CONTINUE  
DO 5 I=16,20  
IF(IPRAM.EQ.1)LABEL(I)=MES8(I-15)  
IF(IPRAM.EQ.2)LABEL(I)=MES9(I-15)

```
5 IF (IPRAM.EQ.3) LABEL(1)=MESA(I-15)
  CONTINUE
  REWIND 15
  WRITE(15,10) BETA0,SIGMAH,ELEVA
  REWIND 15
  READ(15,20) BET,SIG,ELE
  IF (IPRAM.EQ.1) LABEL(14)=BET
  IF (IPRAM.EQ.1) LABEL(19)=ELE
  IF (IPRAM.EQ.2) LABEL(14)=SIG
  IF (IPRAM.EQ.2) LABEL(19)=ELE
  IF (IPRAM.EQ.3) LABEL(14)=BET
  IF (IPRAM.EQ.3) LABEL(19)=SIG
  PRMTR(6)=0.
  PRMTR(2)=20.
  IF (IWAIT.EQ.0) GOTO 6
  WRITE(1,30)
  PAUSE
6 CALL PLOT3D(100,100,3,4,1)

10 FORMAT(F8.6)
20 FORMAT(A8)
30 FORMAT("THIS PROGRAM IS WAITING FOR THE OK TO PLOT(BREAKNODE GO)")
  RETURN
  END
```

## SUBROUTINE INTI

```

COMMON/GEOMI/RANGE, ELEV, RADHI, TARHI, ANGLA, THETA, ANGLB, XA, XB
COMMON/SURFU/BETA0, SIGMAH, RADEG, PI, ELEVA
COMMON/STEP/RADSTP, XSTEP, STPPLG
COMMON/COUNT/ICOUNT
COMMON/PRINT/IPRAM, ANGHAX, ANGHIN, VARLO, VARUP, XMAX, XMIN

```

```

DIMENSION VAR(100,3), SIG(100), BET(100), ELE(100)
EQUIVALENCE (VAR(1,1), SIG(1)), (VAR(1,2), BET(1)), (VAR(1,3), ELE(1))
DOUBLE PRECISION PRINT(3)
DATA PRINT/6HSIGMAH, 6HBETA0, 6HELEVA /

```

```

IF (ICOUNT.GT.1) GOTO 6
ANGMAX=0.
ANGHIN=1.0E10
XMIN=1.0E10
XMAX=0.0
TEMP=ATAN(1.0)
RADEG=TEMP/45.0
PI=4.0*TEMP
WRITE(1,10)
READ(1,*) RANGE, RADHI
WRITE(1,20)
READ(1,*) IPRAM
I1=1
I2=2
IF (IPRAM-2) 1,2,3
1 I1=2
  I2=3
  GOTO 3
2 I1=1
  I2=3
3 WRITE(1,40) PRINT (IPRAM)
  READ(1,*) VARUP, VARLO
  WRITE(1,50) PRINT (I1), PRINT (I2)
  READ(1,*) VAR(I1, I1), VAR(I1, I2)
  STEP=(VARUP-VARLO)/99.
  DO 4 I=1,100
  VAR(I, IPRAM)=STEP*FLOAT(I-1)+VARLO
  VAR(I, I1)=VAR(I, I1)
  VAR(I, I2)=VAR(I, I2)
  BETA0=BET(I)
  SIGMAH=SIG(I)
  ELEVA=ELE(I)
  ELEV=ELEVA*RADEG
  WRITE(1,60) SIG(I), BET(I), ELE(I)
  CALL GEOM
  IF (ANGLA.GT.ANGHAX) ANGHAX=ANGLA
  IF (XB.GT.XMAX) XMAX=XB
  IF (ANGLB.LT.ANGHIN) ANGHIN=ANGLB
  IF (XA.LT.XMIN) XMIN=XA
4 CONTINUE
  TEMIN=ANGHIN/RADEG
  TEMAX=ANGHAX/RADEG
  WRITE(1,70) TEMIN, TEMAX

```

```
READ(1,*)L
IF(L.EQ.1)GOTO 5
WRITE(1,80)
READ(1,*)TEMIN,TEMAX
ANGMAX=TEMAX*RADEG
ANGMIN=TEMIN*RADEG
5 RADSTP=(ANGMAX-ANGMIN)/2999.
  XSTEP=(XMAX-XMIN)/2999.
6  BETAO=BET(ICOUNT)
  SIGMAH=SIG(ICOUNT)
  ELEVA=ELE(ICOUNT)
  ELEV=ELEVA*RADEG,

10  FORMAT(//"INPUT:  1 /  TARGET RANGE"/9X"2 /  RADAR HEIGHT"////9X)
20  FORMAT("WHICH PARAMETER IS VARVIABLE?//" SELECT:  1 /  RMS SURFAC
+E HEIGHT DEVIATION (SIGMA H)"/11X"2 /  RMS SLOPE OF SURFACE FACETS
+ (BETA 0)"/11X"3 /  TARGET ELEVATION ANGLE"////)
30  FORMAT("HOW MANY STEPS OF THE VARIABLE PARAMETER ARE DESIRED ?"/)
40  FORMAT("WHAT ARE THE UPPER AND LOWER LIMITS OF "A6" ?"/)
50  FORMAT("ENTER VALUES FOR "A6" AND "A6"/)
60  FORMAT(" SIGMAH  "G13.6" BETA0  "G13.6" ELEVATION  "G13.6//)
70  FORMAT("THE CURRENT EXTENT OF LOOK ANGLE IS "F6.4" TO "F6.4" DEG"/
+"IF THIS IS ACCEPTABLE ENTER 1 IF IT IS NOT THEN ENTER 0")

80  FORMAT("ENTER THE DESIRED VALUES OF ANGMIN AND ANGMAX")

RETURN
END
```

SEMA(MATRX,0)  
SUBROUTINE GEOM

C RANGE : TARGET RANGE  
C ELEV : TARGET ELEVATION  
C RADHI : RADAR HEIGHT FROM SURFACE  
C TARHI : TARGET HEIGHT FROM SURFACE  
C THETA : DEPRESSION ANGLE FOR SPECULAR REFLECTION  
C BETA0 : RMS SLOPE OF SURFACE FACETS  
C GROUND : GROUND RANGE OF TARGET

COMMON/GEOMI/RANGE,ELEV,RADHI,TARHI,ANGLA,THETA,ANGLB,XA,XB  
COMMON/SURFU/BETA0,SIGMAH,RADEC,PI,ELEVA  
COMMON/STEP/RADSTP,XSTEP,STPFLG  
COMMON/MATRX/PD(100,100),ANGLE(3000),SLOPE(3000)  
COMMON/XAXES/X1,X2,GROUND

TARHI=RANGE\*SIN(ELEV)+RADHI  
THETA=ATAN(TAN(ELEV)\*(RADHI+TARHI)/(TARHI-RADHI))  
GROUND=RANGE\*COS(ELEV)  
BA=-(RADHI+TARHI+2.0\*BETA0\*GROUND)  
BB=-(RADHI+TARHI-2.0\*BETA0\*GROUND)  
XA=(-BA-SQRT(BA\*BA-8.0\*BETA0\*GROUND\*RADHI))/(4.0\*BETA0)  
XB=(-BB-SQRT(BB\*BB+8.0\*BETA0\*GROUND\*RADHI))/(-4.0\*BETA0)  
ANGLA=ATAN(RADHI/XA)  
ANGLB=ATAN(RADHI/XB)

RETURN  
END

SENA(MATRX,0)  
SUBROUTINE ANGL1

C ANGLE(I) : VECTOR OF EQUALLY SPACED ANGLES  
C RADSTP : STEP SIZE BETWEEN SUCCESSIVE ANGLES  
C ANGLA : ANGLE OF REFLECTION AT NEAR EDGE OF GLISSING SURFACE  
C ANGLB : ANGLE OF REFLECTION AT FAR EDGE OF GLISSING SURFACE  
C THETA : ANGLE OF SPECULAR REFLECTION

COMMON/GEOM/RANGE,ELEV,RADHI,TARHI,ANGLA,THETA,ANGLB,XA,XB  
COMMON/SURFU/BETA0,SIGNAH,RADEG,PI,ELEVA  
COMMON/STEP/RADSTP,XSTEP,STPFLG  
COMMON/MATRX/PD(100,100),ANGLE(3000),SLOPE(3000)  
COMMON/PRINT/IPRAM,ANGHAX,ANGHIN,VARLO,VARUP,XMAX,XMIN

START=AINT(ANGHAX/RADSTP)\*RADSTP+RADSTP

DO 1 I=1,3000

ANGLE(I)=START - FLOAT(I-1)\*RADSTP

CONTINUE

RETURN  
END



SENA(MATRX,0)  
SUBROUTINE ANGL2

C ANGLE(I): VECTOR OF ANGLES REPRESENTING EQUAL RANGE SPACING  
C XSTEP : STEP SIZE BETWEEN SUCCESSIVE RANGE POINTS

COMMON/MATRX/Z(100,100),ANGLE(3000),SLOPE(3000)  
COMMON/GEOMI/RANGE,ELEV,RADHI,TARHI,ANGLA,THETA,ANGLB,XA,XB  
COMMON/STEP/RADSTP,XSTEP,STPFLG  
COMMON/PRINT/IPRAM,ANGMAX,ANGMIN,VARLO,VARUP,XMAX,XMIN

START=AINT(XMAX/XSTEP)\*XSTEP + XSTEP

DO 1 I=1,3000

X=START-FLOAT(I-1)\*XSTEP  
ANGLE(I)=ATAN(RADHI/X)

1 CONTINUE

RETURN  
END

```
SEMA(MATRX,0)
  SUBROUTINE ZLOPE
```

```
C   SIGMAH : RMS SURFACE HEIGHT DEVIATION
C   SLOPE(I): VECTOR OF SLOPES OF THE FUNCTION PD**2 AT ANGLE(I)
C   PD2    : ROUGHNESS FACTOR (SEE FUNCTION PD2)
```

```
COMMON/GEOMI/RANGE,ELEV,RADHI,TARHI,ANGLA,THETA,ANGLB,XA,XB
COMMON/SURFU/BETAO,SIGMAH,RADEG,PI,ELEVA
COMMON/STEP/RADSTP,XSTEP,STPFLG
COMMON/MATRX/PD(100,100),ANGLE(3000),SLOPE(3000)
COMMON/XAXES/X1,X2,GROUND
```

```
AMULT=(RANGE**2)/(2.0*PI)
```

```
DO 2 I=1,3000
```

```
Y=YSIZE(I)
```

```
IF(Y.EQ.0.0)GOTO 1
```

```
F=PD2(I)
```

```
TEMP=1.0/(((GROUND-RADHI/TAN(ANGLE(I)))**2)*(COS(ANGLE(I))**2))
```

```
TEMP1=1.0/((X2**2)*(X1**2))
```

```
1 IF(STPFLG.EQ.1.0)SLOPE(I)=AMULT*Y*F*TEMP/RADHI
```

```
IF(STPFLG.EQ.2.0)SLOPE(I)=AMULT*Y*F*TEMP1
```

```
2 CONTINUE
```

```
RETURN
END
```

```
SEMA(MATRX,0)
FUNCTION YSIZE(IANG)
```

C YSIZE : WIDTH OF THE GLISSING SURFACE AT ANGLE ANG

```
COMMON/GEOMI/RANGE,ELEV,RADHI,TARHI,ANGLA,THETA,ANGLB,XA,XB
COMMON/SURFU/BETA0,SIGMAH,RADEG,PI,ELEVA
COMMON/STEP/RADSTP,XSTEP,STPFLG
COMMON/MATRX/PD(100,100),ANGLE(3000),SLOPE(3000)
COMMON/XAXES/X1,X2,GROUND
```

```
IF (ANGLE(IANG).GT.ANGLA.OR.ANGLE(IANG).LT.ANGLB) GOTO 1
TEMP1=TAN(ANGLE(IANG))
X1=RADHI/TEMP1
X2=GROUND-X1
TEMP2=TARHI/X2
TEMP3=(X1*X2/(X1+X2))*(TEMP1+TEMP2)
TEMP4=BETA0**2-((TEMP1-TEMP2)**2)/4.0
IF (TEMP4.LE.0.0) GOTO 1
YSIZE=TEMP3*SQRT(TEMP4)
RETURN
YSIZE=0.0
```

```
1
RETURN
END
```

```
SENA(MATRX,0)
  FUNCTION FD2(IANG)
```

```
C   FD2   :   THE ROUGHNESS FACTOR AT ANGLE ANG
C   PS11  :   REFLECTION ANGLE SEEN BY RADAR
C   PS12  :   INCIDENT ANGLE OF RADIATION FROM TARGET
C   PS12  :   SPECULAR REFLECTION COEFFICIENT FOR PS11
C   PS22  :   SPECULAR REFLECTION COEFFICIENT FOR PS12
C   BETA  :   BISTATIC ANGLE
C   SIGMA0 : BISTATIC RADAR SCATTERING COEFFICIENT
```

```
COMMON/GEOMI/RANGE,ELEV,RADHI,TARHI,ANGLA,THETA,ANGLB,XA,XB
COMMON/MATRX/Z(100,100),ANGLE(3000),SLOPE(3000)
COMMON/SURFC/BETA0,SIGNAH,RADEG,PI,ELEVA
COMMON/STEP/RADSTP,XSTEP,STPFLG
COMMON/XAXES/X1,X2,GROUND
```

```
FPSHOL=4.0*PI*SIGNAH/.03
TANBET=TAN(BETA0)
PS11=ANGLE(IANG)
PS12=ATAN(TARHI/X2)
PS12=EXP(-(FPSHOL*SIN(PS11))**2)
IF(PS12.GT.1.0)PS12=1.0
PS22=EXP(-(FPSHOL*SIN(PS12))**2)
IF(PS22.GT.1.0)PS22=1.0
BETA=(PS12-PS11)/2.0
SIGMA0=EXP(-(TAN(BETA)/TANBET)**2)/(TANBET**2)
FD2=SIGMA0*SQRT((1.0-PS12)*(1.0-PS22))
```

```
RETURN
END
```

## BLOCK DATA

COMMON/GEOMI/RANGE, ELEV, RADHI, TARHI, ANGLA, THETA, ANGLB, XA, XB  
COMMON/SURFU/BETA0, SIGMAH, RADEG, PI, ELEVA  
COMMON/STEP/RADSTP, XSTEP, STPFLG  
COMMON/XAXES/X1, X2, GROUND  
COMMON/WAIT/IWAIT  
COMMON/COUNT/ICOUNT  
COMMON/PRINT/IPRAM, ANGMAX, ANGMIN, VARLO, VARUP, XHAX, XMIN

END